

TECHNISCHE UNIVERSITÄT MÜNCHEN

Lehrstuhl für Physikalische Chemie

Surface chemistry of unsaturated hydrocarbons on metal based nanoparticles and size-selected clusters under UHV conditions

Marian David Rötzer

Vollständiger Abdruck der von der Fakultät für Chemie der Technischen Universität München zur Erlangung des akademischen Grades eines

Doktors der Naturwissenschaften

genehmigten Dissertation.

Vorsitzender: Priv.-Doz. Dr. Friedrich Esch

Prüfer der Dissertation: 1. Prof. Dr. Ulrich K. Heiz
2. Hon.-Prof. Dr. Richard W. Fischer
3. Prof. Dr. Günther Rupprechter

Die Dissertation wurde am 11.04.2018 bei der Technischen Universität München eingereicht und durch die Fakultät für Chemie am 09.07.2018 angenommen.

The spectator of research on 'carbon' might well sympathise with Dogberry's belief that *They that touch pitch will be defiled.*

Geoffrey C. Bond
in Metal-Catalysed Reactions of Hydrocarbons

FOREWORD

This thesis contains results, which were obtained in the NanoCat laboratory (Lehrstuhl für Physikalische Chemie, TUM) in the framework of MuniCat - Munich Catalysis Alliance between Clariant and Technical University Munich. In particular, chapters 3, 4, 5 and 6 originate from this collaboration. The project was supervised by Prof. U. Heiz and coordinated by Prof. R. W. Fischer. Experimental studies and evaluation were performed under guidance of M. D. Rötzer in the period from 01/2015 to 03/2018. Theoretical calculations presented in chapter 5 have been performed by Dr. B. Yoon and Prof. U. Landman (Georgia Institute of Technology).

ABSTRACT

The interactions between unsaturated hydrocarbons and late transition metals are of fundamental importance for many catalytic processes. To deepen our understanding of the underlying phenomena, different model systems have been investigated under UHV conditions. The influence of the hydrocarbon structure and its degree of unsaturation on hydrogenation selectivity was tested on metal single crystals, supported nanoparticles, and subnanometer, size-selected clusters.

It is shown that the available (de)-hydrogenation chemistry can be tuned by the precise number of metal atoms. As the performance of supported catalysts is decisively controlled by their charge state, a model based on the local work function of the support is proposed to describe charge-transfer. This model is successfully applied to Pt clusters and Pd nanoparticles. Manipulation of the local work function can be used to influence coke formation, the nature of the dehydrogenated overlayer, and the stability of the latter. These parameters are found to control selectivity for (de)-hydrogenation reactions and the results obtained provide a foundation for future studies on the rational design of selective hydrogenation catalysts.

ZUSAMMENFASSUNG

Die Wechselwirkungen zwischen ungesättigten Kohlenwasserstoffen und späten Übergangsmetallen bilden die Grundlage für viele katalytische Prozesse. Um diese genauer zu verstehen, wurden unterschiedliche Modellsysteme unter UHV Bedingungen untersucht. Hierbei wurde der Einfluss der molekularen Struktur und des Sättigungscharakters des Kohlenwasserstoffs auf die Hydrieraktivität von metallischen Einkristallen, geträgerten Nanopartikeln und Größen-selektierten Clustern getestet.

Hierbei lassen sich die möglichen (De)-Hydrierpfade durch die genaue Anzahl an Metallatomen kontrollieren. Da die Aktivität geträgerter Katalysatoren durch deren Ladungsdichte bestimmt ist, wurde ein Modell entwickelt, welches den Ladungstransfer zwischen Trägermaterial und Aktivkomponente beschreibt. Dieses basiert auf der lokalen Austrittsarbeit des Trägers und wird erfolgreich verwendet, um die Hydrieraktivität von Pt Clustern und Pd Nanopartikeln zu beschreiben. Durch eine Manipulation der lokalen Austrittsarbeit ist es möglich, sowohl ungewünschte Kohlenstoffablagerungen zu unterbinden als auch die Struktur und Stabilität dehydrierter Oberflächenspezies zu beeinflussen, welche ausschlaggebend für die Selektivität der Metallkomponente sind. Die gewonnenen Erkenntnisse bilden die Grundlage für zukünftige Forschung auf dem Gebiet der Selektivhydrierungen.

TABLE OF CONTENTS

	Page
List of Figures	xi
List of Tables	xvi
1 Introduction	1
1.1 The Impact of Catalysis	1
1.2 Hydrogenation Reactions on Late Transition Metals	5
1.2.1 The Nature of the Active Site	8
1.2.2 Coke Sensitivity and the Organometallic Zoo	11
1.2.3 The Selectivity Criterion	16
1.2.4 Concepts of Cluster Catalysis	20
1.2.5 Industrial Challenges During Selective Hydrogenation	25
1.3 Thesis Outline and Roadmap	31
2 Experimental	33
2.1 Ultra High Vacuum Chamber	34
2.1.1 Infrared Reflection Absorption Spectroscopy	35
2.1.2 Electron Emission Spectroscopies	38
2.1.3 Temperature-Programmed Desorption and Reaction	41
2.1.4 Pulsed Molecular Beam Reactive Scattering	43
2.1.5 QMS Calibration	44
2.1.6 Film Synthesis and Characterization	47
2.2 Cluster and Nanoparticle Synthesis	51
2.3 Specific Experimental Procedures	54
2.3.1 Surface Chemistry of Hexynes on Pt(111)	54
2.3.2 3-Hexyne on Size-Selected Pt Clusters	57
2.3.3 Ethylene Hydrogenation on Size-Selected Pt Clusters	58
2.3.4 Ethylene Hydrogenation on Pd Nanoparticles	59
2.3.5 Acetylene Hydrogenation on Pd Nanoparticles	61
3 Surface Chemistry of Hexynes on Pt(111)	67
3.1 Introduction	68

TABLE OF CONTENTS

3.2	Results	71
3.2.1	TPD Studies of 1- and 3-Hexyne	71
3.2.2	MIES/UPS of 1- and 3-Hexyne	74
3.2.3	IRRAS of 1-Hexyne	78
3.3	Discussion	81
3.3.1	Dehydrogenation and Thermal Hydrogen Evolution	81
3.3.2	Desorption of C ₆ Molecules	85
3.4	Conclusions	90
3.5	Additional Insights	92
4	3-Hexyne on Size-Selected Pt Clusters	97
4.1	Introduction	98
4.2	Results	100
4.3	Discussion	103
4.3.1	Dehydrogenation Pathways	104
4.3.2	Hydrogenation Pathways	107
4.4	Conclusions	112
5	Ethylene Hydrogenation on Size-Selected Pt Clusters	115
5.1	Introduction	115
5.2	Results and Discussion	116
5.3	Conclusions	129
6	Ethylene Hydrogenation on Pd Nanoparticles	131
6.1	Introduction	132
6.2	Results and Discussion	134
6.2.1	Hydrogen Chemisorption	136
6.2.2	Ethylene Hydrogenation	138
6.2.3	Active Phase and Deactivation	142
6.2.4	Influence of Metal-Support Interaction on Reaction Rate	147
6.3	Conclusions	150
6.4	Some Additional Remarks	152
7	Acetylene Hydrogenation on Pd Nanoparticles	159
7.1	Introduction	160
7.2	Results	163
7.3	Discussion	166
7.3.1	Metal-Support Interactions on Clean Particles	169
7.3.2	The Role of Dehydrogenated Species During Acetylene Hydrogenation	172
7.4	Conclusions	177
7.5	Additional Insights- Pd Nanoparticles on MgO(100)	181

8 Conclusion and Outlook	191
A Appendix	201
Bibliography	211

LIST OF FIGURES

FIGURE	Page
1.1 Excerpt of the periodic table showing general properties of Pd and Pt.	6
1.2 Simplified hydrogenation reaction scheme of unsaturated hydrocarbons.	7
1.3 Mechanism of C ₂ spectator formation on platinum and palladium for acetylene and ethylene.	14
1.4 The selectivity dependence between different reaction products on relative heights of activation barriers.	18
1.5 The evolution of Pd based selective hydrogenation catalysts.	27
1.6 Industrial configurations of selective acetylene hydrogenation plants.	28
1.7 Thesis road-map.	32
2.1 Schematic of the experimental setup used for this dissertation.	36
2.2 Experimental setup for infrared reflection absorption spectroscopy (IRRAS).	37
2.3 Spectroscopic characterization of a-SiO ₂ supported on Pt(111) and Mo(211).	50
2.4 TPD of probe molecules on a-SiO ₂ supported on Pt(111) and Mo(211).	52
2.5 Mass scan of size-selected Pt _n ⁺ clusters and retarding field analysis for Pt ₁₃ ⁺	55
2.6 Mass scan of Pd nanoparticles during optimization and size distribution of mass-selected particles.	56
2.7 Experimental data acquisition and evaluation for acetylene hydrogenation.	64
3.1 TPD studies of 3- and 1-hexyne on Pt(111) depicting alkyne and alkene desorption.	72
3.2 TPD studies of 3- and 1-hexyne on Pt(111) depicting hydrogen and benzene desorption.	75
3.3 Coverage dependent UP/MIE spectra of 3- and 1-hexyne on Pt(111).	76
3.4 Change of work function and peak positions of 3- and 1-hexyne extracted from the UP/MIE spectra.	79
3.5 IRRA spectrum of multilayer 1-hexyne adsorbed on Pt(111).	80
3.6 Percental product distribution of 3- and 1-hexyne on Pt(111) during TPD.	82
3.7 Proposed reaction mechanism for benzene formation of hexynes and hexenes on Pt(111).	91
3.8 TPD studies of different hexenes on Pt(111).	93
3.9 IRRA spectra of 3-hexenes and 3-hexyne adsorbed on Pt(111) at 100 K.	96

4.1	TPR studies of 3-hexyne and deuterium on size-selected Pt clusters supported on MgO(100) tracing $m/z = 86$ and $m/z = 90$	101
4.2	TPR studies of 3-hexyne and deuterium on size-selected Pt clusters supported on MgO(100) tracing $m/z = 69$ and $m/z = 78$	102
4.3	Product distribution of 3-hexyne and deuterium on size-selected Pt clusters.	103
4.4	TPD of 3-hexyne on single Pt atoms supported on MgO(100).	107
4.5	Comparison between TPR results obtained for 3-hexyne and ethylene hydrogenation.	109
5.1	Experimental and theoretical characterization of the two a-SiO ₂ systems.	120
5.2	The calculated work function of the grown a-SiO ₂ films on Pt(111) and Mo(211).	122
5.3	The charging propensity of a metal cluster adsorbed on the metal-adsorbed a-SiO ₂ film in dependence of the local work function.	126
5.4	Ethane TOF during ethylene hydrogenation of size-selected Pt clusters on different a-SiO ₂ thin films.	128
6.1	Schematic design of the two Pd model systems used for hydrogenation of ethylene and acetylene.	136
6.2	D ₂ -TPD spectra ($m/z = 4$) of Pd nanoparticles supported on (a) a-SiO ₂ /Pt(111) and (b) a-SiO ₂ /Mo(211).	139
6.3	Activity results for ethylene hydrogenation of supported Pd nanoparticles given as ethane TOF per Pd particle in progression of single ethylene pulses at 300 K.	141
6.4	<i>Post-mortem</i> TPR spectra of Pd nanoparticles after ethylene hydrogenation.	146
6.5	CO IRRAS data of Pd nanoparticles supported on a-SiO ₂ before and after ethylene hydrogenation at 300 K.	148
6.6	TPR spectra of D ₂ / ethylene on Pd nanoparticles supported on a-SiO ₂ /Pt(111) (a) and a-SiO ₂ /Mo(211) (b).	158
7.1	Activity results for acetylene hydrogenation catalyzed by clean and poisoned Pd nanoparticles supported on a-SiO ₂ /Pt(111) (a) and a-SiO ₂ /Mo(211) (b).	164
7.2	<i>Post-mortem</i> TPR spectra of Pd nanoparticles supported on a-SiO ₂ /Pt(111) (a) and a-SiO ₂ /Mo(211) (b) after acetylene hydrogenation.	167
7.3	CO IRRAS data after acetylene hydrogenation on Pd nanoparticles supported on a-SiO ₂ /Pt(111) (a) and a-SiO ₂ /Mo(211) (b).	168
7.4	Available C ₂ reaction pathways of acetylene and ethylene on supported Pd nanoparticles.	178
7.5	D ₂ -TPD spectra ($m/z = 4$) of Pd nanoparticles supported on MgO(100): (a) in dependence of coverage and (b) in the presence of CO.	183
7.6	Activity results for ethylene hydrogenation of Pd nanoparticles supported on MgO(100) at 300 K.	184
7.7	Activity results for acetylene hydrogenation catalyzed by clean (a) and poisoned (b) Pd nanoparticles supported on MgO(100).	188

7.8	CO IRRAS data (a) and <i>post-mortem</i> TPR spectra (b) after acetylene hydrogenation on Pd nanoparticles supported on MgO(100).	189
8.1	Schematic of the new experimental setup.	198
A.1	Auger spectra for 3- and 1-hexyne on Pt(111) after TPD to 800 K.	204
A.2	Background correction for the desorption of 3-hexyne during TPD.	207
A.3	Temperature dependent IRRA spectra of 1-hexyne on Pt(111).	208
A.4	Publishing agreement for the Journal of Physical Chemistry C.	209

LIST OF TABLES

TABLE	Page
2.1 Sensitivity factors of C ₆ -molecules determined by QMS calibration.	46
3.1 Vibrational band assignments for a multilayer of 1-hexyne adsorbed on Pt(111) at 100K in comparison to Ru(0001).	81
3.2 Vibrational band assignments for 3-hexenes and 3-hexyne adsorbed on Pt(111) at 100K.	95
A.1 Theoretical photoelectron peak assignment for a gas phase spectrum of 3-hexyne. .	205
A.2 Theoretical photoelectron peak assignment for a gas phase spectrum of 1-hexyne. .	206

INTRODUCTION

1.1 The Impact of Catalysis

Today, the usage of catalysts and the basic underlying principles are widely known and applied on an industrial and laboratory scale. In fact, the fundamental definition itself as described by W. Ostwald in 1901 remains unchanged to this day [1]: "A catalyst is a substance that accelerates a chemical reaction without being observed in the final reaction product."¹ As of 2018, this definition is often expanded emphasizing two important aspects: first, the catalyst itself remains unchanged after completion of the reaction cycle and second, the final position of the thermodynamic equilibrium of the reaction stays the same highlighting the kinetic nature of the phenomenon catalysis.

Nowadays approximately 80-90% of chemical industry products are made by catalytic processes and most of the technical and cultural revolution would not have been possible in the last century without significant improvements of our understanding about catalysis [2–4]. The prime example of the benefits gained by catalysis in the last century is the Haber-Bosch process, enabling the production of ammonia on an industrial scale crucial for the feeding of the ever-growing population of humans on earth. Given this significant importance, it is obligatory at this point to mention two Nobel prizes awarded to W. Ostwald in 1909 and to G. Ertl in 2007 for their contributions in the field of catalysis. In light of the steadily growing demand of mankind on energy and resources, catalysis can be identified to be one of the key technologies to ensure and maintain the standard of living and wealth under sustainable conditions [5].

In 2013, a "Technology Roadmap: Energy and GHG (green house gases) Reductions in the Chemical Industry via Catalytic Processes" was published by a joint collaboration of International Energy Agency (IEA), DECHEMA Gesellschaft für Chemische Technik und Biotechnologie e. V., and the International Council of Chemical Associations (ICCA) [6]. The authors concluded

¹This definition is translated, since the original publication in *Physikalische Zeitschrift* was written in German.

by a combination of scenarios, that in 2050 approximately 13 EJ ($\text{Eta}=10^{18}$) per year could be saved by improvements of catalysts and related processes. Since this energy is hardly imaginable, it is convenient to compare this finding to current state-of-the-art technology. The energy production of a medium-sized nuclear power plant can be assumed to be 11 GkWh ($\text{Giga}=10^9$) per year, which is equivalent to $3.96 \cdot 10^{16}$ J per year. Division of both numbers leads to a total of 328 nuclear power plants, which could be spared by significant upgrades of catalysis related processes. This number is comparable to the total number of plants currently used worldwide. The use of renewable energy resources, e.g. wind, leads to another scenario. The energy production of a wind turbine is approximately 6 GWh per year ($\equiv 2.16 \cdot 10^{13}$ J per year). A total of $\sim 602,000$ wind turbines would be required to ensure this demand. Supposing the average space requirement to be 4000 m^2 for one wind wheel to run effectively, the space needed to build these plants would be $\sim 24074 \text{ km}^2$. That is one third of the size of the Free State of Bavaria ($\sim 70,000 \text{ km}^2$). In light of this huge amount of energy, which could be saved by increased effectiveness of catalytic processes, and the goal being clearly defined, the question arises what circumstances prevent us from implementing these better technologies today?

The answer to this question is, that these technologies are currently under development and don't exist yet [7]. Here, the major problem is grounded in the complexity of the faced challenges and, although the ultimate goal can be clearly assigned, the road can be long and windy, if one doesn't know the exact route. An inter-disciplinary approach is necessary in order to tackle this endeavor as the intricacy of catalytic progress lies within the multi-level dimensionality of the process itself, ranging from reactor design in thousands of m^2 to molecular events on the atomic scale below one nanometer ($1 \text{ nm}=10^{-9} \text{ m}$) [8].

It is this small size regime of matter, which is the major topic of this work. Investigations of interactions on the atomic scale under applied reaction conditions are often hampered by the presence of undesired species, e.g. gases, and physical limitations of spectroscopic methods. One approach to minimize those effects is the use of ultra-high vacuum (UHV, $< 10^{-7}$ mbar), under which the real world catalyst can be mimicked and the pure interactions between reactant and catalysts can be examined. The research performed under these conditions is referred to as model catalysis, as it is the aim to gain insights into catalytic processes under idealized conditions. It was the aim of this work to elucidate the interactions between unsaturated hydrocarbons and late transition metals in general and in particular with regard to hydrogenation reactions, an important reaction class within industry [2]. Before the performed research and the used experimental approach are presented, a brief introduction of the surface chemistry of unsaturated hydrocarbons on late transition metals is given in the next section.

1.2 Hydrogenation Reactions on Late Transition Metals

Late transition metals were recognized to be efficient hydrogenation catalysts already in the early stages of heterogeneous catalysis at the start of the 20th century. Consequently, it is not too surprising that a vast amount of literature exists covering all aspects of these systems.

These aspects span from macroscopic reactor design and microscopic transport phenomena to nanoscopic molecular investigations. It seems impossible to give an entire overview over the existing literature without neglecting certain point of views worth being mentioned. Rather than trying this unfeasible endeavor, the literature overview in this work puts emphasis on selected topics about the molecular surface chemistry of unsaturated hydrocarbons on late transition metals, in particular Pd and Pt. It is the aim to demonstrate trends of general validity, but also the difficulties encountered when investigating these systems. Detailed discussions about specific literature can be found along with the results presented in each chapter.

58.93 760.4 1.91 27 Co Cobalt [Ar]3d ⁷ 4s ²	58.69 737.1 1.88 28 Ni Nickel [Ar]3d ⁸ 4s ²	63.55 745.5 1.90 29 Cu Copper [Ar]3d ¹⁰ 4s ¹
102.91 719.7 2.28 45 Rh Rhodium [Kr]4d ⁸ 5s ¹	106.42 804.4 2.20 46 Pd Palladium [Kr]4d ¹⁰	107.87 731.0 1.93 47 Ag Silver [Kr]4d ¹⁰ 5s ¹
192.22 880.0 2.20 77 Ir Iridium [Xe]4f ¹⁴ 5d ⁷ 6s ²	195.08 870.0 2.28 78 Pt Platinum [Xe]4f ¹⁴ 5d ⁹ 6s ¹	196.97 890.1 2.54 79 Au Gold [Xe]4f ¹⁴ 5d ¹⁰ 6s ¹

Atomic mass	195.08	78	Atomic number
1 st Ionization energy	870.0	2.28	Electronegativity
Chemical symbol	Pt		
Name	Platinum		
Electron configuration	[Xe]4f ¹⁴ 5d ⁹ 6s ¹		

Figure 1.1: Excerpt of the periodic table showing general properties of palladium and platinum: Both belong to the group 10 metals (along with nickel) of the periodic table, also referred to as nickel group.

An excerpt of the periodic table showing the metals of interest (Pd and Pt) in this work is presented in figure 1.1. Although nickel (Ni) is also known for hydrogenation reactions (notably as Raney nickel), its surface chemistry is omitted here and the reader is referred to the literature [9–12]. To explain the high activity of Pd and Pt for hydrogenation reactions of unsaturated hydrocarbons, it is necessary to understand the reaction mechanisms on a molecular level. The most basic reaction scheme for hydrogenations of double and triple CC bonds is given in figure 1.2. Here, an alkyne is adsorbed on the metal surface. Half-hydrogenation of the alkyne *via* atomic hydrogen leads to a vinyl-intermediate, which can be further hydrogenated to an alkene. The alkene in turn can either desorb or be further stepwise hydrogenated to the according alkane [13]. This stepwise addition of hydrogen to the hydrocarbon, which is commonly assumed during mechanistic discussions, is referred to as Horiuti-Polanyi mechanism [14]. It should be noted, that for both metals, Pd and Pt, normal Eley–Rideal mechanisms based on addition of molecular hydrogen (gas) to the olefin or addition from the olefin (gas) to atomic hydrogen (reversed) have been discussed [15–19]. All of these studies concluded, that Eley-Rideal mechanisms only play a negligible role under most reaction conditions and therefore these are neglected in the ongoing section.

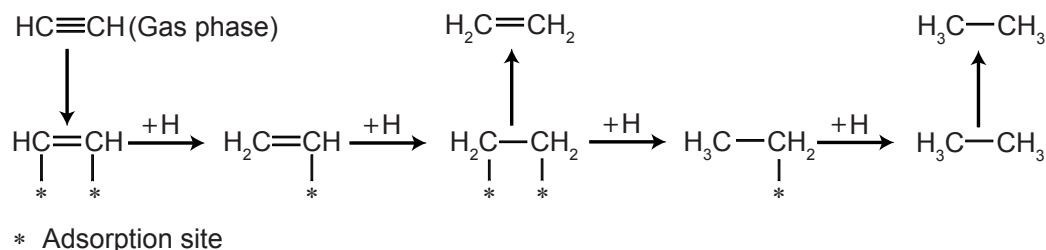


Figure 1.2: Simplified hydrogenation reaction scheme of unsaturated hydrocarbons: Adsorbed alkynes and alkenes are hydrogenated by stepwise addition of atomic hydrogen. Additional reaction channels like dehydrogenation are omitted.

From the basic description of hydrogenation in figure 1.2 already two important aspects can be derived: the catalyst needs to dissociatively adsorb hydrogen and activate the according unsaturated hydrocarbon. Here, the formed hydrogen atoms on the metal surface have a hydride character [4]. The special case of subsurface hydride species on Pd based systems is dealt with in chapter 6 and disregarded for the moment. The interaction and activation of the hydrocarbon can be described by the Dewar-Chatt-Duncanson model and combination of molecular orbitals with the according states of the metal in analogy to organometallic chemistry [12, 20–22]. In short, the hydrocarbon donates electron density from its highest occupied orbital to the metal, which in return increases itself the electron density at the lowest unoccupied orbital of the hydrocarbon by back-donation. Obviously, the extent of donation/back-donation not only depends on the molecular orbitals of the hydrocarbon, but also on the density of states of the metal with respect to the Fermi energy (E_F) and the position of the latter in reference to the vacuum level. One example of these interactions can be given for ethylene adsorbed on platinum, where significant rehybridization from sp_2 to $sp_{(2.5-3)}$ is observed upon adsorption for ethylene, experimentally and theoretically [23, 24]. This rehybridization results in an activated, elongated CC bond and movement of the hydrogen atoms out of the molecular plane. The same effect is observed for the well-known Zeise’s salt $\text{K}[\text{PtCl}_3(\text{C}_2\text{H}_4)] \cdot \text{H}_2\text{O}$ in organometallic chemistry [25].

1.2.1 The Nature of the Active Site

Having established the basic requirements of a late transition metal based hydrogenation catalyst for unsaturated hydrocarbons, the question arises, what does the adsorption site given in figure 1.2 look like. Indeed, the description and identification of the nature of the active site, which can be regarded as being equivalent to the adsorption site for the present, remains one of the holy grails in catalysis research since the basic concept was introduced by Taylor in 1925 [26] and is still debated today [27, 28]. For metal-catalyzed transformations of hydrocarbons, the definition of singular active centers becomes increasingly complex and it is the opinion of the author that our current understanding can be considered incomplete.

To illustrate the aforementioned difficulty, we shall first consider the adsorption of alkynes

and alkenes on clean transition metals under UHV conditions, as it is a necessity for activation. Most of the times, the adsorption results in chemisorbed species, which are coordinated to a different amount of metal surface atoms. In the case of alkynes, the species observed are denoted as di- σ /di- π or di- σ/π , in which the alkyne interacts either with three or four surface atoms. As stated by G. Bond, there is little evident chemical logic, which surfaces show which structure [29]. For alkenes, mainly two modes of interactions are identified being a strongly-bound di- σ and a weakly bound π species. In summary, even the adsorption site and mode of one particular hydrocarbon needs to be evaluated carefully.

To make matters worse, it was shown by the pioneering work of Cremer and Somorjai, that the hydrogenation of ethylene can proceed *via* both adsorption modes on Pt(111) [30, 31]. However, the di- σ mode can also lead to the formation of ethynidyne, which effectively blocks the surface and prevents further di- σ adsorption. Consequently, this adsorption mode is only of minor importance during hydrogenation, as it also leads to dehydrogenation, which is discussed in more detail in the next subsection. The different reactivities of these two adsorption modes are by no means unique to ethylene hydrogenation on Pt(111), but have also been discussed for alkynes on Pt and Pd [32, 33]. It seems like the first hydrogenation step for alkynes and alkenes in figure 1.2 is facilitated by weak π adsorption modes, whereas strong chemisorption results either in dehydrogenation or blockade of the metal surface.

Having gained a basic understanding of the bonding behaviour of unsaturated hydrocarbons on transition metals, the next step is to define the active site required for hydrogenation. Let us suppose that such sites are the minimum ensemble of metal atoms capable of hydrogenation, how many atoms are actually needed for this definition? In our recent work, we have shown that the hydrogenation of ethylene catalyzed by size-selected Pt_n clusters supported on MgO is structure-sensitive [34]. More interestingly in this context, density functional theory (DFT) calculations revealed that the local electron density on single Pt atoms within the cluster determine the activity towards hydrogenation. Here, the local electron density is not only influenced by direct undercoordinated neighbouring atoms, but also by atoms located several Ångströms away. For instance, the tenth atom in a Pt₁₀ cluster can be regarded as an ad-atom of Pt₉ and electron sink, leading to higher hydrogenation activity of the residual atoms within the cluster. This atom is not directly involved in bond making or breaking during ethylene hydrogenation, yet it has a major impact on other, classically defined "active sites" and needs to be accounted for understanding the results obtained. This definition problem is not only observed for clusters in the sub-nm size regime, but also for other systems, e.g. the surface chemistry of unsaturated hydrocarbons on Pt(111) in comparison to Pt₃Sn and Pt₂Sn alloys [35–37]. Although small ensembles of Pt still exist on the surface of these alloys, the chemistry available on these surfaces is significantly altered in the presence of Sn, which is believed to be caused by an electronic effect. Again, no bond is formed between the hydrocarbons and Sn atoms, yet the latter decisively control the Pt atoms. These two examples amplify the problem of defining one catalytic active site for hydrogenation reactions.

1.2.2 Coke Sensitivity and the Organometallic Zoo

The definition of an active site for hydrogenation reactions is not only hampered by the influence of catalyst atoms not directly involved in bond making or breaking, but also by the surface chemistry of unsaturated hydrocarbons themselves, especially under UHV conditions. Already the first works on hydrocarbons on metal single crystals (see for instance references [38–41]) demonstrated, that the thermal chemistry of these molecules on initially clean metals leads to dehydrogenation rather than hydrogenation. Here, the formation of ethylidyne on Pt(111) from ethylene at room temperature represents the most investigated system [42]. The identification and characterization of this species by the most respected researchers in the field took several years and a historical overview of this exciting discussion can be found within the work of my great predecessor Crampton [43]².

The theoretical, basic mechanism of dehydrogenation is schematically shown in figure 1.3 for acetylene and ethylene on Pt(111) and Pd(111) at room temperature. Three different reactions have to be taken into account in general for transformation of adsorbed, unsaturated hydrocarbons: dehydrogenation under removal of hydrogen, hydrogenation under addition of an external hydrogen atom, and intramolecular hydrogen shifts. The calculated main reaction pathway of ethylene to ethylidyne on these metal surfaces is currently believed to follow a three step mechanism, where adsorbed ethylene first dehydrogenates to a vinyl species, which is subsequently hydrogenated to ethylidene. In the last step, ethylidene is dehydrogenated to ethylidyne [44]. However, conversion of vinyl to ethylidyne might also proceed *via* vinylidene as proposed by the same authors later on [45]. Our own calculations on supported, size-selected Pt_n clusters started with a half-hydrogenated ethyl species, which dehydrogenates to ethylidyne *via* ethylidene [34, 46]. The derived activation barriers were in reasonable agreement with temperature-induced activity changes and red-shifts in CO IRRA spectra observed experimentally. Acetylene is believed to be first hydrogenated to vinyl, which follows then the pathways proposed for ethylene. The formation of an ethynyl species on platinum is unfavorable due to a high energy barrier [47]. Besides hydrocarbon coverage dependent effects, the favored reaction pathway can obviously also be steered by the effective hydrogen coverage as can be seen in figure 1.3. This is also the first time, that an analogy between acetylene and ethylene is observed in their surface chemistry on late transition metals.

Although ethylidyne is the most prominent example for a dehydrogenated species at room temperature, it is not at all unmeted as it belongs to the group of alkylidynes, which are observed for almost all unsaturated hydrocarbons on metal surfaces. They include propylidyne, butylidyne up to hexylidyne [48–50]. As a rule of thumb, dehydrogenated species including alkylidynes prefer adsorption sites, where the missing valencies of carbon atoms are replaced by single σ bonds between carbon and metal atoms. Dehydrogenated species formed between 200 and 400 K have one common fate, as all of them are further dehydrogenated to amorphous or graphitic carbon at higher temperatures.

²The choice of words here was inspired by Garry Kasparov's *My great predecessors*.

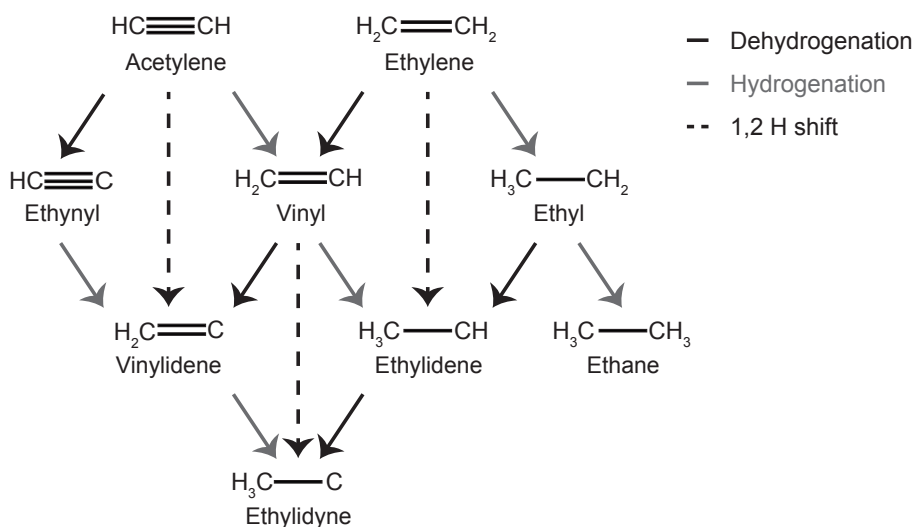


Figure 1.3: Mechanism of spectator formation on platinum and palladium. The ethylene path follows the three step model proposed by Rösch [45], whereas the acetylene path has been added according to Lu *et al.* [47]. Black arrows to the left are dehydrogenation steps, whereas grey arrows to the right are hydrogenation reactions. 1,2 Hydrogen shifts are presented by vertical, dotted lines. Missing valencies of carbon atoms are used for carbon metal bonds, which are omitted for the sake of simplicity.

Now, as we know that a carbonaceous overlayer is formed on the metals of interest, we shall ask, what is the role of this adlayer during catalysis? As a matter of fact, this is one of the key questions unanswered even for the best investigated olefin hydrogenations [51]. The common belief is that the by far most important role of dehydrogenated species is to block the active metal surface. They are often considered to be spectator species, as they are not directly involved in the hydrogenation mechanism, e.g. the rate of ethylidyne hydrogenation on Pt(111) is significantly lower than the ones of general olefin hydrogenation, prohibiting direct participation in the reaction [52]. However, they might be responsible for the creation of small, uncovered metal islands, where the actual reaction takes place. This idea was enforced for acetylene hydrogenation on Pd based catalysts by Borodziński and Bond [33, 53]. The size of the small metal islands leads to different active sites for acetylene and ethylene on Pd, which has also been observed in one of the first systematic semi-hydrogenation studies [54]. The influence of dehydrogenated species on the creation of small metal sites is another example of the difficult definition of active sites.

In addition, the role of the dehydrogenated species might exhibit more hidden subtleties and only the most important concepts are introduced here. One idea is, that these species prevent intimate contact between the unsaturated olefin and the metal leading to di- σ adsorption and favor weak π adsorption, which was shown to be beneficial for hydrogenation activity [31, 52]. The dehydrogenated overlayer may also act as a hydrogen reservoir/source. Due to the experimental challenge, the scientific approval of this hypothesis has yet to be performed and is

currently under debate [51].

It can be concluded, that the dehydrogenated overlayer has a major impact on catalytic performance of hydrogenation catalysts. In light of the outlined surface chemistry, it borders to irony that hydrogenation reactions should be considered as coke-insensitive according to Menon [55]³. Similar to Boudart's classification of structure-insensitive/ facile and structure-sensitive/ demanding reactions [56], the author proposed that catalytic reactions can be classified into coke-insensitive and sensitive reactions. "Coke-insensitive reactions are met, when there is hydrogen under pressure or a strong hydrogenation catalyst in the system, because the carbonaceous species can then be considered to be intermediates, whereas coke-sensitive are encountered in the absence of these two parameters, since the formed coke then remains on the active component" [55]. It should be noted, that the classification of coke-insensitivity makes no statement about the influence of the coke on catalytic activity. As stated by the author for coke-insensitive reactions, "it (coke, author's note) can also be termed 'beneficial' when it enhances selectivity or serves as a reactive carbonaceous overlayer on the catalyst surface, or may be the actual catalytic site itself on the surface" [55]. Most surface scientists working on unsaturated hydrocarbons would agree with this statement.

1.2.3 The Selectivity Criterion

One of the most important aspects in hydrogenation catalysis is the control over selectivity, which describes the yields of different reaction products. A model developed by the group of Zaera is useful to understand the underlying physical properties, which determine overall selectivity [51, 52, 57]. Despite its simplicity and limitations, this model nicely describes key aspects of selectivity.

The model, which is given in figure 1.4, describes the parallel reaction pathways of a reactant molecule on a one-dimensional potential energy surface, which can either react to product 1 or 2. The event of the reactant forming product 1 or 2 can be considered to follow Arrhenius behavior, where the pre-exponential factor is the same for both pathways. The two reaction channels only differ by their activation barriers ΔG_1^\ddagger and ΔG_2^\ddagger . The reaction rate is now determined by the absolute height of the according barriers, whereas the selectivity between product 1 and 2 is determined by the difference of both barriers, $\Delta G_1^\ddagger - \Delta G_2^\ddagger$. We can define the selectivity S_1 of product 1 as $S_1 = S_1/(S_{Total}) = S_1/(S_1 + S_2)$ and assume $\Delta G_2^\ddagger = 0.8$ eV at 300 K (typical value for the hydrogenation of acetylene [33]). Variation of $\Delta G_1^\ddagger - \Delta G_2^\ddagger$ and its influence on the selectivity S_1 is given in figure 1.4. Uniform activation barriers ($\Delta G_1^\ddagger - \Delta G_2^\ddagger = 0$) obviously lead to a equal product distribution. A decrease of 0.05 eV in ΔG_1^\ddagger leads to a selectivity increase in S_1 of $\sim 90\%$ and an increase of 0.05 eV to $\sim 10\%$. In other words, a change in activation barrier of 0.1 eV enables a selectivity switch from ~ 90 to $\sim 10\%$.

The benefit of this simple model is that it allows us to estimate the necessary changes in relative barrier heights in order to steer chemical selectivity. Furthermore it can be successfully

³The author would like to clarify, that it's not his intention to criticize the idea, but rather the diction.

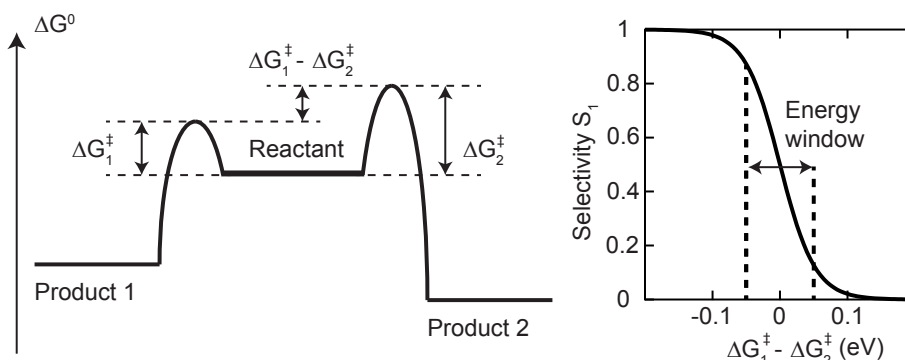


Figure 1.4: The dependence of selectivity between different reaction products on relative heights of activation barriers is given for a one-dimensional potential energy surface: The reactant can either react to product 1 or 2 depending on the relative barrier heights of ΔG_1^\ddagger and ΔG_2^\ddagger , respectively (left). Keeping ΔG_2^\ddagger constant, variation of barrier height ΔG_1^\ddagger determines the overall selectivity S_1 for product 1 (right). The calculation was performed for 300 K and $\Delta G_2^\ddagger = 0.8$ eV.

expanded to consecutive reactions by replacing one product to the gas phase value. The absolute reaction activation barrier height is then given by the desorption energy. As the energy of a product in the gas phase is fixed, two ways emerge in order to steer selectivity of consecutive reactions: either the desorption energy is manipulated by the reactant or the reaction barrier of the alternative pathway is altered. One example, where this model can be applied, is the high selectivity of small Au nanoparticles for triple over double bond hydrogenation [58–61]. In contrast to alkynes, the heat of adsorption of olefins is believed to be very small, which results in low desorption activation energies (assuming that the according adsorption activation energy is negligible). The alkenes formed by hydrogenation of alkynes simply desorb before overhydrogenation to the alkane can occur resulting in remarkable high selectivities.

Also the hydrogenation process itself can be thought of as a consecutive reaction *via* a half-hydrogenated species as shown in figure 1.2. Identification of the rate-determining step (RDS) for alkyne or alkene hydrogenation has attracted much attention, but the results vary depending on metal and reaction conditions (e.g. UHV *vs* applied). In general, both hydrogenation steps exhibit similar activation barriers, which makes an absolute answer unfeasible. Changes as small as 0.1 eV of one barrier might change the RDS as predicted by the selectivity model, although both steps contribute to the reaction rate. In this case, it is better to use more sophisticated methods like the degree of rate control proposed by Campbell in order to evaluate the contribution of single steps to the total reaction rate [62–64].

1.2.4 Concepts of Cluster Catalysis

As atoms are put together to form metallic embryos, nuclei, and crystallites, how does the catalytic activity of the particles vary with their size?

This question was written by M. Boudart in 1966 [65]. Although using different terminology, he formulated a question leading to a new research area, which still occupies researchers all over the world today: the cluster size regime. Here, a cluster of atoms is classically defined as being comprised of two to approximately one hundred atoms and therefore this small size regime of matter is settled between single atoms and nanoparticles; the latter consisting of literally thousands of atoms. In this transition regime, physical and chemical properties can no longer be extrapolated from the bulk material nor from the single atom. Even the addition or removal of single atoms from one cluster can dramatically change its properties leading to a third dimension of the periodic table, where each atom counts [66].

When the nature of small clusters is governed by the exact number of atoms, it requires ultimate control over size in order to reveal any effects truly caused by atomicity. Indeed, early catalytic studies on small clusters under UHV conditions were hampered by a lack of control over size, since evaporated metal atoms were intentionally sintered at high temperatures and the resulting average size was only determined afterwards [67]. This led some catalysis researchers to believe, that it is virtually impossible to prepare a collection of metallic particles that is truly monodisperse [68]. However, experimental physicists, who were originally interested in the material transition between atoms and bulk matter, succored the catalysis community with significant experimental improvements enabling the production of monodisperse, size-selected metal clusters. An excellent review of the experimental possibilities and the gained knowledge about metal clusters at that time was given by de Herr in 1993 [69].

The implementation of experimental novelties, e.g. sputter and laser ablation sources, allowed the investigation of monodisperse cluster materials for catalytic applications under UHV conditions for the first time [70, 71]. The produced clusters were conventionally soft-landed⁴ onto the support material of interest and tested for their catalytic properties by means of temperature-programmed desorption and reaction. Since these early studies, an emerging field of research has developed around the catalysis of size-selected metal clusters. Although recent work on size-selected clusters was also performed under ambient conditions in order to overcome the limitations of the pressure gap, the following passages focus on results and concepts gained under UHV conditions. The reader interested in ambient results is referred to the literature for photocatalysis [72, 73], electrochemistry [74, 75], and thermal catalysis [76].

The standard model system used nowadays under UHV conditions consists of a metal-oxide support material, on which the size-selected metal clusters are deposited. In most of the cases, this support material is grown on metal single crystals. Overall, three key parameters can be identified experimentally for the results of a given reaction: the underlying single crystal, the support material, and the size-selected clusters themselves. All of these parameters are inter-correlated and have to be taken into account when interpreting results.

The influence of the underlying metal single crystal, which might not be too obvious for somebody outside the thin film subject area, is in most cases of electronic nature. The crystal serves as a template for the growth of thin metal-oxide films, the actual support

⁴The definition of soft-landing is given in the experimental section.

material. Therefore, the underlying metals are not in direct contact with the catalytically active component. However, due to the finite size of the thin films, the underlying metal perturbs the electronic structure of the support material. For thick support materials (above 10 monolayers), the influence of the crystal can be neglected, whereas for thinner films (below 3 monolayers), this perturbation can have significant implications on the cluster material. The CO oxidation catalyzed by supported Au₂₀ depends remarkably on the thickness of the MgO(100) film [77]. Here, charge-transfer from the molybdenum to the gold cluster can be achieved by thin MgO films, which leads to wetting of the gold clusters. On thick films, where this charge-transfer is suppressed by the film thickness, the Au₂₀ prefer 3-D structures, which leads to marked differences in catalytic activity for the same cluster size. The transition between 2-D and 3-D morphologies of gold particles in dependence on the film thickness and general charge transfer have also been predicted and observed by other researchers [78, 79]. A more thorough analysis of finite films is given in chapter 5.

The effect of the support material on size-selected metal clusters can be understood in analogy to applied catalysis manifold. It provides the footprint for any adsorbed metal particle, and as such decisively controls the physical state of the latter. This statement is especially true for clusters in the sub-nm size regime, where basically all cluster atoms are in intimate contact to the support. If the support exhibits unique defect sites, clusters can be anchored and activated by charge transfer [80]. For instance, the frequency of CO adsorbed on Pd atoms shifts in dependence of the defect sites on MgO(100) [81]. Not only the defect sites are responsible for charge transfer, but also the support stoichiometry. In particular, we have shown in our previous work, that the stoichiometry of amorphous SiO₂ can be used to (de)-charge Pt₁₃ clusters. In fact, the decharging depends linearly on the number of Pt-O and Pt-Si bonds [82], which in turn can be used to enforce hydrogenation activity. However, simple charging arguments based on general acidity and basicity of support materials fail to predict catalytic activity of clusters, where each cluster size has to be considered separately [83]. At the moment, there is no physical quantity available to describe charge-transfer between support and active component *a priori*, an issue, which will be addressed in chapter 5. Furthermore, the support might not only provide unique adsorption sites, but also be directly involved during catalysis by the creation of a capture zone as evidenced by CO oxidation of Pd_n clusters supported on MgO(100) [84].

The last missing piece is the size-selected cluster itself. It was already mentioned, that the exact number of atoms within the cluster determines its physical and chemical properties. At the moment, two major concepts are used to describe the catalytic activity of metal clusters besides charging: fluxionality and local electron density. The term fluxionality (which is also referred to as flexibility) is used to describe several phenomena [85–87]. On the one hand, one cluster size possesses several isomers having low energy structures [88]. Not only one isomer is thermally accessible at a given temperature, but several, which all contribute to the catalytic activity [89]. This puts severe challenges to the computational description of such systems, as the time needed for calculations scales at least linearly with the amount of isomers. On the other hand, dynamic fluxionality is also used to describe the response of one cluster to

the presence of adsorbates and its behavior during reaction [90]. The concept of local electron density is used to describe the fundamental interactions between an adsorbate and the metal atoms of the clusters [34, 46]. It was recognized that the environment within the cluster can lead to charge-redistributions, which lead to accumulation or deficiency of electron density on single atoms. This charging within the cluster can be used to steer the reaction pathways of interest at single active sites on the cluster.

1.2.5 Industrial Challenges During Selective Hydrogenation

Having established a rudimentary understanding of hydrogenation reactions from a surface chemistry point of view, it is finally time to introduce a reaction of great industrial importance: the selective hydrogenation of acetylene, which is dealt with in chapter 7 in combination with chapter 6 of this thesis.

Ethylene as one of the most important, organic base chemicals, is produced by steam cracking of hydrocarbons. However, the common way of production also leads to hydrocarbons with higher molecular mass and multiple unsaturated molecules such as acetylene, which acts as a poison in the downstream processes. Consequently, the alkyne has to be removed from the feedstock for further processing. As the acetylene market is rather small compared to the one of ethylene, separation based on physical properties is in most cases too expensive and uneconomic. For this reason, acetylene is chemically removed by partial hydrogenation to ethylene thereby increasing the value of the ethylene feedstock. Here, the main aim is to achieve high selectivity towards ethylene and simultaneously keeping overhydrogenation of either acetylene or ethylene, which is present in large excess, as small as possible.

The two basic industrial configurations are shown in figure 1.6 for a) front-end and b) tail-end named after their position relative to the cold box, where hydrogen and partially methane are removed [91]. As can be seen in this figure, the two layouts not only differ by their position within the process layout, but also on the feedstocks they have to process. In the front-end design, excess hydrogen is present, which makes high selectivities harder to achieve for obvious reasons. In addition, varying concentrations of CO, which acts as a beneficial modifier of the catalyst, lead to challenging reactor handling. In contrast to the front-end design, the feedstock of the tail-end layout contains only C_{2+x} hydrocarbons with varying degree of unsaturation. Molecular hydrogen and CO can be added intentionally making handling of the reactor easier. Both setups have in common, that Pd is in most instances the metal of choice for selective hydrogenation and therefore a short overview over the history of the applied systems is beneficial to understand current scientific discussions.

A historical overview of Pd based selective hydrogenation catalysts is shown in figure 1.5. In 1952, Lindlar described a class of catalysts, which are now named after him [92]. He used Pd nanoparticles supported on $CaCO_3$ for the selective hydrogenation of triple bonds during the synthesis of vitamin A. The catalyst was additionally poisoned by lead and quinoline, which is believed to suppress oligomerization [93]. In the seventies, the first generation of industrially

relevant catalysts consisted of Pd supported on a suitable carrier. The next generation in the 90's introduced Ag as a promoter. The new catalysts are therefore alloys, which fascinated scientists ever since their discovery. These alloys were further stabilized in the third generation.

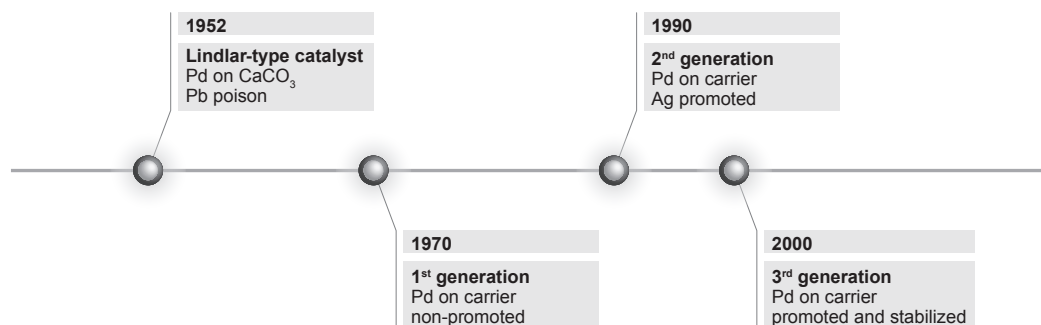


Figure 1.5: The historical evolution of Pd based selective hydrogenation catalysts is shown since 1952 until the 3rd generation.

Given the long history of selective hydrogenation catalysts on Pd basis, it is not too surprising that a vast literature exists, dealing with all aspects of these catalysts. As the chemistry of pure Pd is subject of chapter 6 and 7, it is convenient to mention an alternative academic approach to achieve higher selectivities at this point. The (sub)-surface chemistry of unsaturated hydrocarbons on Pd is characterized by dehydrogenation. Since the formed dehydrogenated species are believed to be located at small ensembles of Pd atoms, an idea is to minimize the latter to one single atom in order to avoid undesired coke deposition and disentangle the subsurface chemistry [94]. A class of materials, which satisfy the single surface atom criterion, are intermetallic compounds of Ga and Pd. Indeed, Pd₂Ga and Pd₅Ga₂ have been experimentally and theoretically proven to be efficient semi-hydrogenation catalysts [95–99]. Whether these catalysts can replace the current ones used in industry has to be awaited.

Considering the advanced understanding, synthesis, and characterization of novel catalytic systems, one might expect, that the chemistry of the Pd metal itself is settled. A short, scientific anecdote is helpful to illustrate the difficulties encountered even when investigating these rather 'simple' systems. In 2013, a theoretical work of Yang *et al.* compared the Pd(111) and Pd(100) surface for the hydrogenation of acetylene. The authors concluded, that the Pd(111) surface should exhibit higher activity and selectivity than the Pd(100) surface [100]. Shortly after, an experimental work was published in the same journal about shape controlled Pd nanoparticles [101]. Here, the Pd(100) surface showed higher activity and selectivity than the Pd(111) surface, in contrast to the previous theoretical study. This discrepancy between the two studies was finally resolved in 2016, when theoretical calculations of the same authors confirmed the higher activity/selectivity of Pd(100) in comparison to Pd(111) under the assumption of a carbide phase [102]. Without judgment of either work, this story nicely illustrates a key point made by Geoffrey Bond about the selective hydrogenation of acetylene on Pd, which is simultaneously a worthy end of this introduction about hydrogenations on late transition

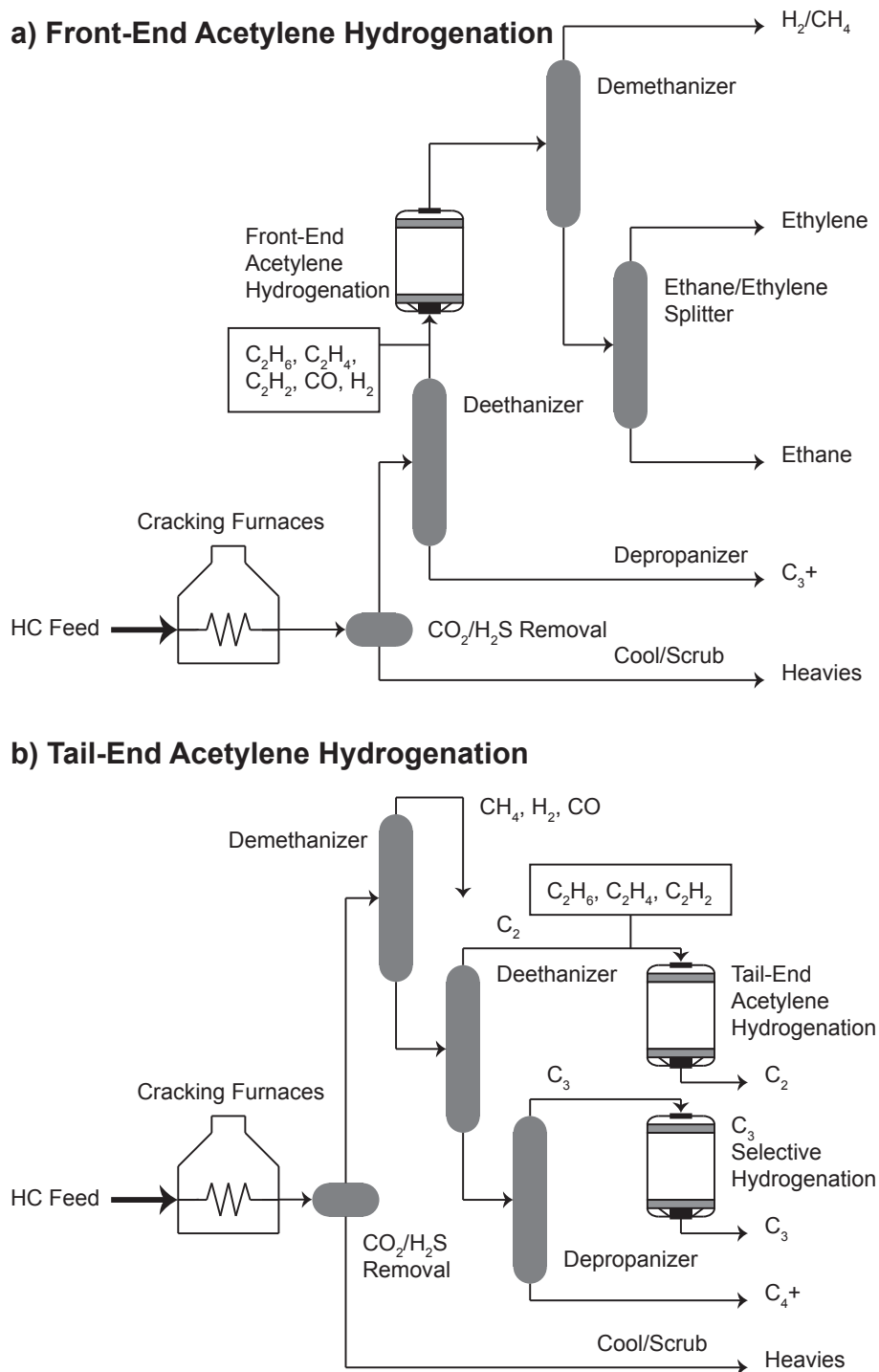


Figure 1.6: The two basic setups of selective acetylene hydrogenation plants are given: a) Front-end and b) tail-end. The configurations are primarily differentiated by the position relative to the cold box [91].

metals:

It is simplistic to try to assign a particular observation to a single cause, as it is more probable that a number of factors are simultaneously at work. ...

Interpretation of results is therefore a minefield through which we must walk delicately,

Geoffrey C. Bond
in Metal-Catalysed Reactions of Hydrocarbons

1.3 Thesis Outline and Roadmap

A graphical overview of the chapters in this thesis is given in figure 1.7. Plotting a physical or chemical quantity of a metal-based material in dependence of the number of involved atoms leads typically to the occurrence of three distinct size regimes. The first one, having an approximately infinite amount of atoms, is called bulk material having known macroscopic properties. Decreasing number of atoms leads to the intermediate size regime nanoparticles, where properties start to deviate from bulk materials. This non-scalable regime differs from the scalable size regime defining cluster-based materials by turning band structures into rather molecular orbitals being influenced by quantum size effects. This fluent transition between nanoparticles and clusters occurs between 100 and 20 atoms.

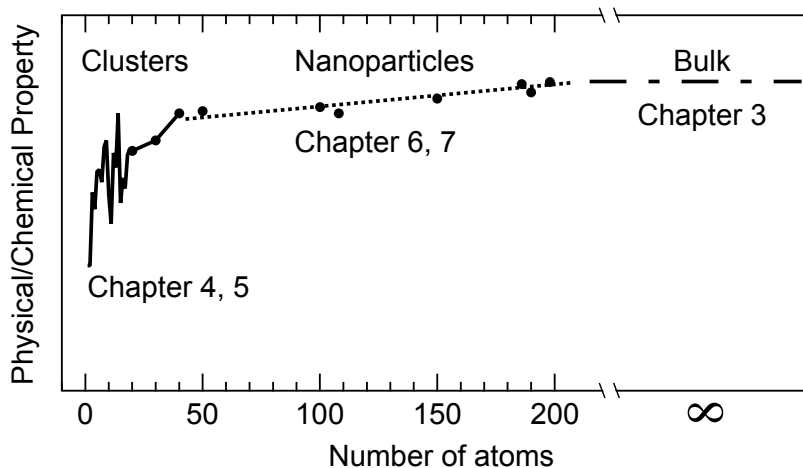


Figure 1.7: Thesis road-map: An arbitrary physical/ chemical property (e.g. electron affinity) is shown as a function of metal atoms. For each regime (clusters, nanoparticles and bulk metal) the chapters dealing with each topic are given.

Each topic shown in figure 1.7 is covered by separate chapters in this thesis. The first scientific chapter 3 deals with the pure surface chemistry of 3- and 1-hexyne on Pt(111) as a bulk material. This chapter provides fundamental understanding of 3-hexyne chemistry on size-selected Pt clusters given in chapter 4. Chapter 5 concerns metal-support interactions between Pt clusters and thin silica films on both, experimental and theoretical basis, and how they can be used to steer catalytic activity for ethylene hydrogenation. These insights into metal-support interactions are expanded to small palladium nanoparticles in chapter 6 and 7. The main focus of chapter 6 is placed on support-dictated hydrogen adsorption and ethylene hydrogenation, whereas chapter 7 is dedicated to acetylene hydrogenation. Here, not only the influence of support is probed, but also the intentional creation of poisoned particles and their impact on adsorption sites of acetylene.

Based on these results a short summary and conclusion is presented in the last chapter of this work being completed by an outlook with respect to future research and challenges.

EXPERIMENTAL

This chapter is dedicated to the ultra-high vacuum (UHV) setup and the experimental procedures used in this work. In the first section, the general setup is described along with a short introduction to each applied method. Special focus is put onto film synthesis and characterization, since metal-support interactions represent a major topic of this dissertation. In the second section, the cluster source used to produce size-selected metal clusters and nanoparticles with a narrow size distribution is presented. Specific experimental details for each chapter are presented in the third section.

2.1 Ultra High Vacuum Chamber

All experiments have been performed in a bakeable, stainless steel UHV chamber having a base pressure of $< 2 \cdot 10^{-10}$ mbar [71]. The setup, which is schematically shown in figure 2.1, is referred to as 'old nanocat' lab, since the new rebuilt one in the Catalysis Research Center (CRC) was accompanied by significant experimental modifications. As can be seen in figure 2.1, the apparatus can be divided into two major parts: the analysis chamber used for experiments under UHV conditions and the cluster source, which is described in more detail in section 2.2. The additional transfer chamber attached to the cluster source is omitted for the sake of simplicity as no ambient cluster results are discussed in this thesis. The analysis chamber includes several spectroscopic techniques and capabilities to synthesize different support materials, which are briefly introduced in the following.

The performed experiments were conducted using single crystals, either as object of investigation themselves (e.g. Pt(111) as in chapter 3) or as starting material for synthesis of thin metal-oxide films. The latter represent support materials for metal particles. These single crystals were attached by tungsten wires to a threefold sample holder mounted to a *xyz*-manipulator capable of rotation by 360° . The samples could be cooled by liquid nitrogen (LN_2) to 100 K

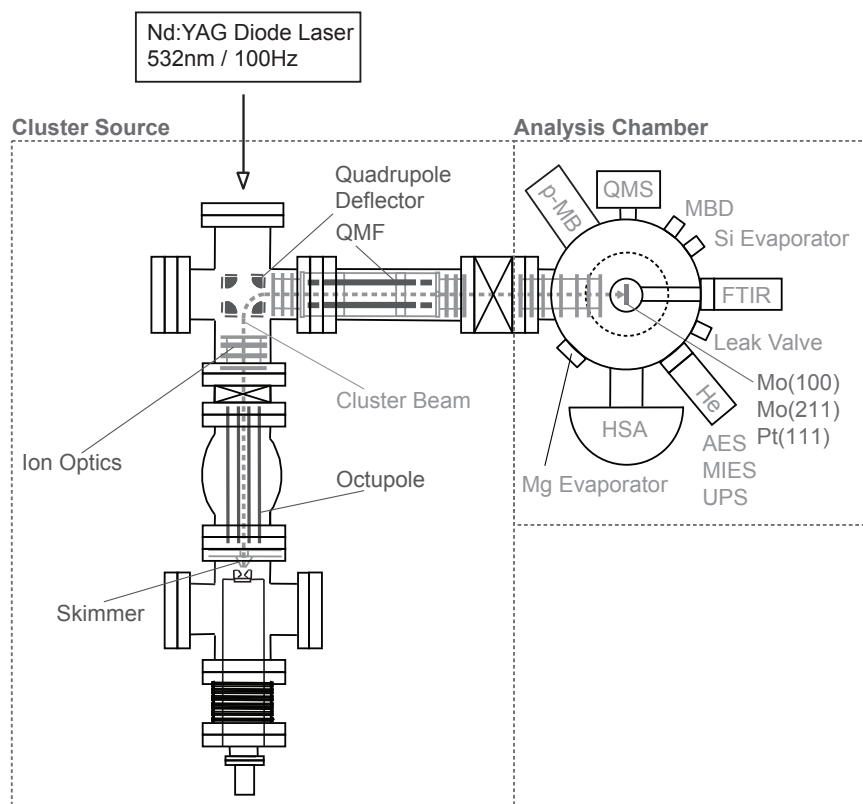


Figure 2.1: Schematic of the experimental setup used for this dissertation including analysis chamber (right) and cluster source (left). Further details about applied techniques and cluster production can be found in this chapter.

and resistively heated to ≈ 1300 K. In case of higher required temperatures, a home-built electron-gun could be used for heating the samples to 2000 K.

2.1.1 Infrared Reflection Absorption Spectroscopy

Vibrational spectroscopy has been performed by use of infrared reflection absorption spectroscopy (IRRAS, also referred to as IRAS and RAIRS). The basic instrument (Nicolet FT-6700, Thermo Electron Corp.) and setup is shown in figure 2.2. In short, the IR beam emitted by the globar of the spectrometer, which is purged by $N_2(g)$, is focused by a set of mirrors and guided into the UHV chamber. The focusing chamber is evacuated by a rotary pump to 10^{-3} mbar. The IR beam impinges the single crystal in the main chamber (base pressure 10^{-10} mbar) at grazing angle and is reflected towards an external focusing lens and a mercury-cadmium-telluride detector (MCTA-TRS, Thermo Electron Corp., cooled by LN_2). To minimize the influence of stray light, an aperture is set between the focusing window and detector. The measurements were performed in single reflection mode without s - p polarization of the IR beam.

A detailed theoretical and instrumental review of this well-established method was given by Hoffmann in 1983 [103] and the application of IRRAS for the investigation of model catalytic

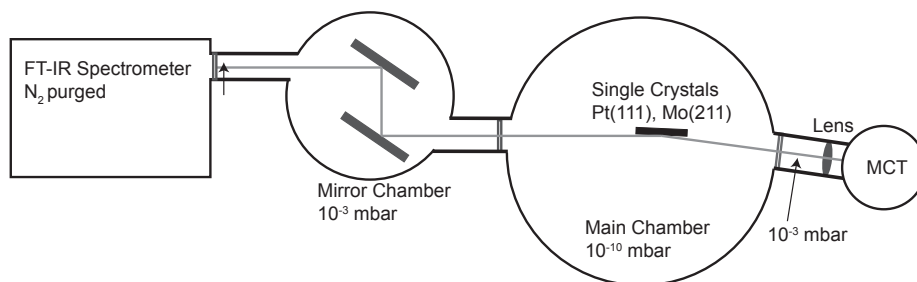


Figure 2.2: Experimental setup for infrared reflection absorption spectroscopy (IRRAS): The focused IR beam emitted by the spectrometer is reflected by the single crystal at glancing angle ($\approx 85^\circ$ with respect to the surface normal) and detected by an external MCT detector.

systems focusing on nanoparticles was summarized by Wilson and Brown [104]. Two important points should be mentioned for understanding the results presented in the following chapters [103, 105]: The incident light should be reflected at the metal surface at grazing incidence, which is caused by the reflectivity of the surface. Only p polarized (parallel to the plane of incidence) light can excite vibrations with a dipole moment perpendicular to the surface. The latter is known as the surface selection rule of IRRAS and can give important information about adsorption geometries by presence of characteristic vibrations or the absence thereof. For instance, the $\text{C}\equiv\text{C}$ vibration of asymmetric, terminal alkynes¹ can be observed at 2260 to 2100 cm^{-1} . If this band is observed in an IRRA spectrum, the molecule must adsorb in a geometry, in which the $\text{C}\equiv\text{C}$ bond is partly perpendicular to the surface plane. This allows detailed investigations of surface species, their adsorption geometries, coverage effects and temperature stabilities [50, 106–109].

2.1.2 Electron Emission Spectroscopies

Three spectroscopic techniques based on the emission of electrons have been used in this thesis, including Auger electron spectroscopy (AES), ultraviolet photoelectron spectroscopy (UPS) and metastable impact electron spectroscopy (MIES). All three methods have in common that the electrons being emitted are detected according to their kinetic energy E_{Kin} , whereas the excitation source, underlying physical processes and surface sensitivities vary. Each method is shortly introduced and experimental details are given.

As already indicated by the name, AES is based on the Auger effect, which is induced after creation of a (inner) core hole of the sample atom. Here, the hole can be created either by photons (soft X-rays) or electrons between 1 to 10 keV. In this work, an electron gun ($E_{\text{Kin}}=3$ keV) was used to induce these holes, which destabilize the corresponding atom. During the Auger process, the de-excitation to the ground state proceeds *via* filling of the hole by an outer shell electron², where the released energy is transferred in a radiation-less process to a second

¹The according vibrations of symmetric alkynes are hardly detectable due to symmetry leading to small dipole moments.

²An alternative relaxation mechanism based on the emission of photons is not considered here.

electron, which is emitted from the surface. The kinetic energy of these electrons is measured by a hemispherical analyzer (HSA, VSW HAC 150). Since three distinct energetic levels are involved in this process, the kinetic energy of the Auger electron is characteristic for an element and can be used for qualitative and quantitative analysis (under the assumption of a structure model as performed for hexynes on Pt(111) in this thesis). As the signals caused by Auger electrons are superimposed by a background of secondary electrons, it is convenient to use a lock-in technique for better visibility. As a result of this technique, the Auger spectra are shown in the derivative form dN/dE .

In contrast to AES, UPS is based on the photoelectric effect, in which interaction between photons and matter leads to ejection of photoelectrons. The photons employed are typically in the range of 20 to 40 eV (in this work He I α , 21.2 eV) and consequently the valence structure of the solid and/or adsorbates is probed. Here, the emitted electrons must satisfy both, conservation of energy and of momentum, and give information about the joint density of states (JDOS), which represents a convolution of densities of unoccupied and occupied states, respectively. The real band structure is only available by angular resolved ultraviolet photoelectron spectroscopy (ARUPS) or by change of excitation energy. None of these two experiments have been performed in this thesis and therefore the interested reader is referred to references [110–112]. Emission of photoelectrons is commonly described by a three step model, the details of which can be found elsewhere [113]. The surface sensitivity of AES and UPS are both determined by the mean free path of electrons in the solid, which is described by the universal curve as a function of kinetic energy. Since the mean free path is in both cases longer than the thickness of an atomic monolayer, the resulting spectra of UPS and AES contain information not only about the outermost surface, but also the layers below.

MIES applies metastable, electronically excited He atoms, which have low thermal kinetic energy and interact with the solid surface using their excitation energy to eject electrons from the surface. Since the He atoms do not penetrate into the bulk material, the electron emission takes place at the outermost surface selectively, in contrast to averaging techniques such as UPS and AES. Further information about electron spectroscopy using metastable atoms and de-excitation mechanisms can be found elsewhere [114].

The MIE/UP spectra in this work were recorded simultaneously using the setup described in previous publications and originally designed by Kempster [115–117]. A two-stage He-discharge source generates UV photons and excited, metastable He atoms. Using a time-of flight separation, a chopper is applied to separate photons from metastable atoms and thereby generating two signals, which originate from the two different processes resulting in photoelectrons being emitted from the surface. The determined binding energies are transformed to ionization potentials (IPs) by adding the work-function determined for the clean Pt(111) crystal in the case of hexynes [116, 118]. The peaks in the resulting spectra are fitted using a convolution of Lorentzian and Gaussian line shape (Voigt functions). Detailed information about data treatment can be found elsewhere [116].

2.1.3 Temperature-Programmed Desorption and Reaction

Temperature-programmed desorption and reaction (TPD/R) are common surface science methods. Applied under UHV conditions, different molecules are adsorbed on the surface of interest at cryogenic temperatures and a constant heating ramp is applied, during which desorbing species are identified by e.g. mass spectrometry. The differentiation between TPD and TPR is fluent, as only the most simple desorption experiments can be classified as real TPD experiments. In most cases additional reaction pathways exist besides desorption even for initially pure adsorbates. This is especially true for hydrocarbons on transition metals, which exhibit pathways like isomerization, dehydrogenation, and self-hydrogenation as will be shown in chapter 3. The relative rate of desorption r can be given by:³

$$r = -\frac{d\theta}{dt} = k_{des} \cdot \theta^n = \nu(\theta) \cdot \theta^n \cdot \exp\left(-\frac{E_{Des}(\theta)}{R \cdot T}\right) \quad (2.1)$$

with θ coverage, k_{des} reaction rate constant for desorption, ν pre-exponential factor, n order of desorption, E_{Des} desorption energy, R gas constant and T temperature. $\frac{d\theta}{dt}$ is proportional to change in temperature, since a linear heating ramp is applied. Further details about experimental details and analysis can be found in the literature [119–121].

In this work, a QMS (Balzers QMA 430, Liechtenstein) was used to monitor desorbing species during TPR/D and a constant heating rate between 2 and 2.5 K/s was applied by resistive heating. The single crystals were placed approximately 5 mm in front of the skimmer leading to the differentially pumped QMS stage. One final remark concerns the difficulty to obtain kinetic data by means of TPR data as the experiments are not performed under steady-state conditions: the absence of one particular product characteristic for a single reaction pathway, e.g. hydrogenation of alkynes as shown in chapter 4, does not exclude the possibility for this pathway to occur under isothermal, steady-state conditions, since the experiments scan available reaction pathways according to their activation energy. If for example the activation energy for desorption E_{Des} is smaller than the one for hydrogenation E_{Hyd} , no hydrogenation products are detected due to previous desorption.

2.1.4 Pulsed Molecular Beam Reactive Scattering

In order to overcome the limitations of TPR/TPD experiments, pulsed molecular beam reactive scattering (p-MBRS) experiments can be used to extract valuable kinetic information. As was recently stated by Zaera in his review, to date, the use of molecular beams remains one of very few approaches available to surface scientists for the measurement of the kinetics of reactions on surfaces in a systematic way [122]. During these experiments, the surfaces are kept at constant temperature (isothermal) and precise amounts of gases are pulsed periodically onto the surface. The desorbing species/products are monitored mass spectroscopically using the setup described for TPD/R experiments [123, 124]. Partial pressures of different products can be determined

³Under the assumption of infinite pumping speed of the QMS in order to avoid re-adsorption.

within the quasi steady-state region after calibration. Knowing the coverage of nanoparticles or clusters allows turn-over frequencies (TOFs) to be calculated after normalization. The pulsed valve apparatus is of in-house design and described elsewhere [125]. Two types of p-MBRS experiments have been performed for this work: ethylene and acetylene hydrogenation. The ethylene hydrogenation was performed as described in detail by Crampton [43]. Due to the presence of several reaction pathways, the acetylene hydrogenation presented in chapter 7 required additional calibration and a reaction model, which are both described in the specific experimental section.

2.1.5 QMS Calibration

Two factors have to be taken into account in order to calibrate the QMS for different gases: the sensitivity factor of the ion gauge and of the QMS. The sensitivity factor of the ion gauge (S_{ion}) is used for measuring the pressure inside the UHV chamber. This factor depends on gas composition and on the original calibration, which is usually carried out using a defined background of certain gases. Most of the sensitivity factors S_{ion} used in this work are taken from the users manual. The correlation between the real pressure (p_{real}) and the measured pressure (p_{meas}) is given by:

$$p_{real} = p_{meas}/S_{ion} \quad (2.2)$$

Two steps are necessary in order to correlate a measured ion current to a certain number of molecules. The first one is the measurement of a known number of molecules desorbing from a surface during a TPD experiment. In this case the Pt(111) surface covered by CO was used. The single crystal ($1.15 \cdot 10^{15}$ surface atoms per cm^2 , 0.785 cm^2 area of single crystal) is covered by $8 \cdot 10^{14}$ CO molecules, which give rise to an area of $2.35 \cdot 10^{-7} \text{ A}\cdot\text{s}$ during TPD measurement [43].⁴ The second step is to install identical fluxes through the skimmer of the QMS for different gases of interest and to measure the QMS response. The flux F in collisions per cm^2 through the aperture can be calculated using:

$$F = 2.64 \cdot 10^{22} \frac{p_{real}}{\sqrt{TM}} \quad (2.3)$$

where M is the molar mass in g/mol and T the temperature in K. The reference flux is the background corrected QMS response for CO at a pressure p_{set} of $5 \cdot 10^{-8} \text{ mbar}$, so the real pressure is $p_{real} = 4.76 \cdot 10^{-8} \text{ mbar}$ using S_{ion} . Using the sensitivity factors reported in the users manual, the QMS response is measured for different gases after installing the same flux. The ratio of the QMS current measured for CO and the gas of interest can now be calculated and is called the sensitivity factor of the QMS, S_{QMS} .

⁴The unit $\text{A}\cdot\text{s}$ is linearly correlated to $\text{A}\cdot\text{K}$, since a linear heating ramp was used.

Gas	S_{QMS}	Gas	S_{QMS}
1-hexyne	2.94	3-hexene	5.05
3-hexyne	3.50	hexane	1.21
1-hexene	6.55	benzene	0.45

Table 2.1: Sensitivity factors of C_6 -molecules determined by QMS calibration. The *cis* and *trans* isomers of 3-hexene have an identical cracking pattern and consequently sensitivity factors.

$$S_{QMS} = \frac{I(CO)}{I_C(x)} \quad (2.4)$$

The factor S_{QMS} is independent of the ion gauge and can be used to convert a measured TPD area for any calibrated gas in reference to CO and to a defined amount of molecules. A summary of C_6 sensitivity factors determined in this work is given in table 2.1. The advantage of these sensitivity factors over importation of cracking patterns from databases, e.g. NIST, is that the transmission function of the QMS does not have to be known and the pressure dependence is usually small. Furthermore it is directly correlated to the used instrument including specific parameters, e.g. ionization voltage (90 eV).

If $S_{QMS} > 1$, as it is the case for most gases used in this work, a higher current/area of CO would be measured in comparison to the gas of interest for the same flux of molecules. In other words, a higher S_{QMS} factor results in the loss of sensitivity caused e.g. by fragmentation patterns of hydrocarbons. The opposite holds true if $S_{QMS} < 1$ as observed for benzene, since this molecule hardly fragments during ionization. The area of an arbitrary gas $A(x)$ measured during TPD can now be converted to an absolute amount of molecules ΔN based on the calibration of CO:

$$\Delta N = \frac{A(x)}{A(CO)} \cdot 8 \cdot 10^{14} \cdot S_{QMS} \quad (2.5)$$

2.1.6 Film Synthesis and Characterization

Two thin amorphous silica films (abbreviated a-SiO₂) and a MgO(100) film have been synthesized as support material for Pd nanoparticles and size-selected Pt_n clusters. Experimental synthesis and characterization are described in the following for each film.

2.1.6.1 a-SiO₂ on Pt(111)

The Pt(111) crystal (MaTeck, Germany) was cleaned by repeated cycles of Ar⁺ sputtering (T=900 K, p(Ar)=5 · 10⁻⁶ mbar, U=1 keV, I=10 μA), followed by oxidation (T=650 K, p(O₂)=5 · 10⁻⁷ mbar) and annealing *in vacuo* (T=1300 K). The a-SiO₂ film was prepared by electron-beam evaporation (Tetra, Germany) of a silicon rod (99.999% purity, Alfa-Aesar, Germany) in an oxygen background pressure (T=400 K, p(O₂)=2 · 10⁻⁶ mbar) and subsequent annealing (T=1200 K,

$p(\text{O}_2)=2 \cdot 10^{-6}$ mbar). Detailed mechanistic considerations about the film growth can be found in reference [126].

2.1.6.2 a-SiO₂ on Mo(211)

The a-SiO₂/Mo(211) system was synthesized according to a modified route of Goodman et al. [127]. The same procedure as described for Pt(111) was used during silicon evaporation, after cleaning the single crystal by electron bombardment ($T=1860$ K) and oxidation ($T=900$ K, $p(\text{O}_2)=4 \cdot 10^{-7}$ mbar). After deposition of silicon, the film was annealed in oxygen to 1050 K ($p(\text{O}_2)=2 \cdot 10^{-6}$ mbar) in order to retain the amorphous character of the film and to avoid sublimation of SiO_x species at higher annealing temperatures [128].

2.1.6.3 MgO on Mo(100)

The MgO(100) film was grown on a Mo(100) single crystal. Prior to film preparation the molybdenum crystal was cleaned by electron bombardment (2000 K, 30 s) and oxidation (900 K, $p(\text{O}_2)=4 \cdot 10^{-7}$ mbar, 10 min). Film preparation was conducted by evaporation of a magnesium ribbon (99.5% purity, Merck Germany) in an oxygen background ($p(\text{O}_2)=5 \cdot 10^{-7}$ mbar) at 600 K. Afterwards the sample was annealed to 800 K for 10 min in order to minimize defect sites by reordering the film. The resulting support had a thickness of 8 – 10 ML (monolayers) and determined defect-poor. The cleanliness of the single crystal and the synthesized film was controlled via Auger electron spectroscopy. Further details about film preparation and characterization can be found in references [116, 129, 130].

2.1.6.4 Comparison between a-SiO₂ on Pt(111) and Mo(211)

The spectroscopic characterization of the two thin films is presented in figure 2.3. The amorphous character of both a-SiO₂ thin films is shown with IRRAS measurements, which exhibit vibrational bands at 1238 and 1252 cm⁻¹ and a broad shoulder down to 1100 cm⁻¹ associated with asymmetric longitudinal phonon vibrations. Additionally, the a-SiO₂/Mo(211) exhibits a band at 1051 cm⁻¹ caused by Mo-O-Si vibrations, which in turn means, that in contrast to the platinum system, a chemical bond is formed between oxygen and the underlying molybdenum. As can be seen in the Auger spectra of figure 2.3 b), no oxidation state other than (IV) is found for silicon and both films are stoichiometric. Based on these spectra, an average thickness of approximately 8 ± 4 Å was determined, where the large uncertainty is caused by the amorphous character of the films and the unknown mean free path of the photoelectrons (approximately 10 Å in the case of a-SiO₂ [131]). The UP/MIE spectra of the two films are shown in figure 2.3 c). Here, the absence of emission just below E_F in the MIE spectra demonstrated negligible amounts of defect sites.

To further characterize the surface of the synthesized films, TPD experiments of probe molecules were performed. The results are shown in figure 2.4 for a) NH₃, b) D₂O and c) CO. The routinely performed D₂-TPDs for both supports are not shown, since they do not exhibit any

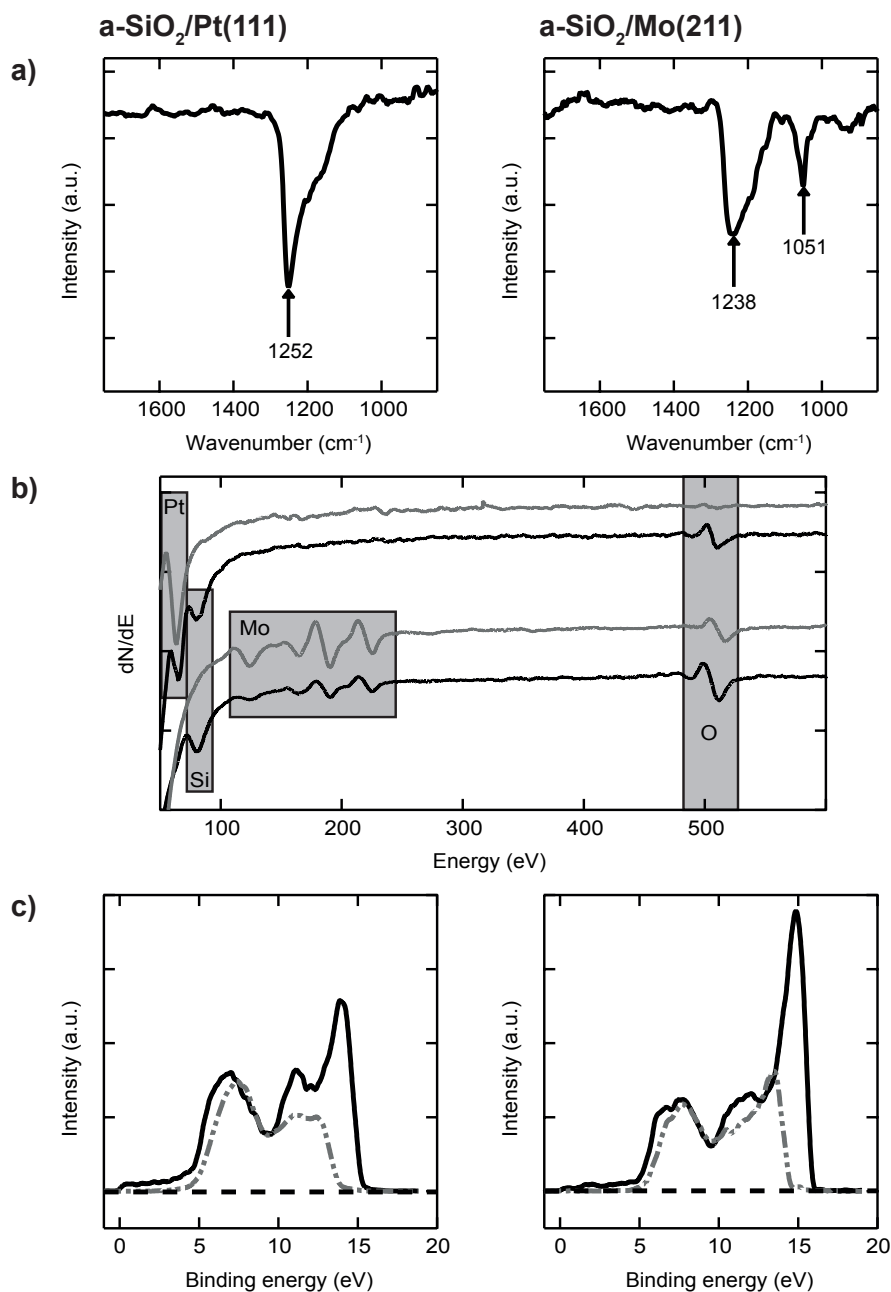


Figure 2.3: Spectroscopic characterization of $a\text{-SiO}_2$ supported on Pt(111) and Mo(211). The IRRAS data in a) show the amorphous character of both systems, whereas an additional band at 1051 cm^{-1} is characteristic for Mo-O-Si bonds. In subfigure b) Auger spectra of the clean single crystals and after film growth are presented. The MIE (dotted) and UP (solid) spectra after annealing are shown in c).

features. Desorption of physisorbed ammonia is observed below 150 K for a-SiO₂/Pt(111). On a-SiO₂/Mo(211), the desorption maximum shifts to 180 K. A single sharp desorption signal is detected for D₂O on a-SiO₂/Pt(111) in contrast to a-SiO₂/Mo(211), where no desorption occurs. The CO-TPDs of both supports show only physisorbed species below 150 K. A more detailed discussion about the films and their influence on supported clusters can be found in chapter 5, which also includes theoretical calculations.

2.2 Cluster and Nanoparticle Synthesis

A laser ablation source was used to synthesize size-selected Pt clusters and Pd nanoparticles [71]. In short, the second harmonic of a Nd:YAG (100 Hz, 532 nm, Innolas Spitlight DPSS, Germany) is focused onto a rotating metal target (99.95%, Alfa-Aesar for Pt, 99.95%, ESG Edelmetalle for Pd) producing a metal plasma, which is subsequently cooled by a delayed He-pulse (6.0 purity, Westfalen, Germany) and supersonic expansion into vacuum. The resulting cluster ions are guided by ion optics and an octupole ion guide to a quadrupole bender, where only positively charged clusters are transmitted into the analysis chamber (see figure 2.1). Negatively charged clusters are guided into the opposite direction, whereas the direction of neutral clusters remains unchanged. Consequently, both, neutral and negatively charged, clusters can be neglected and the settings of the bender unit can be used to preselect a mass range.

The cations are guided by Einzel lenses to an additional QMF (quadrupole mass filter, 16.000 amu, Extrel, USA), where mass-selection down to a single cluster size is achieved. A mass scan of size-selected Pt_n⁺ cations during optimization is shown in figure 2.5 a). It should be noted, that the m/z ratios of the clusters contain a certain offset, since the QMF is not calibrated. In order to achieve atomic resolution, the U/V ratio of the QMF has to be adjusted to ensure baseline-separation.

The size-selected clusters are further transmitted by Einzel lenses into the main chamber of the UHV setup. Here, they are deposited onto the support material of choice under soft-landing conditions (kinetic energy < 1 eV per cluster atom). These conditions ensure that the clusters remain intact upon deposition and fragmentation can be excluded. The kinetic energy of the clusters can be measured by retarding field analysis (RFA), which is shown in figure 2.5 b) for Pt₁₃⁺. Here, the cluster current is recorded as a function of the applied voltage on the sample holder. The negative derivative leads to the kinetic energy distribution of the clusters, which is approximately 3 eV as can be seen in figure 2.5 b). The neutralization current on the sample is recorded *via* a picoammeter (Keithley Instruments) assuming unit charge per cluster and can be used to calculate coverages.

In the case of Pd nanoparticles used in chapters 6 and 7, the QMF was operated in the *R.F. only mode*, which led to the QMF functioning as a high-pass mass filter. For a detailed discussion about the working principle of the *R.F. only mode* the reader is referred to reference [110]. The influence of cluster source settings on the obtained size distribution is shown in figure 2.6 a) for two mass ranges. With the settings of the cluster source used in those chapters, the resulting

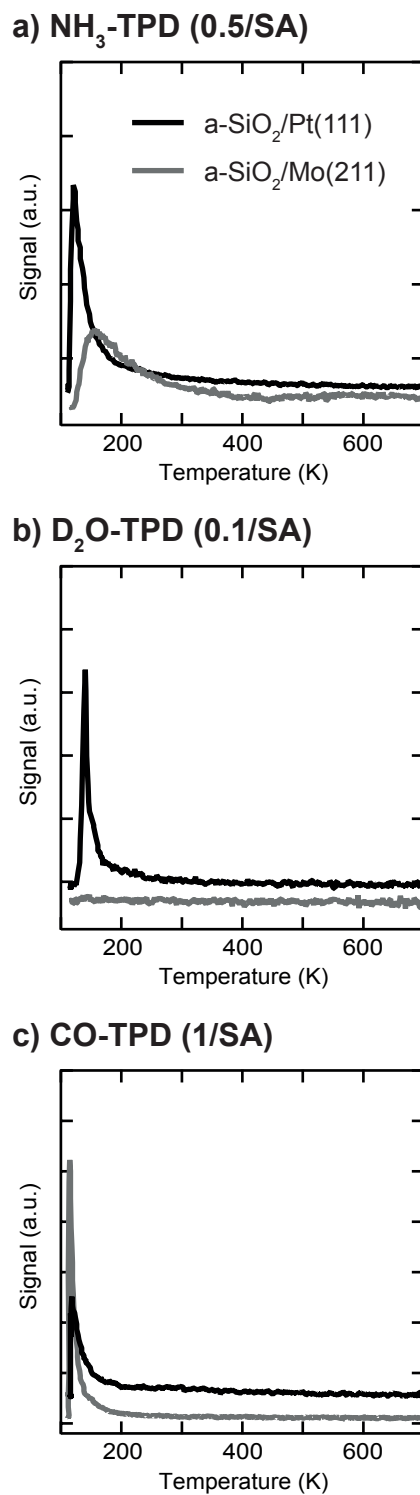


Figure 2.4: TPD of probe molecules on a-SiO₂ supported on Pt(111) and Mo(211): The amount of dosed molecules are given per surface atom (SA). For NH₃-TPD $m/z=17$ was monitored, for D₂O $m/z=20$ and for CO $m/z=28$.

particle distribution can be fitted by a log-normal function as evidenced by TEM studies [132, 133]:

$$y = y_0 + A \cdot \exp \left[- \left\{ \frac{\ln(x/x_0)}{\text{width}} \right\}^2 \right] \quad (2.6)$$

The results of this fit are presented in figure 2.6 b). The minimum particle size, which can pass the QMS, was set to be Pd₂₀, and the maximum of the size distribution was found for Pd₂₆. The Pd nanoparticles are consequently in the size regime of 0.9 to 1.4 nm.

2.3 Specific Experimental Procedures

2.3.1 Surface Chemistry of Hexynes on Pt(111)

The Pt(111) crystal was cleaned as described previously. Due to the formation of dehydrogenated carbonaceous species at high temperatures the single crystal was repeatedly cleaned after each single measurement.

All chemicals (Sigma-Aldrich, Germany, > 99.8% purity) were checked towards the absence of benzene and hexenes by GC-MS measurements and only additional stabilizers were found. The chemicals were further purified by repeated freeze-pump cycles prior to use and the cleanliness was monitored *in situ* with mass spectrometry. Dosage of chemicals was performed at 110 K using a calibrated molecular beam-doser originally designed by Yates *et al.* assuming unity sticking probability [134, 135]. The coverage is reported as adsorbed molecule per Pt surface atom (SA). The number of platinum surface atoms is presumed to be $\approx 1.15 \cdot 10^{15}/\text{cm}^2$ [136].

A linear heating ramp of 2.5 K/s was used for TPD measurements. The cracking patterns of 1/3-hexyne, 1/3-(cis/trans)-hexene, hexane, benzene and hydrogen were determined *in situ* by backfilling the chamber and are in good agreement with the NIST database (below 5% deviation). Due to the high ionization voltage of the QMS (~ 90 V) the following m/z ratios were used for identification rather than the molecular m/z ratios: 2 for hydrogen, 57 for hexane, 69 for hexene and 78 for benzene. Simultaneous recording, e.g. of 69 and 84 for hexene, confirmed the applied characteristic m/z ratios. Desorption of hexynes was monitored using $m/z = 67, 81$ and 82 in order to disentangle the possible formation of hexadienes and cyclohexene because of similar cracking behavior. After TPD to 800 K an Auger spectrum was recorded to determine the total amount of carbonaceous species on the single crystal [137].

The IRRAS experiment was performed by dosing 1.6 L ($1 \text{ L} = 1.33 \cdot 10^{-6} \text{ mbar} \cdot \text{s}$) of 1-hexyne at 100 K and averaging 1024 scans at 4 cm^{-1} resolution. The ion gauge sensitivity, which is a factor of 6.2, is taken into account for dosage. The resulting spectra are base-line corrected.

2.3.2 3-Hexyne on Size-Selected Pt Clusters

The cluster coverage was varied from 0.8% ML (Pt₃) to 0.3% ML (Pt₁₃) for better comparability of the metal loading on the support. After deposition the temperature of the samples was shortly

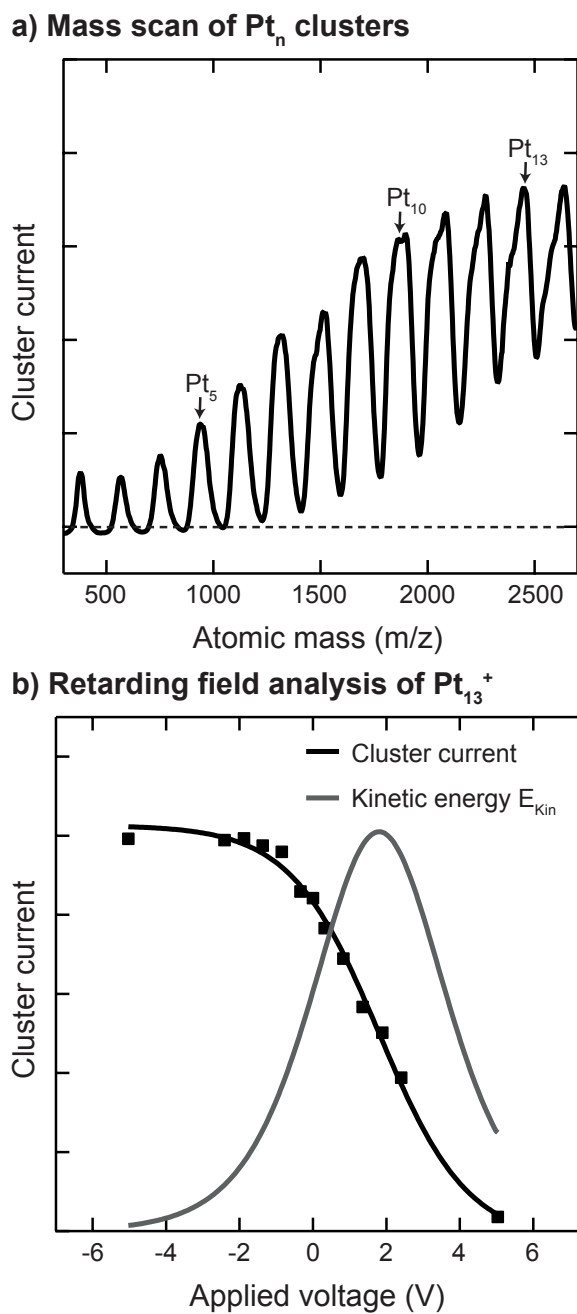
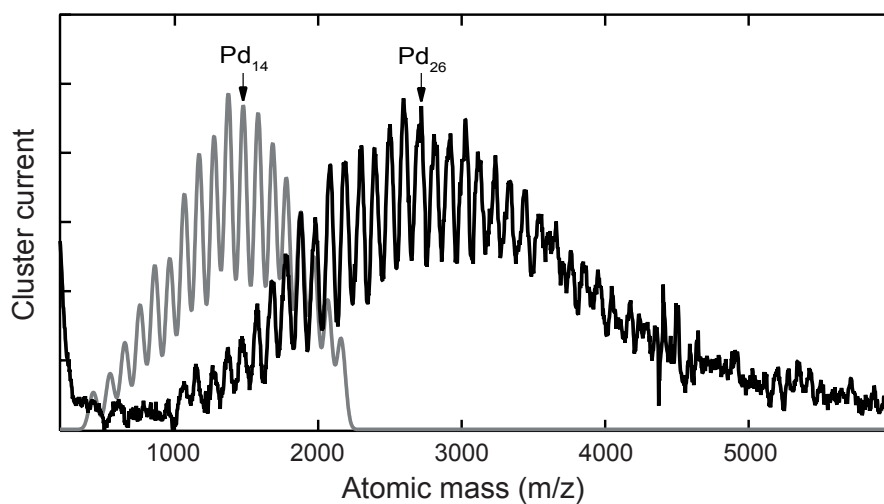


Figure 2.5: Mass scan of size-selected Pt_n^+ clusters (a) and retarding field analysis for Pt_{13}^+ (b). Further details are given in the main text.

a) Tuning of the cluster source



b) Pd nanoparticles

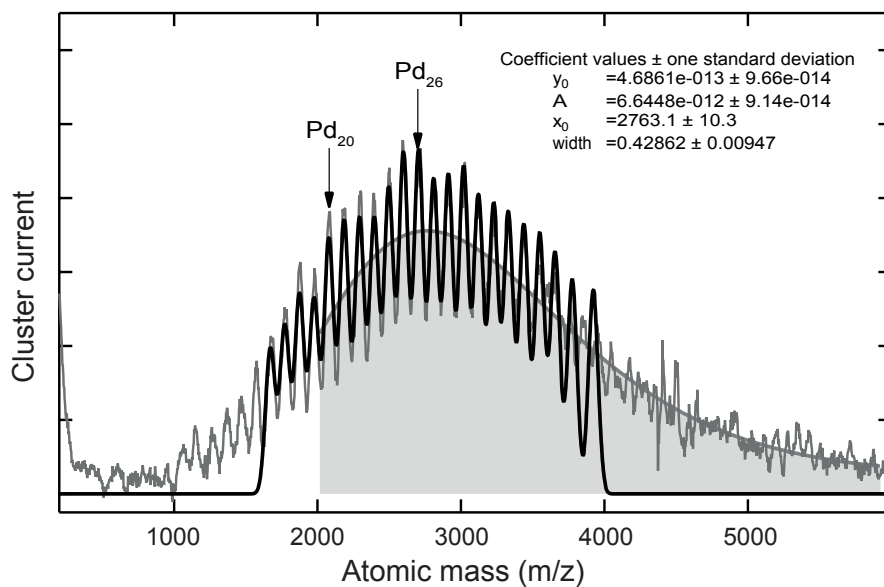


Figure 2.6: The influence of cluster source settings on size distribution are shown for Pd clusters and nanoparticles in a). In subfigure b), the size distribution of Pd nanoparticles used in chapter 6 and 7 is fitted by a log-normal function and marked in grey.

increased to 300 K. In order to compare activities, the same experiments were also performed on a clean Pt(111) single crystal.

A heating ramp of 2 K/s was used for TPR measurements after dosage of gases. The reported dosages are given per surface atom (SA) of the MgO support assuming $2.25 \cdot 10^{15}$ atoms/cm². For all experiments 0.4/SA D₂ was dosed first followed by 0.22/SA 3-hexyne. The areas determined by TPR experiments were corrected using QMS sensitivity factors determined for each molecule. The following *m/z* ratios were used for identification: 86 for d₂-hexene, 90 for d₄-hexane, 78 for benzene and 69 for H₂-hexene (correlating to the ion CH₃CH₂CH=CHCH₂⁺). The benzene trace has been baseline-corrected for the overlapping cracking pattern of physisorbed 3-hexyne at low temperatures. The presented error bars were determined from multiple measurements on a single cluster size.

2.3.3 Ethylene Hydrogenation on Size-Selected Pt Clusters

All experimental details required to understand the results are presented in the respective chapter 5. Further information about film preparation can be found in subsection 2.1.6.

2.3.4 Ethylene Hydrogenation on Pd Nanoparticles

The coverage of $4.5 \cdot 10^{12}$ particles per 0.785 cm² single crystal (unless otherwise stated) was used for all experiments. After deposition, the samples were flashed to 300 K.

For D₂-TPD, a total of $9 \cdot 10^{12}$ Pd particles were used and varying amounts of D₂ were dosed at 100 K. A linear heating ramp of 2.5 K/s was then applied and the ion signal of 4 *m/z* was recorded.

The p-MBRS experiments were performed at 300 K using a piezo-driven valve of in-house design, which is used to pulse ethylene (C₂H₄, 3.5 purity, Westfalen Germany) in a highly reproducible, well-defined manner (*f*= 0.1 Hz, 0.6 ms pulse width) in a background pressure of $2 \cdot 10^{-6}$ mbar D₂ within the UHV chamber [34, 123, 138]. The partial pressure of C₂H₄ was determined to be $5 \cdot 10^{-7}$ mbar within the pulse and consequently all experiments are performed in excess deuterium. In order to disentangle the formation of stoichiometric product C₂H₄D₂ and ethane, which additionally underwent HD-exchange (e.g. C₂H₃D₃), the *m/z* ratios of 31 and 33 were recorded. The different cracking patterns of these two molecules and the contribution of ¹³C was used to determine their relative abundance [139]. In general, $4.5 \cdot 10^{12}$ particles were used for activity measurements, except for the determination of *m/z* = 31 for Pd nanoparticles supported on a-SiO₂/Pt(111) due to the detection limit of the oscilloscope. For this reason, the coverage was stepwise decreased to $0.3 \cdot 10^{12}$ particles. Since the particles deactivate over the course of the experiment, a linear correlation was found between the number of deposited particles and the formed product at the end of the p-MBRS experiments. Consequently the TOFs reported here, which were normalized to the number of particles, are unaffected by the overall coverage.

For *post-mortem* TPR, the samples were cooled to 100 K and additional D₂ was dosed (1.6 per surface atom). The same procedure as described for pure D₂-TPD was then applied monitoring $m/z=2,3$ and 4. In a second step, the reaction was performed at 300 K on $9 \cdot 10^{12}$ particles using H₂ instead of D₂. Only afterwards, D₂ was dosed at 100 K and the same procedure applied.

In order to gain further insights into catalyst deactivation, IRRAS with CO as a probe molecule was performed. This method has often been applied to investigate the presence of carbon deposits on Pd and Pt [140, 141]. Spectra of Pd particles as deposited and after catalytic measurement described previously were collected at 100 K after dosing 10 L CO in single reflection mode (256 scans, 4 cm⁻¹ resolution). The resulting spectra were base-line corrected.

2.3.5 Acetylene Hydrogenation on Pd Nanoparticles

A coverage of $4.5 \cdot 10^{12}$ nanoparticles on the 0.785 cm² single crystals was used for all experiments.

A background pressure of $2 \cdot 10^{-6}$ mbar D₂ was established in the UHV chamber during p-MBRS experiments. A piezo driven valve (600 μs pulse width, 0.1 Hz) was used to pulse well-defined amounts of acetylene onto the sample. The local pressure during the measured quasi steady-state region for one pulse was determined to be $3 \cdot 10^{-7}$ mbar for acetylene (free of acetone, Linde AG, Germany) at 250 K. Consequently, all catalytic measurements were performed in excess of deuterium.

To investigate the effect of dehydrogenated C₂H_x species on the nanoparticles on catalytic activity, all experiments were performed twice, once with clean particles and once with C₂H_x precovered particles. Hydrogenation of ethylene was performed at 300 K *prior* to acetylene hydrogenation as described previously [138]. This reaction leads to formation of C₂H_x species on the particle surface (most likely ethylidyne, ethylidene and others) and possibly of a carbide.

Several m/z ratios were monitored in order to disentangle the formation of different reaction products. Due to the limited quasi steady-state region within one pulse (≈ 20 ms, see figure 2.7) and detection by quadrupole mass spectrometry, each m/z ratio had to be measured individually requiring highly reproducible film preparation and particle synthesis, enabled by the use of the cluster ablation source. Six different m/z ratios were measured: 30, 31, 33, 34, 54 and 78. The latter m/z ratio is the molecular mass of benzene formed by cyclotrimerization of acetylene. The $m/z=54$ ratio was used to monitor the desorption of C₄-molecules with 1,3-butadiene being the most abundant molecule. Due to the low amounts of benzene and C₄-molecules being formed during reaction, their contribution to lower m/z ratios by overlapping cracking patterns can be neglected. It should be noted, that due to the high exchange rate between hydrogen and deuterium, the given yield of benzene and C₄-molecules is rather qualitative than quantitative.

The m/z ratios of 30, 31, 33 and 34 have been used to discriminate between ethylene and ethane, which additionally underwent HD-exchange besides the stoichiometric reaction. It was recently shown that during the hydrogenation of ethylene on Pt(111) using D₂ not only the stoichiometric product ethane, C₂H₄D₂, is formed, but rather a statistical distribution of

deuterium content within the ethane molecule [16]. This statistical distribution of deuterium content within the product during ethylene hydrogenation implies the possible presence of over 16 different deuterated ethylenes and ethanes during the hydrogenation of ethyne [142]. Since the measurable mass to charge ratios are limited for this reaction, the whole system of possible desorbing species is classically under-defined in this case. However, careful data analysis allows at least general trends to be established.

Measurement of four m/z ratios allows four molecules to be included in the reaction network. Unfortunately, other m/z ratios like 32 (oxygen) and 28 (CO), which would be beneficial to data evaluation, could not be measured due to background noise. Two of these four molecules are attributed to the stoichiometric reaction products, ethylene-D₂ (*cis*) and ethane-D₄, which are the most abundant reaction products. The cracking ratios of stereoisomers (e.g. *cis* and *trans* of CHDCHD) are typically in the range of few percent and the error made by excluding these isomers is small compared to the uncertainty of the experiment [143]. The same line of reasoning allows to neglect contribution of ¹³C. Further molecules included are ethylene-D₃ and ethane-D₅, which additionally exchanged H by D. The cracking patterns of these molecules are transferred from references [139, 143] and the validation of this approach was additionally checked *in situ* by ethylene-H₄, ethylene-D₄ and ethane-H₆ (below 5% deviation).

The contribution of each molecule to one particular m/z ratio can be solved analytically. The recorded voltage, which is now corrected for different molecules, can be correlated to a partial pressure within the quasi steady-state region. Normalization to the amount of used nanoparticles allows to determine TOFs and the errors presented in the following are based on multiple measurements of each particular m/z ratio. The data evaluation is summarized in figure 2.7.

For *post-mortem* TPR, the samples were cooled to 100 K after acetylene hydrogenation at 250 K and 40 L of D₂ were dosed. The same experimental setup described for p-MBRS measurements was used, with a linear heating ramp of 2.5 K/s. For Pd nanoparticles supported on a-SiO₂/Pt(111), this experiment was also conducted for ethylene hydrogenation at 300 K followed by acetylene hydrogenation at 250 K.

The Pd nanoparticles were further characterized by IRRAS using CO as a probe molecule after reaction. After background measurement at 100 K, 10 L CO were dosed and a spectrum recorded (256 scans, 4 cm⁻¹ resolution). The base-line corrected spectra after reaction were either recorded directly after the 250 K reaction step or after five additional pulses at 300 K.

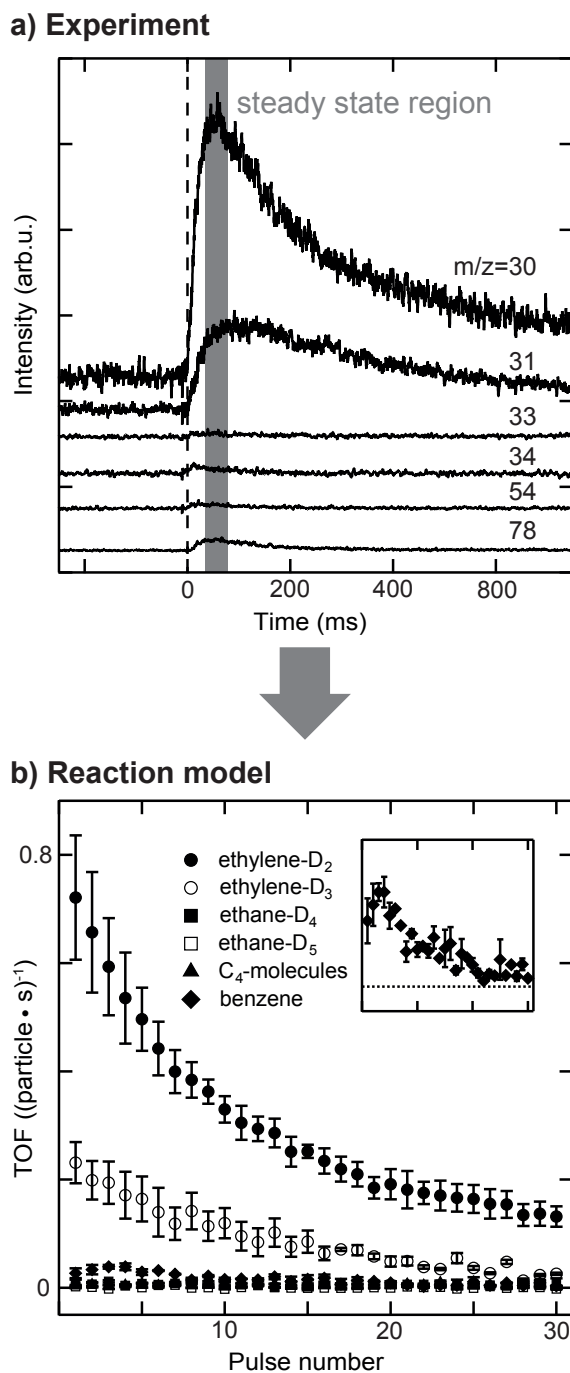


Figure 2.7: Experimental data acquisition and evaluation: A pulsed molecular beam reactive scattering technique is used to measure a quasi steady-state region for different m/z ratios during acetylene hydrogenation (a): average m/z ratios of 30 pulses are shown for a typical experiment, where the acetylene pulse starts at 0 s indicated by the dotted line. The contribution of individual molecules to one m/z ratio can be calculated by cracking pattern analysis. Normalization to the number of particles allows to determine TOFs as a function of pulse number (b). The inset exhibits a magnification of benzene formation.

SURFACE CHEMISTRY OF HEXYNES ON Pt(111)

The following chapter was published in the *Journal of Physical Chemistry C*. Reprinted with permission from *J. Phys. Chem. C* 122, 8, 2018, 4428-4436. Copyright 2018 American Chemical Society.

Despite their industrial use in selective hydrogenation reactions, the surface chemistry of long-chained alkynes on transition metals is not well understood. To this end the two C_6 -alkynes 1- and 3-hexyne were studied on Pt(111) using temperature programmed desorption (TPD), electron emission spectroscopies (MIES/UPS) and infrared reflection-absorption spectroscopy (IRRAS). Besides the formation of graphitic carbon residues, both molecules mainly undergo desorption, self-hydrogenation and dehydrocyclization to form benzene during temperature programmed desorption similar to the analogous alkenes. The dehydrocyclization to benzene is shown to be ubiquitous to unsaturated hydrocarbons on Pt(111) regardless of the degree of unsaturation and its position within the molecule. A reaction mechanism for dehydrocyclization is proposed based on dehydrogenation followed by ring-closure. This work extends the understanding of alkyne chemistry on Pt based catalysts and may aid to identify additional reaction mechanisms leading to undesired coke formation.

3.1 Introduction

The chemistry of hydrocarbons on transition metals is of major importance for many industrial relevant processes. Naphtha reforming is a prime example of such processes, which is used to increase the octane number of fuels by dehydrogenation, isomerization, aromatization and hydrocracking of alkanes containing six to ten carbon atoms [29]. Consequently, significant efforts have been put into understanding the underlying phenomena, which determine the overall chemistry. From a surface science point of view the chemistry of C_6 hydrocarbons on

different metal single crystals has been extensively studied under both, UHV conditions and under increased pressure conditions with a variety of different techniques such as temperature-programmed desorption (TPD) [37, 144–147], Auger electron spectroscopy (AES) [137, 148], infrared reflection absorption spectroscopy (IRRAS) [107, 149] and sum frequency generation (SFG) [150, 151].

This work is dedicated to study the chemistry of unsaturated, linear C_6 -hydrocarbons on Pt(111), while previous studies were mainly performed on cyclic- C_6 -membered hydrocarbons due to their possible role in dehydrogenation reactions [37, 148, 149, 152–154]. When a monolayer of hexane is adsorbed on Pt(111) at cryogenic temperatures under UHV conditions, its C–C bonds align parallel to the surface in a trans-trans-trans conformation characterized by two major bands at 2904 and 2929 cm^{-1} in an IR spectrum [155]. Increasing the temperature leads to molecular desorption at 240 K with a desorption energy of ≈ 14.8 kJ/mol and, due to the weak interaction between adsorbate and surface, no thermal decomposition can be observed [156]. In contrast to these UHV studies, adsorption of hexane on Pt(111) at 296 K under increased pressure conditions (1.5 Torr) leads to the formation of a π -allyl $c-C_6H_9$ species, which can be further dehydrogenated to form benzene at higher temperatures [150]. In the presence of excess hydrogen (15 Torr) the formation of this allyl-species is suppressed and heating up to 453 K results in various surface species including metallacyclobutane, metallacyclohexane and hexylidyne.

Hexylidyne is also identified by IRRAS under UHV conditions, when 1-hexene is adsorbed on Pt(111) at 240 K [157]. Heating above 333 K results in the formation of the metallocycle $Pt_3\equiv C-(CH_2)_5-Pt$, which can be further dehydrogenated to $Pt_3\equiv C-(CH_2)_4-C\equiv Pt_3$ above 373 K. The nature and amount of the desorbing species of 1-hexene on Pt(111) is not fully understood. During TPD a significant amount of 1-hexene (between 70 and 98%) undergoes dehydrogenation resulting in release of hydrogen and in formation of carbonaceous deposits on the Pt(111) surface, which is consistent with the formation of hexylidyne as a dominating surface species [137, 144]. Molecular desorption of 1-hexene is observed between 259 and 284 K and in one study also the desorption of benzene and hexane caused by dehydrocyclization and self-hydrogenation was observed in small quantities [137]. To the best of the authors knowledge the chemistry of the structural isomers 2- and 3-hexene on Pt(111) has not been investigated so far.

Little is also known about the surface chemistry of hexynes on Pt(111) under UHV conditions. IRRAS investigations were performed on Ru(0001) with an identical surface arrangement to Pt(111) [107]. Briefly, 1-hexyne readily forms a hexylidyne species even at 120 K on Ru(0001) analogously to 1-hexene on both surfaces [158]. Hexylidyne was not observed for 2- and 3-hexyne, which were found to be di- σ/π -bonded at low temperatures and underwent decomposition upon heating including scission of C–C bonds [159, 160].

Apart from these works, the chemistry of long-chained alkynes, in particular of hexynes, on metal surfaces under UHV conditions has received little attention, despite the industrial application of the very same metals in selective hydrogenation reactions [29]. Consequently this study aims at elucidating the surface chemistry of 1- and 3-hexyne on Pt(111) under UHV

conditions.

3.2 Results

3.2.1 TPD Studies of 1- and 3-Hexyne

TPD spectra of 1- and 3-hexyne on Pt(111) as a function of coverage are displayed in figure 3.1 and 3.2. For the lowest investigated coverage of 0.11/SA molecular desorption of chemisorbed 3-hexyne measured at $m/z = 67$ is observed in a single desorption peak centered around 333K (figure 3.1 a). This signal appears asymmetric at lower temperature due to an overlap with the cracking pattern of hexene, which is subtracted for quantitative analysis (background corrected traces can be found in the appendix). Increasing coverage leads to desorption of a physisorbed species at 120K. Almost no molecular desorption is measured for 1-hexyne at low coverages. From a coverage of 0.22/SA on, two molecular desorption peaks are identified, one sharp signal at 120K characteristic of physisorbed hexyne and one broad signal between 310 and 390K of chemisorbed 1-hexyne.

In figure 3.1 b) the desorption of alkenes during TPD is shown tracing $m/z = 69$. The alkenes are self-hydrogenation products caused by hydrogen released during the dehydrogenation of the alkynes. The main desorption peak of 3-hexene is located at 315K independent of coverage and for coverages higher 0.22/SA a shoulder at 250K starts to emerge. No information about the stereochemistry of the produced 3-hexene can be given, since *cis* and *trans* isomers possess almost identical cracking patterns in the QMS. The desorption of 1-hexene is observed at 330K at low coverages and shifts to lower temperatures for higher coverages. Additionally a second desorption peak located at 240K appears for higher coverages (0.33/SA and above).

The hydrogen release connected to dehydrogenation is displayed in figure 3.2 a). The lowest 3-hexyne coverage of 0.11/SA shows an onset of hydrogen production at 280K and two sharp, overlapping dehydrogenation signals at 330 and 361K, respectively. These two sharp signals are followed by a broad hydrogen signal ranging from 400 to 730K. Increasing the coverage of 3-hexyne, the low temperature signal at 280K vanishes, while simultaneously increasing the yield of self-hydrogenated hexene as shown in figure 3.1 b). For higher coverages (above 0.44/SA) an increased background is observed below 200K, which is caused by physisorbed 3-hexyne. For comparison, the hydrogen production of the two hexenes, *cis*- and *trans*-3-hexene, at a coverage of 0.22/SA are additionally shown. Both molecules display two signals at 240 and 350K followed by a broad, high temperature dehydrogenation signal up to 700K.

The hydrogen release of 0.11/SA 1-hexyne starts at 270K, which is lower than the temperature observed for the same coverage of 3-hexyne, and a maximum of hydrogen production is observed at 383K. Above 500K a broad signal is observed similar to the ones of 3-hexyne and the 3-hexenes. With increasing coverage the low temperature signal disappears and the second hydrogen signal shifts to higher temperatures (413K). In contrast to 1-hexyne, 1-hexene (0.22/SA) exhibits two sharp hydrogen signals at 243 and 364K.

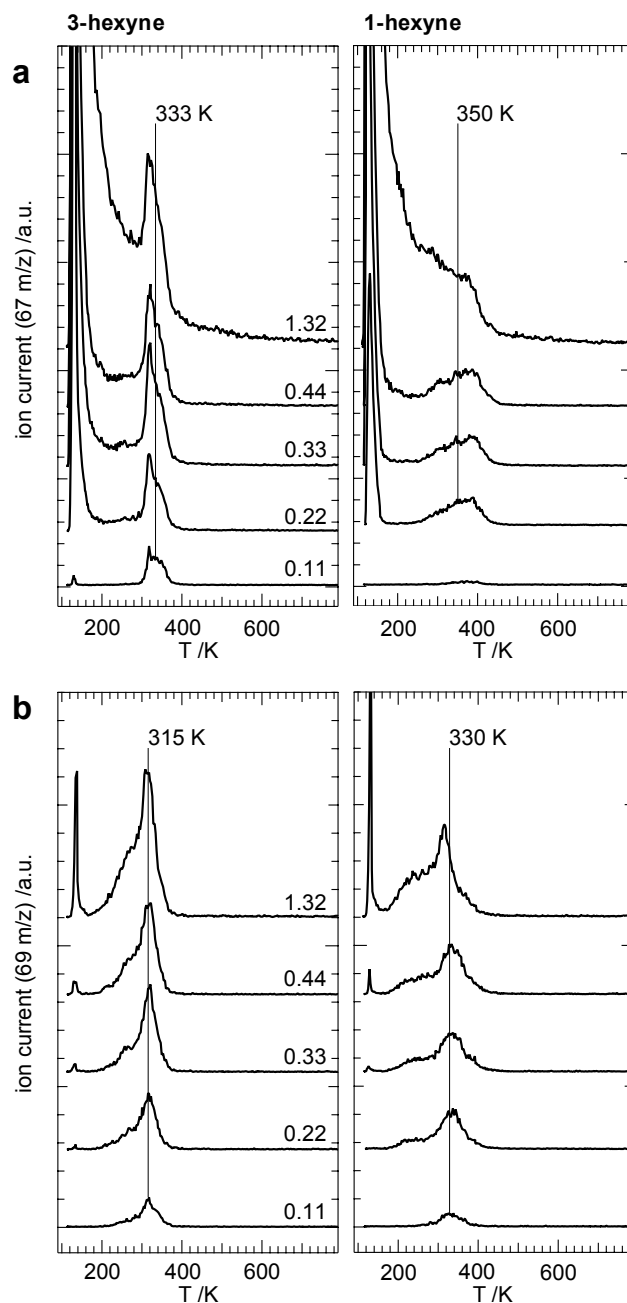


Figure 3.1: TPD studies of 3- and 1-hexyne on a Pt(111) surface as a function of alkyne coverage given in molecules/SA: trace $m/z = 67$ (alkyne desorption, a) and $m/z = 69$ (hexene desorption caused by self-hydrogenation, b). The signal of $m/z = 69$ at 120K is caused by the cracking pattern of the alkyne. Adapted with permission from *J. Phys. Chem.C* 122, 8, 2018, 4428-4436. Copyright 2018 American Chemical Society.

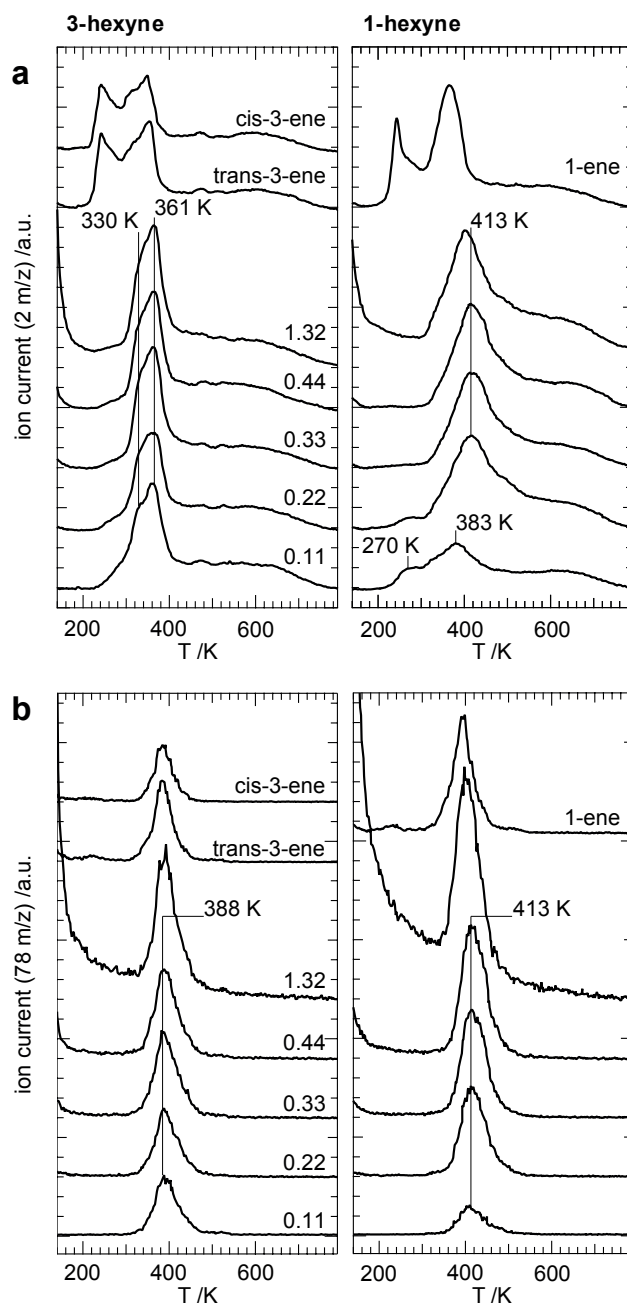


Figure 3.2: TPD studies of 3- and 1-hexyne on a Pt(111) surface depicting $m/z = 2$ (hydrogen desorption, a) and $m/z = 78$ (benzene formation, b). Additionally the same traces are shown for the according alkenes for comparison. The increased background at temperatures below 200 K originates from the contribution of physisorbed alkynes. Adapted with permission from *J. Phys. Chem.C* 122, 8, 2018, 4428-4436. Copyright 2018 American Chemical Society.

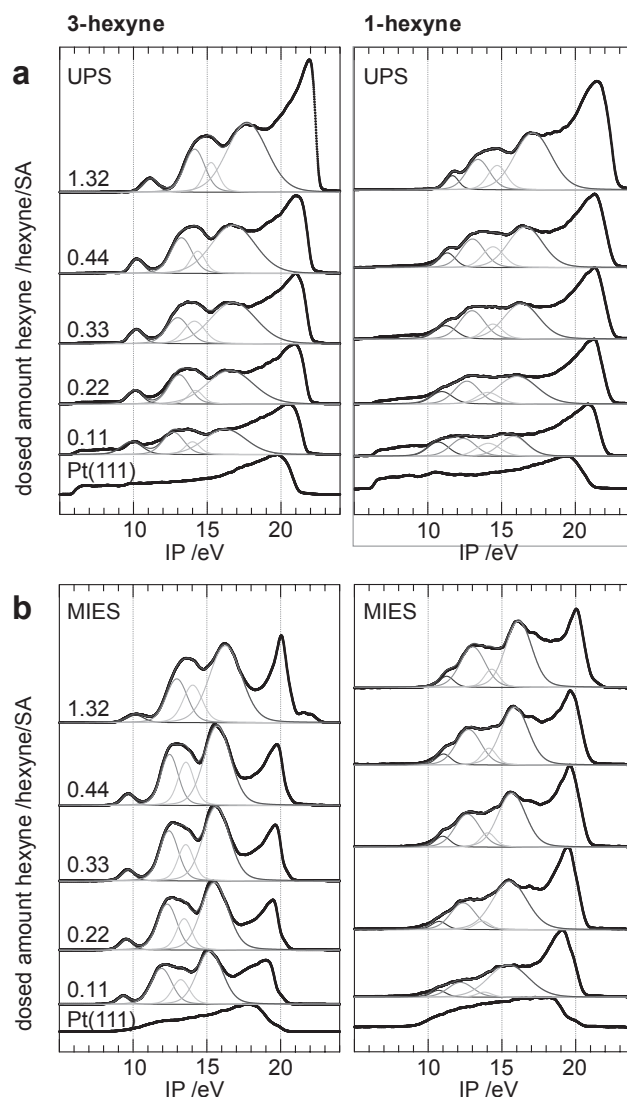


Figure 3.3: Coverage dependent UP (a) and MIE (b) spectra of 3- and 1-hexyne adsorbed on Pt(111) at 100K. The spectra are fitted by four peaks. Adapted with permission from J. Phys. Chem.C 122, 8, 2018, 4428-4436. Copyright 2018 American Chemical Society.

The dehydrocyclization leading to the formation of benzene ($m/z = 78$) is shown in figure 3.2 b). For a coverage of 0.11/SA 3-hexyne, the evolution of benzene peaks at a temperature of 388K. This temperature remains almost constant while the peak area grows with increasing coverage. The corresponding 3-hexenes also show the production of benzene at 383 and 384K for *cis* and *trans* isomers at a coverage of 0.22/SA, respectively. In contrast to 3-hexyne, the desorption temperature of benzene formation is 413K for 1-hexyne and 395K for 1-hexene.

3.2.2 MIES/UPS of 1- and 3-Hexyne

Figure 3.3 shows the MIE/UP spectra of the coverages used for the TPD experiments described previously. For higher coverages all spectra, MIES and UPS, contain at least four signals. The

signal around 20 eV can be assigned to secondary electrons emitted from the surface, which allows for extraction of the work function value (based on the binding energy). The remaining three signals can be interpreted assuming four peaks based on results obtained by UP spectra of 3- and 1-hexyne in the gas phase [161, 162]. Peak 1 at lowest IP can be assigned to emission from a molecular π -orbital, whereas peak 2, 3 and 4 are caused by emission of p- and s-orbitals or of σ_{CH} and σ_{CC} orbitals depending on nomenclature [162]. This interpretation is further supported by theoretical calculations, which can be found in the appendix. The envelope of the four fitted peaks is additionally shown. In the UP spectra of 3-hexyne it can be seen, that the first peak located at 10 eV is well separated from the remaining three peaks and can be observed even for the lowest coverage of 0.11/SA. In contrast to 3-hexyne, the first peak of 1-hexyne around 10.8 eV appears as a shoulder of the second peak. The according MIE spectra of the alkynes adsorbed on Pt(111) can be seen in figure 3.2 b). The same four signals as in the UP spectra are observed confirming the adsorbed alkynes as the origin of these signals due to strict surface sensitivity of the technique. Again the first signal of 3-hexyne is well separated whereas it appears as a shoulder for 1-hexyne. The signals of the MIE spectra are at lower IP than for UPS for 3-hexyne. This shift has been shown to be caused by a change in the excitation energy of the He atom as a function of the surface composition [163].

The coverage dependent work function of the two alkynes extracted from the UP spectra of figure 3.3 a) is given in figure 3.4 a). For the clean Pt(111) the work function is determined to be ~ 6.1 eV, which is in reasonable agreement with the literature value of 5.9 eV [164]. Upon increasing coverage of alkynes the work function is continuously decreased. For the highest coverage a maximum decrease of ≈ 1.5 eV is observed for both alkynes. The results of the fitting procedure are summarized in figure 3.4 b) for UPS and c) for MIES. The changes of the peak positions are given relative to the coverage of 0.44/SA, a coverage at which all peaks can be fitted well. All peaks within one coverage show the same shift with regard to the reference point regardless of UPS and MIES. Furthermore there is a strong correlation between the peak position determined by MIES and UPS for both hexynes.

3.2.3 IRRAS of 1-Hexyne

The IRRAS spectrum of multilayer 1-hexyne (1.6L) adsorbed on Pt(111) at 100 K is shown in figure 3.5. The observed vibrational bands and mode assignments are summarized in table 3.1, which also contains vibrational modes for 1-hexyne on Ru(0001) and hexylidyne on Pt(111) adopted from references [157, 165]. All vibrational modes observed for a multilayer of 1-hexyne on Ru(0001) [165] are also present on Pt(111). Two additional bands at 2858 and 1460 cm^{-1} are present for 1-hexyne on Pt(111), which may be assigned to $\nu_s\text{CH}_2$ and $\delta_{as}\text{CH}_2$, respectively. The origin of these bands is explained in the discussion section and further IRRAS spectra at higher temperatures can be found in the appendix.

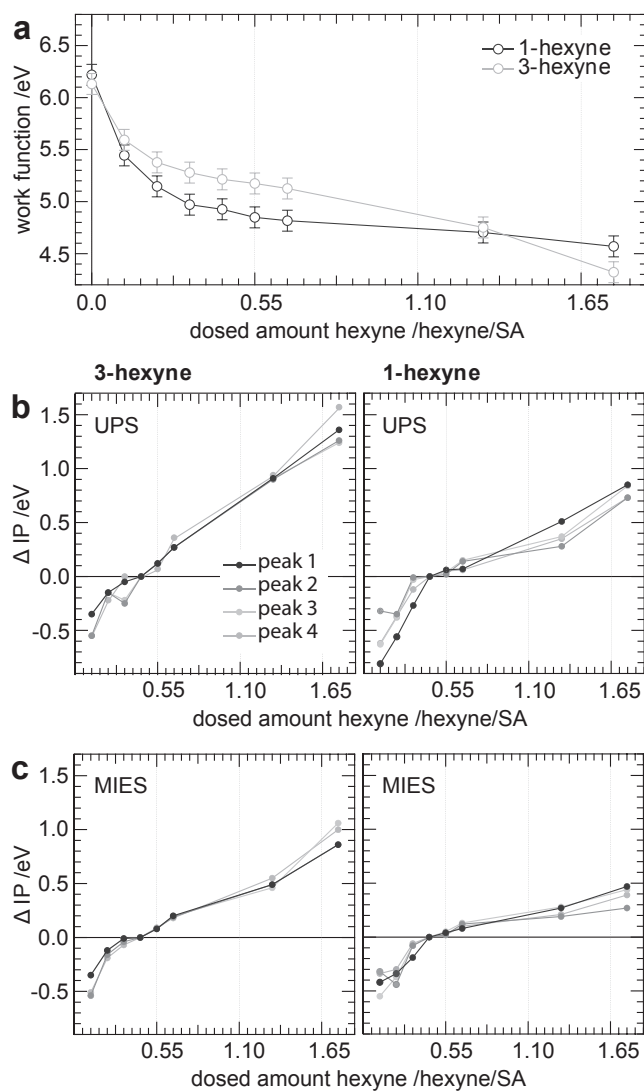


Figure 3.4: The change of work function as a function of alkyne coverage a). The relative change of ionization potential (IP) for the four signals extracted from figure 3.3 for UPS b) and MIES c). The peak positions determined for a coverage of 0.44/SA are used as a reference and peak 1 can be assigned to emission from a molecular π -orbital, whereas peak 2,3 and 4 belong to σ_{CH} and σ_{CC} orbitals, respectively. Adapted with permission from J. Phys. Chem.C 122, 8, 2018, 4428-4436. Copyright 2018 American Chemical Society.

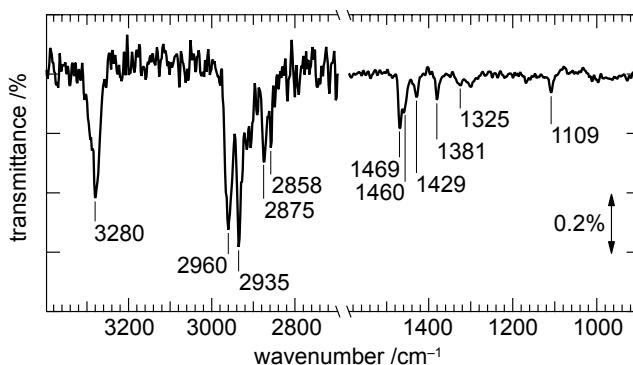


Figure 3.5: IRRA spectrum of 1.6L 1-hexyne adsorbed on Pt(111) at 100K. Adapted with permission from J. Phys. Chem.C 122, 8, 2018, 4428-4436. Copyright 2018 American Chemical Society.

Table 3.1: Vibrational band assignments for a multilayer of 1-hexyne adsorbed on Pt(111) at 100 K in comparison to Ru(0001).

1-hexyne multilayer Band assignment	on Pt(111) ($\tilde{\nu}/\text{cm}^{-1}$)	on Ru(0001) [165] ($\tilde{\nu}/\text{cm}^{-1}$)	Hexylidyne on Pt(111) [157] ($\tilde{\nu}/\text{cm}^{-1}$)	Band assignment
$\nu \equiv \text{CH}$	3280	3277		
$\nu_{as}\text{CH}_3$	2960	2959	2961	$\nu_{as}\text{CH}_3$ (gtt)
$\nu_{as}\text{CH}_2$	2935	2936	2936	$\nu_{as}\text{CH}_2$ (gtt)
$\nu_s\text{CH}_3$	2875	2872	2877	$\nu_{as}\text{CH}_3$ (ttt)
	2858		2857	$\nu_{as}\text{CH}_2$ (gtt)
$\delta_{as}\text{CH}_3$	1469	1468		
	1460		1460	$\delta_{as}\text{CH}_3$
$\delta_s\text{CH}_2$	1429	1429		
$\delta_s\text{CH}_3$	1381	1379	1381	$\delta_s\text{CH}_3$ (ttt)
ωCH_3	1325	1327		
ρCH_3	1109	1109		

3.3 Discussion

3.3.1 Dehydrogenation and Thermal Hydrogen Evolution

First we turn to the dehydrogenation and hydrogen release since thermal treatment of unsaturated hydrocarbons on clean transition metals primarily leads to formation of dehydrogenated carbonaceous deposits on the surface [29]. The TPD spectra of 1- and 3-hexyne demonstrate this, as evidenced by the release of molecular hydrogen upon heating, which can be used to identify main dehydrogenation characteristics. Figure 3.6 depicts the reaction selectivity of the TPD spectra in figure 3.1 and 3.2, with respect to the desorption of the alkyne, self-hydrogenated alkene, dehydrocyclization to benzene or the formation of coke on the basis of integrating the TPD signals.

During TPD approximately 69 and 87% of the adsorbed 3- and 1-hexyne molecules, res-

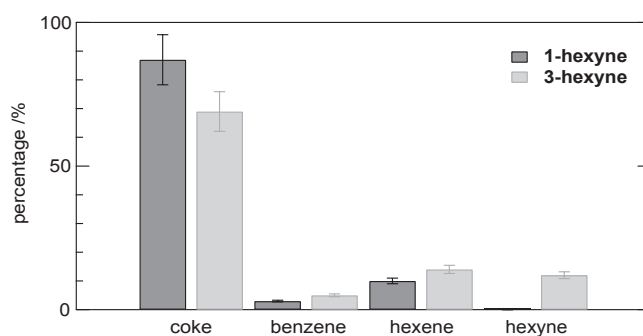


Figure 3.6: Percental product distribution of 0.11/SA 1- and 3-hexyne on clean Pt(111) during TPD. Adapted with permission from *J. Phys. Chem.C* 122, 8, 2018, 4428-4436. Copyright 2018 American Chemical Society.

pectively, decompose for the lowest coverage investigated in this work as evidenced by AES (detailed information about the Auger spectra can be found in the SI). The yield of dehydrogenated products is comparable to other alkynes such as acetylene (90 to 99% [166, 167]) and propylene (76% [168]). Similar results are found for 1-hexene (65 to 98%) and 1,5-hexadiene (100% [137, 144]) on Pt(111).

The hydrogen formation from hexynes can be divided into two regions. The high temperature region above 450K is typically associated with the final and complete dehydrogenation of residual hydrocarbons on the surface leading to $C_nH(ads)$ and graphitic carbon. The formation of these species seems to be almost independent of functional group and chain length of the initial hydrocarbon since these features have also been observed for alkenes, e.g. ethylene, propylene and 1-hexene, and alkynes such as acetylene and methylacetylene [49, 137, 168, 169]. The second region between 300 and 450K constitutes the main dehydrogenation signals of 1- and 3-hexyne as can be seen in figure 3.2. In comparison to the corresponding alkenes, the hexynes do not exhibit a low temperature desorption signal below 300K. These low temperature signals of alkenes have been ascribed to the removal of hydrogen directly located at the double bond of the hydrocarbon. In the case of terminal alkenes the initial removal of hydrogen leads to the formation of alkylidyne species at low temperatures and in the case of 1-hexene the H_2 -TPD spectra correlates with the formation of hexylidyne evidenced by IRRAS [144, 157].

The desorption of molecular hydrogen on Pt(111) is observed at 350 K below monolayer coverage and shows second order kinetics due to recombination of atomic hydrogen [170]. Only at coverages close to one monolayer a second desorption feature is observed at temperatures below 250 K, which is attributed to repulsive lateral interactions between adsorbed molecules. The hydrogen release of hexynes is characterized by higher desorption temperatures, which clearly indicates that these signals are either reaction-rate limited or surface diffusion is hindered by the presence of coadsorbed dehydrogenated hydrocarbons.

The removal of hydrogen directly attached to the functional group is effectively suppressed for hexynes at low temperature. This effect has also been observed for the dehydrogenation of ethylene compared to acetylene on Pt(111) [169]. It should be noted, that the removal of

hydrogen from a terminal alkyne, e.g. acetylene and 1-hexyne, and consequent desorption requires higher temperatures compared to alkenes. This indicates that initial bond breaking takes place at CH-bonds directly located at the alkene functional group rather than at aliphatic substituents and terminal alkynes.

Interestingly 1-hexyne shows lower hydrogen yield than 3-hexyne for low coverage, as can be seen in figure 3.1. Simultaneously the amount of carbonaceous species after TPD is substantially higher as evidenced by Auger spectroscopy. This already indicates that for 1-hexyne an additional reaction pathway has to be taken into account. One reaction pathway, which could be accessible for 1-hexyne in contrast to 3-hexyne, is the formation of a hexylidyne species at low temperatures as observed for 1-hexyne on Ru(0001) [165].

An additional argument, which supports partial hexylidyne formation besides increased carbon residuals and lower hydrogen yield, can be found in the IRRA spectrum. Two additional bands are identified in the IRRA spectrum at 2858 cm^{-1} and 1460 cm^{-1} , which are not observed for a multilayer of 1-hexyne adsorbed on Ru(0001). These vibrational modes can be attributed to $\nu_{as}\text{CH}_2$ (ggt) and $\delta_s\text{CH}_3$ (ttt) of different conformer hexylidyne species respectively, whereas the remaining vibrational modes overlap with the multilayer [157].

3.3.2 Desorption of C_6 Molecules

Two primary, non-dissociative chemisorption modes of alkynes have been identified depending on the interaction of the π orbitals with the metal surface being a di- σ /di- π complex involving four metal atoms and a di- σ/π complex involving three metal atoms [29].

The first signal observed in the MIE/UP spectra occurs at 10 eV for 3-hexyne and at 10.8 eV for 1-hexyne. These signals can be attributed to emission from π -orbitals. Emission from the highest occupied orbital of 3-hexyne is measured at 9.3 eV during UPS in the gas phase [161]. However, direct correlation between IP and adsorption mode is not straightforward, since the measured quantity might contain contributions of both, physisorption and chemisorption resulting in shifts of opposite direction [112, 116]. Surface screening typically lowers the IP of adsorbed molecules by $\approx 1\text{ eV}$ [112]. Since the difference in IP between gas phase and adsorbed on Pt(111) is found to be smaller for the π -orbital, it is likely, that this orbital takes part in a chemical bond to the surface, which would be in line with a di- σ/π adsorption. In contrast, the first peak of adsorbed 1-hexyne is observed at 11 eV at high coverages, whereas emission of the π -orbital is observed at 10 eV in the gas phase [162]. Therefore these orbitals are not chemically bonded to the surface and are characteristic of a physisorbed multilayer as evidenced by TPD. The remaining three signals, which were fitted in figure 3.3, can be assigned to σ_{CH} and σ_{CC} orbitals [162]. Several molecular orbitals with similar energies contribute to these signals, which leads to broad peaks in the spectra.

The simultaneous contribution of σ and π orbitals of alkynes when bonding on a surface lead to high adsorption energies, which are typically in the range of $\approx 2\text{ eV}$ [171]. Consequently chemisorbed alkynes tend to dehydrogenate rather than desorb. For example, almost no thermal

molecular desorption is observed during an acetylene TPD on Pt(111) [169]. For both hexynes molecular desorption on Pt(111) can be observed in a broad temperature window around 300 K, which would result in a desorption energy of ≈ 1 eV using a simple *Redhead* analysis [120]. This desorption energy is significantly lower than expected based on adsorption properties. Two reasons seem to be plausible to explain this behavior. First, the coverages investigated in this work are close or even higher than the monolayer coverage. This leads to non-negligible intermolecular interactions between adsorbed alkynes effectively weakening adsorption. Additionally geometric effects might lead to occupation of non-favorable adsorption sites, where the number of interacting metal surface atoms is not maximal. Secondly the *Redhead* approach might be inappropriate to describe the investigated system since it was shown for the desorption of n-alkanes from both, metal surfaces and metal oxides, that additional entropy effects upon desorption, e.g. rotational and translation entropy gain, have to be taken into account [172, 173]. This leads to higher kinetic prefactors by several orders of magnitude. Although the desorption of alkynes should be dominated by the functional group, the alkyl substituents could have an additional impact on the kinetic prefactor.

The desorption of hexenes produced by self-hydrogenation are mainly observed above 310 K in contrast to the desorption of the pure 1-hexene molecules on the clean Pt(111) surface below 280 K [137, 144]. Consequently the formation of self-hydrogenated species can be assigned to be rate-limited. This assumption is further supported by the hydrogen release observed for the hexynes. The main dehydrogenation pathway, which is observed above 300 K, forms atomic hydrogen on the surface, which in turn can hydrogenate alkynes. The temperature of the main dehydrogenation channel is significantly above the desorption temperature of the hexene, which also explains, why no significant amount of hexane is observed as this would entail another hydrogenation step requiring two hydrogen atoms before hexene simply desorbs. Although the percentage of the self-hydrogenated product seems to be low (see figure 3.6), the actual coverage of hexenes on the surface tends to be higher since a certain threshold of coverage has to be overcome in order to observe molecular desorption [137].

The same holds true for the desorption of benzene. Below monolayer coverage only 45 % of the adsorbed molecules desorb intact upon heating during TPD whereas 55 % dehydrogenate and dissociate at the surface according to Campbell *et al.* [174]. In other words the actual yield of formed benzene on the surface might be twice as high as actually observed during desorption in the TPD experiments. Interestingly the intramolecular dehydrocyclization of hexynes to form benzene has not been reported so far and the same reaction, which has occasionally been observed for hexenes [137, 175], is not very well understood on a mechanistic level.

In principle three reaction mechanisms can be proposed for dehydrocyclization of C_6 hydrocarbons: formation of a cyclic C_5 -membered ring followed by ring enlargement, stepwise dehydrogenation followed by ring-closure or *vice versa*. Ring enlargement of a C_5 -membered ring has been observed in small quantities during TPD of 1-methyl-1-cyclopentene and methylene cyclopentane on Pt(111) [176]. However, this mechanism would first require the formation of a C_5 -membered ring, which is reported to be stable up to 325 K [176]. This species would have

characteristic vibrational frequencies, e.g. $\delta(\text{ring})$ at 1215 cm^{-1} , and none of these frequencies have been observed for linear hydrocarbons on Pt(111) using IRRAS [157] and SFG [150, 151] making this mechanism rather unlikely.

Differentiation between the two remaining mechanisms based on TPD results alone is rather difficult. The desorption temperature of benzene produced by dehydrocyclization of either hexynes or hexenes on Pt(111) of this study is comparable to the desorption-limited TPD of pure benzene on Pt(111) at low coverage [174]. This desorption is thought to be related to a bridge site on the platinum surface [177] and the variations in desorption temperatures observed in this study might be caused by spectator species, which were also postulated to perturb adsorption sites of linear hydrocarbons on Pd(111) [175]. For the dehydrocyclization of 1-hexene on $\text{Cu}_3\text{Pt}(111)$ it was shown by NEXAFS measurements, that the rate-determining step is the formation of a cyclic intermediate, whereas dehydrogenation takes place already at low temperatures [145]. 1-Hexene is believed to dehydrogenate to form a 1,3-hexadiene via an allylic intermediate, followed by 1,3,5-hexatriene, which finally forms benzene. Due to the detection of hexenes caused by self-hydrogenation of 1- and 3-hexyne on Pt(111) at 300 K it is obvious that significant dehydrogenation takes place at temperatures below 300 K. Therefore cyclization would have to take place below that temperature for a mechanism in which cyclization precedes dehydrogenation. However no experimental evidence was found for ring-formation by IRRAS e.g. for the surface chemistry of 1-hexene on Pt(111) [157].

Consequently a mechanism based on dehydrogenation followed by cyclization seems rather likely. The presence of self-hydrogenated alkenes could be the starting point of a mechanism analogous to the dehydrocyclization of 1- and 3-hexene on $\text{Cu}_3\text{Pt}(111)$. For the alkynes, an additional mechanistic route without the formation of an alkene species could lead to the formation of an allylic intermediate, namely half-hydrogenation to a vinyl-intermediate followed by a 1,2-hydrogen shift. These isomerizations caused by hydrogen shifts have been observed for several hydrocarbons on Pt(111) including the inter-conversion between adsorbed acetylene and vinylidene [42] and η^3 -allyl to propylidyne [178]. The formation of a hexadiene species is followed by additional dehydrogenation steps leading to hexatriene, which finally forms benzene. The proposed reaction mechanism is summarized in figure 3.7.

3.4 Conclusions

The studies presented in this work shed light onto the complex surface chemistry of hexynes on Pt(111). Both molecules mainly undergo dehydrogenation to form highly dehydrogenated carbonaceous species during TPD, ranging from 70 to 90% of the initially adsorbed molecules. As a direct consequence of the functional group, the corresponding hydrogen evolution is characterized by higher desorption temperatures compared to the analogous alkenes. Three major desorbing carbon species are detected: molecular desorption of chemisorbed hexyne, hexenes produced by self-hydrogenation as well as benzene formed by dehydrocyclization. Intramolecular dehydro-cyclization of linear C_6 alkynes to form benzene takes place regardless

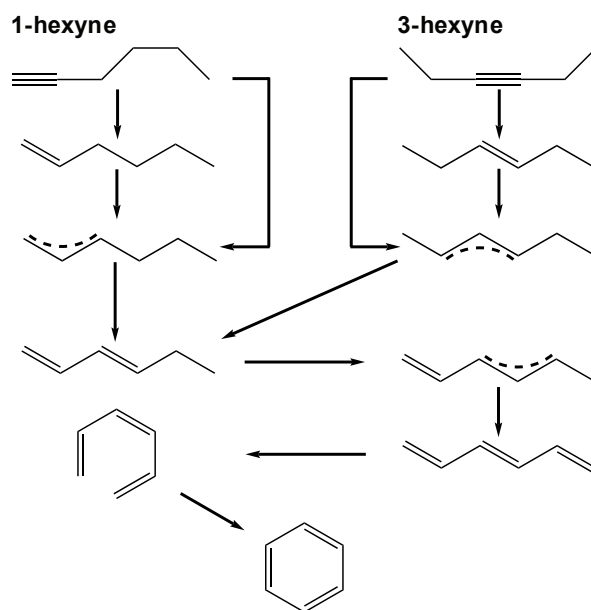


Figure 3.7: Proposed reaction mechanism for benzene formation of hexynes and hexenes on Pt(111). Dehydrogenation of an allylic intermediate, which is formed either by dehydrogenation of hexenes or by half-hydrogenation followed by 1,2-hydrogen shift of alkynes, leads to hexadiene. Further dehydrogenation leads to a hexatriene species, which cyclizes to form benzene. Adapted with permission from J. Phys. Chem.C 122, 8, 2018, 4428-4436. Copyright 2018 American Chemical Society.

of the position of the triple bond and is reported for the first time. Based on similarities between alkynes and alkenes, and similar investigated systems, a reaction mechanism based on dehydrogenation followed by ring-closure is proposed. Identification and characterization of all available reaction pathways of alkynes including the dehydrocyclization are of pivotal importance for understanding activities of metal catalysts, since the carbon residues were shown to have a major impact on catalytic activity [48, 179]. This work provides a first step and foundation for further investigations of long-chained alkynes on platinum catalysts.

3.5 Additional Insights

The preceding chapter dealt with the thermal surface chemistry of different hexynes on Pt(111) and neglected thereby compulsory the chemistry of the according hexenes. It is the aim of this section to highlight effects encountered during investigation of these molecules. The entire TPD studies of alkenes on Pt(111) are summarized in figure 3.8 and additional IRRA spectra of 3-hexenes and 3-hexyne are shown in figure 3.9.

The assignment of different m/z ratios for the TPDs displayed in figure 3.8 follows mostly the one of hexynes: 2 for hydrogen, 57 for hexane, 78 for benzene, and 69/67 for the corresponding hexene as no hexynes are present in these experiments. The dehydrogenation leading to release of molecular hydrogen and intramolecular dehydrocyclization were already discussed in the

previous chapter. The self-hydrogenation leading to hexane can be monitored by the m/z ratio of 57. For *cis*- and *trans*-3-hexene only negligible amounts of hexane can be detected. A sharp signal of hexane desorption is observed at 236 K for 1-hexene, which is in qualitative agreement with previous studies [137]. Here, the hexane desorption is coincident with the onset of hydrogen release. The appearance of hexane during TPD of 1-hexene in contrast to the 3-hexenes reflects the nucleophilic character of the atomic hydrogen during hydrogenation, which is suppressed for electron-rich 3-hexenes.

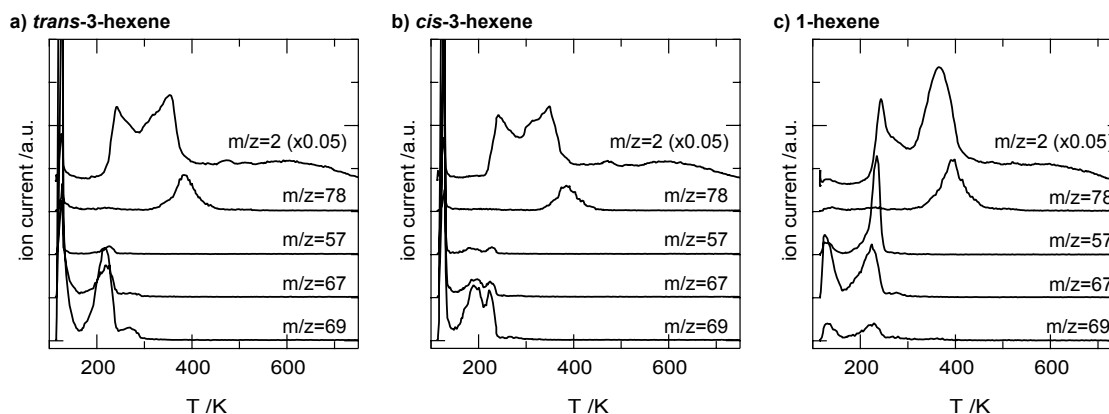


Figure 3.8: TPD studies of different hexenes on Pt(111). In each experiment, 0.22/SA of a) *trans*-3-hexene, b) *cis*-3-hexene, and c) 1-hexene was dosed at 100 K.

The molecular desorption of hexenes is more complex. Regardless of the actual surface chemistry, they all have in common, that hexene desorption takes place at temperatures significantly below 300 K in contrast to hexene desorption caused by self-hydrogenation of alkynes above 300 K. Consequently the desorption of self-hydrogenated hexenes described in the previous section can definitely be assigned to be rate-limited, which is consistent with the higher temperatures required for dehydrogenation of hexynes. In the simple case of 1-hexene, only one desorption signal at 222 K is observed. For *trans*-3-hexene, one major desorption signal is detected at 215. Interestingly, *cis*-3-hexene exhibits two distinct features at 194 and 221 K. At first glance the presence of two desorption signals might be attributed to pronounced differences in adsorption sites. However, a similar behavior has been described for the thermal chemistry of *cis*- and *trans*-2-butene on Pt(111)[180]. The *cis*-isomer desorbs at higher temperatures compared to the *trans*-isomer indicating stronger bonding to the surface, which is in this respect surprising as the *trans*-isomer is thermodynamically more stable. At the same time isomerization of *trans* to *cis* takes place at lower temperature than *vice versa*. The relative stability of the two alkenes on Pt(111) depends not only on the energies of molecular deformations and alkene-surface interactions, but also on those associated with surface restructuring[181]. It seems like this effect of surface restructuring can be expanded to internal hexenes, but more mechanistic details are required to acquire a more complete picture.

One problem, which hinders more meaningful statements about the surface stability of

hexenes, is associated with the identical cracking pattern of both molecules. This drawback can be circumvented by means of IRRA spectroscopy, which is shown in figure 3.9. The most prominent bands are summarized in table 3.2 and band assignment was performed using different references [150, 158, 182]. Comparison between the spectra of *cis*- and *trans*-isomers in figure 3.9 leads to identification of characteristic frequencies for each molecule, for instance 2843 cm^{-1} of *trans*-3-hexene. These bands could be used to detect the presence/absence of different isomers at the temperature of interest. Along with isotopic labeling of the initial molecules, a combined IRRAS and TPR study could shed light on the puzzling surface chemistry of hexenes in the future.

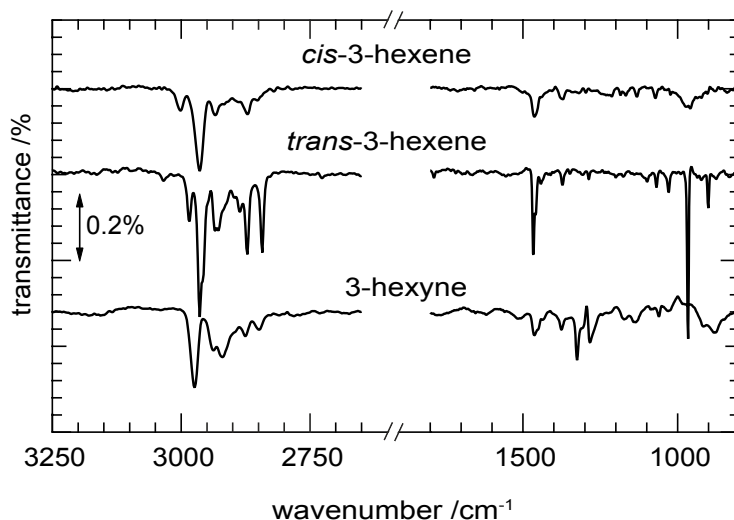


Figure 3.9: IRRA spectra of 0.44/SA 3-hexenes and 3-hexyne adsorbed on Pt(111) at 100 K.

Table 3.2: Vibrational band assignments for 3-hexenes and 3-hexyne adsorbed on Pt(111) at 100 K.

Band assignment	<i>cis</i> -3-hexene ($\tilde{\nu}/\text{cm}^{-1}$)	<i>trans</i> -3-hexene ($\tilde{\nu}/\text{cm}^{-1}$)	3-hexyne ($\tilde{\nu}/\text{cm}^{-1}$)
$\nu =\text{CH}$	3003	2983	
$\nu_{as}\text{CH}_3$	2964	2964	2974
$\nu_{as}\text{CH}_2$	2933	2933/28	2937
$\nu_{as}\text{CH}_2$			2920
$\nu_s\text{CH}_3$	2872	2872	2875
$\nu_s\text{CH}_2$		2843	2846
$\delta_{as}\text{CH}_3$	1460	1466	1463
$\delta_s\text{CH}_3$	1367	1370	1379
ωCH_3			1325

3-HEXYNE ON SIZE-SELECTED PT CLUSTERS

Size-selected metal clusters supported on metal oxides have recently gained significant scientific attention due to their potential to investigate hydrogenation reactions on a fundamental level. To expand previous studies on ethylene hydrogenation we report on the selective hydrogenation of 3-hexyne. The studies were carried out on the same model systems of Pt clusters supported on MgO as for the ethylene hydrogenation and introduce the additional parameter of reaction selectivity. Isotopically labelled temperature-programmed reaction experiments show that the surface chemistry of 3-hexyne is dependent on cluster size and characterized by desorption of several reaction products. The latter include formation of molecules involving dehydrogenation as well as hydrogenation steps. By comparison between hydrogenation of hexyne and ethylene an atomic window is found for Pt₉, where activation barriers favor effectively triple over double bond hydrogenation leading to enhanced selectivity. The favored hydrogenation of the triple bond is found not to be correlated to hydrogen dissociation, but rather to cluster morphology and adsorption sites available for the alkyne. This is the first experimental evidence of the potential use of supported, size-selected metal clusters for selective hydrogenation reactions.

4.1 Introduction

Cluster-based materials with control over atomic size have been intensively studied under ultra-high vacuum (UHV) conditions due to their unique and unpredictable catalytic properties evolving by addition of single atoms [80, 183, 184]. Typically, these investigations dealt either with CO oxidation or acetylene cyclotrimerization catalyzed by late transition metals, in particular Au, Pd and Pt, supported on various metal oxides including MgO [87, 124, 185, 186], SiO₂/Si [70, 187, 188], Al₂O₃ [189, 190] and TiO₂ [191–197].

In recent years the focus of cluster research has shifted towards (de)-hydrogenation reac-

tions of unsaturated hydrocarbons [34, 46, 89, 198, 199]. Our group has shown that supported Pt clusters in the size regime of seven to twenty atoms show distinguishable catalytic activity as a function of size for ethylene hydrogenation [34]. For instance, Pt₁₃ supported on MgO(100) shows higher hydrogenation activity stemming from increased intrinsic resistance towards undesired dehydrogenation channels, leading to poisoning of the metal surface. This finding for cluster-based materials results in structure sensitivity, which is not observed for larger nanoparticles and bulk materials [200]. The proclivity of monodisperse clusters for (de)-hydrogenation reactions was shown to be affected by local electron densities, defining unique catalytic active sites. The local electron density was shown to be not only controlled by cluster size [34, 46], but also by support material [83] and stoichiometry [82], offering additional possibilities to steer chemical reactivity.

Having established an advanced understanding of ethylene hydrogenation on supported Pt clusters on both, an experimental and theoretical basis, the question arises whether these gained insights can be expanded to more complex systems involving other functional groups and alkyl-substituents. Particularly the replacement of the double bond by a triple bond introduces the supplemental parameter of selectivity in addition to overall hydrogenation activity. In order to gain insights into these systems, the hydrogenation of 3-hexyne has been chosen as a model system for long-chained alkynes, keeping cluster component (Pt_n, n between 3 and 13) and MgO(100) as support material constant. This approach allows direct comparison between an unstudied reaction and well-characterized catalyst systems. The tendency to form different reaction products defining cluster selectivity has been tested by isotopically labelled temperature-programmed reaction (TPR) experiments and are compared to results of a Pt(111) single crystal.

4.2 Results

TPR spectra of 3-hexyne and deuterium on supported, size-selected Pt_n clusters, bare MgO(100) and Pt(111) are shown in figure 4.1 and 4.2. Figure 4.1 is devoted to hydrogenation products by coadsorbed D₂, whereas figure 4.2 contains species involving either direct or indirect dehydrogenation steps.

The two possible reaction products of 3-hexyne and deuterium are deuterated hexene and hexane, which can be distinguished using their molecular mass as shown in figure 4.1. No molecular desorption of d₂-hexene at $m/z = 86$ is observed for cluster sizes containing between three and seven atoms as well as the bare MgO(100) support within the sensitivity of the experiment. A small onset of hexene desorption is detected for Pt₈ around 150 to 300 K. Significant hexene desorption are found for Pt_{9,10} and Pt₁₃ having broad desorption features and maxima around 250 K. For Pt(111), two major desorption signals around 150 and 250 K can be seen in figure 4.1. No molecular desorption of d₄-hexane at $m/z = 90$ is detected for all cluster sizes and only minor desorption at 184 K for the platinum single crystal.

Besides the formation of deuterated products, additional reaction pathways including de-

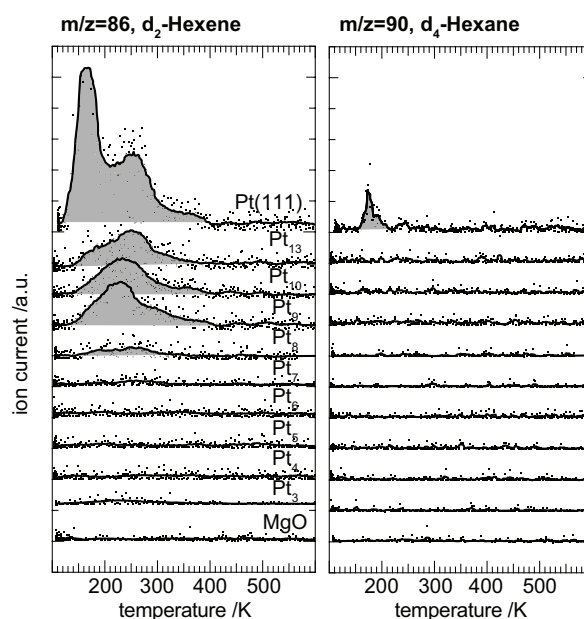


Figure 4.1: TPR results of 3-hexyne and D_2 on size-selected Pt clusters supported on MgO(100) tracing $m/z = 86$ (deuterated hexene, a) and $m/z = 90$ (deuterated hexane, b). Desorption signals are highlighted by grey background. The results obtained for the bare MgO(100) support and a Pt(111) single crystal are shown for comparison.

hydrogenation steps have to be taken into account for the surface chemistry of 3-hexyne as shown in figure 4.2. The m/z ratio of 69 was used to determine the amount of self-hydrogenation leading to the formation of H_2 -hexene. In contrast to deuteration, the hydrogen atoms stem from dehydrogenation of 3-hexyne making atomic hydrogen available for intermolecular hydrogenation of 3-hexyne. No self-hydrogenation is observed for cluster sizes below eight atoms. The signal below 200 K is caused by physisorbed 3-hexyne and can be neglected. Cluster sizes between 8 and 13 atoms show broad signals ranging from 200 up to 400 K, and hexene desorption occurs additionally below 200 K on Pt(111). At temperatures above 400 K, benzene desorption is observed for all cluster sizes and Pt(111).

Integration and normalization of the TPR curves to the number of Pt atoms per sample are shown in figure 4.3. Four desorbing species have been identified including (self-) hydrogenated hexene, hexane and benzene. The only observable reaction pathway of 3-hexyne and deuterium on Pt clusters containing between 3 and 7 atoms is the formation of benzene. Pt_8 is the minimum cluster size where hexene desorption occurs in both forms, hydrogenation and self-hydrogenation. Larger cluster sizes (9, 10 and 13) show higher activity than the Pt(111) surface for all products.

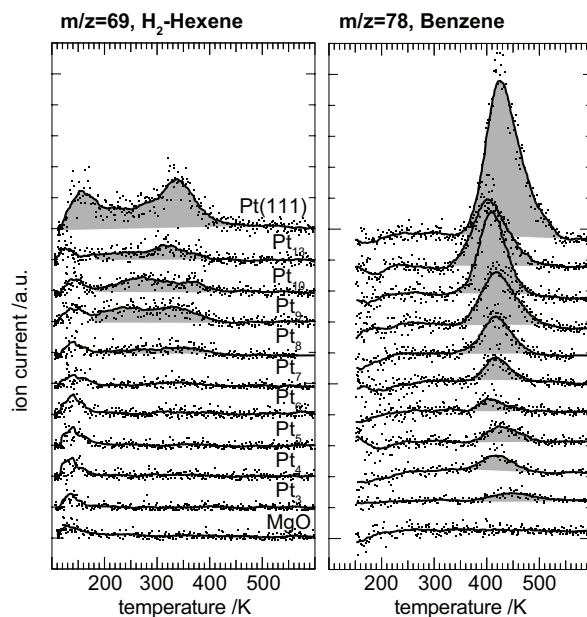


Figure 4.2: TPR results of 3-hexyne and D_2 on size-selected Pt clusters and Pt(111) showing $m/z = 69$ (H_2 -hexene, a) and $m/z = 78$ (benzene formation, b). Desorption signals of H_2 -hexene (grey) are caused by self-hydrogenation and the feature below 160 K originates from the cracking pattern of 3-hexyne physisorbed on the support. The desorption of benzene occurs above 400 K for all cluster sizes.

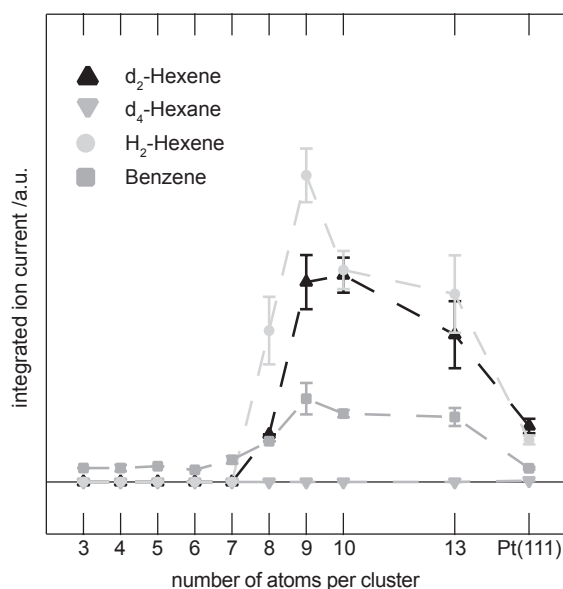


Figure 4.3: The integrated signals from the TPR curves in figure 4.1 and 4.2 normalized to the number of Pt atoms are displayed as a function of cluster size.

4.3 Discussion

The discussion is divided into two parts. First, reactions which do not necessarily require the presence of deuterium are dealt with including formation of H₂-hexene and benzene. In the second part, reactions of 3-hexyne explicitly including deuterium and their impact on selective hydrogenation reactions are discussed.

4.3.1 Dehydrogenation Pathways

The thermal chemistry of unsaturated hydrocarbons on clean transition metals under UHV conditions is known to be characterized by dehydrogenation, leading to the formation of strongly adsorbed carbonaceous species on the metal surface [29]. This process releases atomic hydrogen, which in turn can either recombine to form molecular hydrogen or hydrogenate additional molecules on the surface. The intermolecular hydrogenation was monitored in this work by desorption of H₂-hexene. As expected, no production of H₂-hexene was observed for the blank MgO(100) support, but also platinum metal clusters up to seven atoms showed no significant intermolecular hydrogenation. This observation can be rationalized by the number of adsorption sites available under the applied reaction conditions. Smaller clusters exhibit presumably only one adsorption site of 3-hexyne effectively suppressing intermolecular interactions between adsorbed hexynes. This can be illustrated on Pt₃ clusters, which are assumed to have a trigonal planar structure on the surface. Alkynes adsorb in a di- σ/π configuration on platinum [201], which requires three surface atoms, and consequently all cluster atoms are in direct contact with one single hexyne molecule and not available for interactions with additional molecules. For larger clusters, e.g. Pt₇, additional effects have to be taken into account. The alkyl-substituents of 3-hexyne might sterically hinder co-adsorption or even weaken co-adsorption due to intermolecular interactions, which in turn lead to desorption before dehydrogenation. Besides these interactions, the transition between Pt₇ and Pt₈ might be accompanied by significant changes in cluster morphology, which was proposed between these sizes on TiO₂(110) [192, 194].

As soon as the cluster reaches a critical size, co-adsorption and self-hydrogenation takes place. The broad desorption feature, exhibiting at least two maxima for Pt₉ and Pt₁₀, reflects the multi-step nature of the dehydrogenation. First, significant dehydrogenation takes place below room temperature leading to hexene desorption below 300 K for larger clusters and the metal surface. The desorption temperature of 1-hexene on Pt(111) is found between 275 to 284 K depending on coverage [137, 144], which may be indicative of repulsive interactions between co-adsorbed species of hexene and hexyne tested here. The occurrence of hexene desorption above room temperature is clearly reaction-rate limited by hydrogen release during dehydrogenation.

One reaction pathway of exclusive dehydrogenation is the formation of benzene shown in figure 4.2 b). Benzene desorption is observed even for cluster sizes below seven atoms. This reaction occurs via intra-molecular dehydrocyclization, since no evidence for CC-bond scission was found for both, cluster samples and single crystal. Our previous work has studied the thermal chemistry of 3- and 1-hexyne on Pt(111) in detail [202], concluding that cyclization follows several

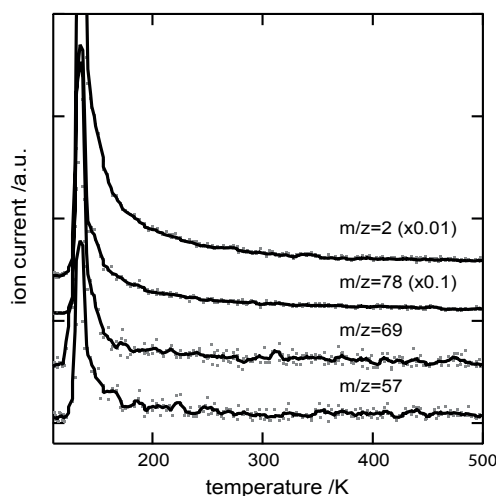


Figure 4.4: TPD of 0.44/SA 3-hexyne on single Pt atoms supported on MgO(100) (coverage of Pt atoms 4.0 % ML).

dehydrogenation steps for both molecules similar to a copper platinum alloy [146]. Furthermore, this dehydrocyclization is also available for the according hexenes regardless of the initial stereochemistry. The dehydrogenation mechanism followed by ring-closure seems to be applicable to platinum clusters, since dehydrogenation, as observed by H₂-hexene desorption in figure 4.2, has vanished below 400 K, which is significantly lower than benzene desorption. This desorption of benzene was shown to emerge only at higher coverages for Pt(111), whereas low coverages lead to complete coking of the surface without molecular desorption [174]. Consequently, the amount of formed benzene in figure 4.3 could be underestimated due to limited desorption. Three metal atoms within one cluster are sufficient for dehydrocyclization, which is explained by the adsorption mode as described above. Further evidence for this adsorption induced reaction behavior arises from dehydrogenation experiments of 3-hexyne on single Pt atoms, shown in figure 4.4. Here, the signals below 200 K are caused by the cracking contribution of 3-hexyne physisorbed on the inert support. No signals are observed for dehydrogenation ($m/z = 2$), self-hydrogenation ($m/z = 69, 57$), and dehydrocyclization ($m/z = 78$). It should be noted, that benzene formation from 3-hexyne reported in this work has distinct differences to the well-established cyclotrimerization of acetylene on Pd clusters, since the latter requires coadsorption of three molecules and represents an intermolecular reaction.

4.3.2 Hydrogenation Pathways

Figure 4.1 demonstrates, that d₄-hexane is only observed as a reaction product from Pt(111) in a small peak at 190 K. This desorption temperature is slightly lower than observed for hexane in submonolayer quantities on clean Pt(111)[173], indicating repulsive intermolecular interactions. No hexane desorption is detected for all cluster sizes, which might be explained

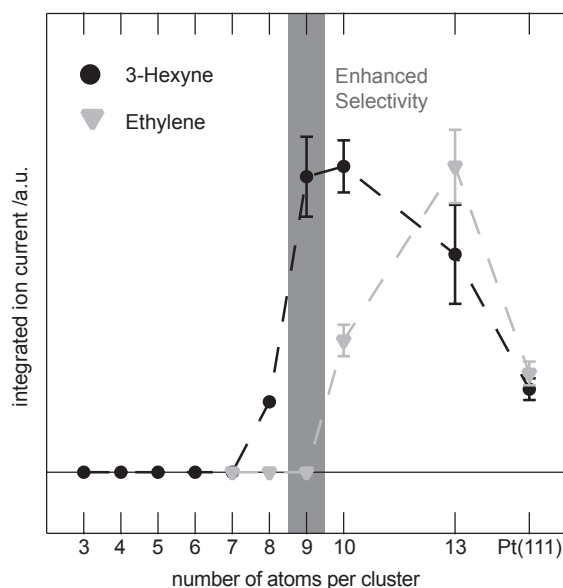


Figure 4.5: Comparison between TPR results obtained for 3-hexyne hydrogenation in this work and ethylene hydrogenation taken from reference[34]. Clusters containing less than eight atoms show no hydrogenation products for 3-hexyne indicative of unfavorable hydrogenation reaction barriers, whereas Pt_{10} and Pt_{13} clusters show reactivity towards both reactions. Only Pt_9 exhibits high activity towards a triple bond and low activity for a double bond resulting in increased selectivity.

either by intrinsic high selectivity or quantities below the detection limit. In order to gain insight into cluster selectivity, it is convenient at this point to compare formation of d_2 -hexene representative of triple bond hydrogenation to the one of a double bond, tested by ethylene hydrogenation under the same experimental conditions.

This comparison between different unsaturated functional groups for identical cluster sizes is shown in figure 4.5. As determined by integration and normalization of the ion current in figure 4.1, cluster sizes below eight atoms show no significant hydrogenation of 3-hexyne, whereas an on-off effect is observed between Pt_9 and Pt_{10} for ethane formation [34]. It should be noted, that the absence of hydrogenation products in TPR experiments does not exclude the clusters capability for hydrogenation under steady-state conditions, but general consistency is found between TPR and pulsed, isothermal experiments [46]. For cluster sizes without hydrogenation products in TPR experiments, the turn-over frequencies determined under isothermal conditions typically do not exceed the one determined for the extended surface.

Cluster sizes with increased hydrogenation activity (Pt_9 , Pt_{10} and Pt_{13}) compared to the extended surface in figure 4.5 all show similar desorption temperatures below 300 K in figure 4.1. This leads to the conclusion that activation barriers for hydrogenation as well as mechanistic pathway leading to hydrogenation are quite similar for these cluster sizes. In contrast to the platinum clusters, two distinct signals are observed for the single crystal. We tentatively attribute the low temperature signal at 180 K to hydrogenation of a weakly bound, physisorbed

hexyne molecule, whereas the high temperature signals originates from hydrogenation of hexyne chemisorbed on the metal surface. The interaction between metal and weakly bound species is decreased by preadsorbed hydrogen acting as an isolation layer, an effect which has also been observed for 1,3-butadiene adsorbed on hydrogen covered Pt(111) [203]. Given similar activation energies, but different activities and selectivities, the question arises of the origin of the latter.

A requirement for increased activity might stem from either more favorable hydrogen or alkyne adsorption. In order to test hydrogen adsorption, we have performed HD scrambling experiments on the clean cluster sizes showing increased reactivity towards hexyne. Here, Pt₉ showed limited activity towards HD-exchange in comparison to Pt₁₀ and Pt₁₃ [34, 46]. Assuming a three-dimensional prismatic structure for Pt₉ (lowest-energy structure found by first-principles calculations), the limited adsorption and dissociation of hydrogen measured by TPR experiments are caused by different interactions between hydrogen and Pt atoms of the bottom layer and top layer, respectively. Hydrogen dissociatively adsorbs on Pt atoms of the bottom layer in contrast to the top layer. However, co-adsorption of deuterium and 3-hexyne on Pt₉ investigated in this work here, demonstrates that Pt₉ is among the most active cluster sizes available for hexyne hydrogenation. Consequently the clusters capability to adsorb and dissociate hydrogen as part of the reaction network can be ruled out to be a limiting factor for both, activity and selectivity. On the contrary, co-adsorption of 3-hexyne on the D₂ precovered Pt₉ clusters has to facilitate hydrogen activation by a synergistic effect in order to achieve high hydrogenation activity as evidenced by the experiments of this work.

This adsorbate-adsorbate interaction is decisively controlled by the adsorption mode and number of available sites of 3-hexyne on the metal clusters. However, these parameters are influenced by several factors making direct correlation rather difficult. First, it was shown for the activation of ethylene, that the arrangement and in particular the local electron density of single metal atoms within the cluster define unique adsorption sites, leading to distinguishable activities [34]. The local electron density governed by cluster morphology can not be regarded as a constant, but rather changes over the course of the experiment due to fluxionality [85, 204]. This cluster relaxation is here mainly controlled by temperature and adsorption of 3-hexyne. During TPR experiments inter-isomer structural conversion occurs with more isomers being thermally accessible at higher temperatures. At the same time, the adsorption energy of an alkyne is higher than the one found for alkenes and is typically around ≈ 2 eV [171], which is comparable to the metal binding energies within the cluster [205]. Therefore adsorption of 3-hexyne is expected to have a major influence on cluster morphology by reaction-induced fluxionality. These interactions also include the activation of co-adsorbed deuterium, which is not observed for Pt₉ clusters without adsorbed alkynes. A complex interplay between these factors leads to favorable hydrogenation conditions of 3-hexyne on Pt₉, Pt₁₀ and Pt₁₃, whereas only for Pt₉ high selectivity can be achieved by suppressed alkene hydrogenation.

4.4 Conclusions

In this chapter the surface chemistry of 3-hexyne was addressed on size-selected Pt clusters supported on MgO(100). The selectivity for different reaction channels was tested by isotopically labelled TPR experiments with the conclusions that (i) all cluster sizes between 3 and 13 atoms showed intramolecular dehydrocyclization of 3-hexyne to form benzene comparable to the Pt(111) single crystal. This finding is correlated to the di- σ/π adsorption mode only requiring the presence of three metal atoms. (ii) Co-adsorption of several 3-hexyne molecules is hindered for cluster sizes smaller than 7 atoms as evidenced by desorption of H₂-hexene. This stems from intermolecular, repulsive interactions caused by steric hindrance. (iii) Small cluster sizes show no hydrogenation products, whereas Pt₉, Pt₁₀ and Pt₁₃ are more reactive than the single crystal on a per atom basis. By comparison to ethylene hydrogenation, a small atomic window is found for Pt₉, which shows high triple bond, but low double bond hydrogenation activity. The resulting enhanced selectivity can be attributed to a change of cluster morphology induced by the higher alkyne adsorption energy in comparison to ethylene. This fluxionality of the clusters is also responsible for activation of hydrogen required for increased hydrogenation activity.

The results presented here demonstrate the potential usage of cluster-based materials for selective hydrogenation reactions, but also the difficulties encountered when designing a catalyst on an atom basis. Not only changes as a function of size are observed, but the investigations of more complex molecules are also complicated by additional reaction pathways, which become accessible as the size is changed. Identification and understanding these pathways constitute a major challenge in the tuning of catalytic selectivity. This work provides the foundation for further investigations of selective hydrogenation reactions of unsaturated hydrocarbons on atomically controlled catalysts.

ETHYLENE HYDROGENATION ON SIZE-SELECTED PT CLUSTERS

5.1 Introduction

Today catalysis is one of the key technologies for establishing a sustainable society. For this aim, the reproducible fabrication of catalytic materials on a large scale is crucial, but remains one of the major challenges in industrial catalysis. Predicting metal-support interactions is crucial for controlling catalytic performance. In this context, the charge transfer caused by dopants of the support material is particularly important in the case of sub-nm sized particles, but has been widely neglected. Although several approaches have been developed to describe general metal-support interactions, there is no underlying physical principle that can predict the charge transfer between the support and the catalytic particle.

Here it is demonstrated experimentally and theoretically that doping of the support material can be used to steer catalytic activity and selectivity of size-selected platinum clusters by manipulation of the local e^- -density. Although it is generally believed that chemical bonds formed at the interface between support and metal particle determine the physical environment responsible for general support effects, it is shown that an additional physical quantity, namely the local work function of the support, is responsible for (de)-charging of metal particles. To quantify this effect the doped support was modelled material by thin α -SiO₂ films on Pt(111) and Mo(211) single crystalline surfaces with well-defined work functions and the selectivity of the ethylene hydrogenation was investigated on supported, sub-nm sized Pt clusters. Manipulation of the local work function not only opens up the possibility to steer chemical activity, but also inhibits undesired coke formation on the active metal component.

5.2 Results and Discussion

The hydrogenation of ethylene catalyzed by metals has long been a benchmark reaction for more complex systems of unsaturated hydrocarbons. Although the reaction follows the Horiuti-Polanyi mechanism[14], it was soon recognized that there is a complex interplay between hydrogenation and dehydrogenation of the hydrocarbon on the metal surface. In general, a large distance between the d-band center and E_F (Fermi energy) is favorable for hydrogenation activity whereas decreasing distance between d-band center and E_F leads to dehydrogenation and formation of carbonaceous species on the surface, e.g. ethylidyne. For platinum based catalysts, these dehydrogenated deposits were made responsible to mask any effect of the underlying metal on hydrogenation activity and consequently this reaction was believed to be structure-insensitive.

Recent research has demonstrated that platinum clusters (Pt_{8-15}) supported on MgO(100) show structure-sensitive behavior for this reaction as a function of the precise number of atoms[34, 46]. Clusters in this non-scalable size regime have been recognized to possess unique physical and chemical properties [80, 183, 195, 206–208] and the local e^- -density on single atoms of nano-sized platinum instead of the d-band center can effectively suppress the formation of ethylidyne leading to enhanced activity. This local charging of single atoms within Pt_{13} clusters on α -SiO₂/Pt(111) can for instance be controlled by varying the support stoichiometry, leading to an enhanced/decreased number of Pt-O/Si bonds [82]. Changing the support material from MgO(100) to α -SiO₂/Pt(111) for several cluster sizes demonstrated the complex interplay between cluster size and support material, where acid-base arguments typically applied to heterogeneous catalysts fail to predict catalytic activity [83]. This example shows that more fundamental insights are required to develop a deeper understanding of metal-support interactions.

To this end, two model support materials have been synthesized: α -SiO₂ supported either on a Pt(111) or a Mo(211) single crystal. Hereby, the fabrication of a thin α -SiO₂ overlayer on Mo(211) (further denoted as α -SiO₂/Mo(211)) followed a modified route of Goodman and co-workers [127], whereas the system α -SiO₂/Pt(111) was characterized in detail in our own publication [126]. Besides experimental characterization (including photo-electron emission spectroscopies, infrared reflection absorption spectroscopy and temperature-programmed desorption), the model systems have been theoretically calculated as summarized in figure 5.1. The IRRA spectra exhibit vibrational bands at 1238 and 1252 cm⁻¹ and a broad shoulder down to 1100 cm⁻¹ associated with asymmetric longitudinal phonon vibrations showing the amorphous character of the films (figure 5.1 a)). Additionally, the α -SiO₂/Mo(211) exhibits a band at 1051 cm⁻¹ caused by Mo-O-Si vibrations, which in turn means, that in contrast to the platinum system, a chemical bond is formed between oxygen and the underlying molybdenum. As determined by Auger electron emission spectroscopy, both films consist of SiO₂ only (no other oxidation state than (IV) is found for silicon). An average thickness of approximately 8 ± 4 Å has been determined by AES, whereas the large uncertainty is caused by the amorphous

character of the films and the unknown mean free path of the photoelectrons. The detection of the Mo-Si-O vibration indicates that this thickness is an upper limit. The small thickness is further demonstrated by photoelectron emission just below E_F in the UP spectra shown in figure 5.1 b), which is caused by the underlying metal d-band. Absence of photoelectrons just below E_F during metastable impact emission spectra (MIES) confirmed that no defect sites contributed to the UP spectra.

In order to calculate the model systems, slabs of Pt and Mo were prepared, exposing the Pt(111) and Mo(211) surfaces. Each of these slabs contained three layers in the normal to the surface (z) directions. The size of the slabs was repeated periodically in the (x, y) directions. The bottom layer of the slab was held fixed and the slabs were relaxed to minimize the total energy using density functional calculations (references to VASP). Subsequently amorphous silica films (a-SiO₂) were prepared using the procedure described by us in detail in our previous publication [82]. A thicker ("4-layer", $4L$, about 10 Å thick) and a thinner ("2-layer", $2L$, about 5 Å thick) film have been prepared; in the following mainly the $2L$ is investigated. Views of the a-SiO₂/Mo(211) and the a-SiO₂/Pt(111) films are shown in figure 5.1 c) (silicon atoms light grey, oxygen in dark grey). Histograms of the distances $d(\text{O-Mo})$ ($d(\text{O-Pt})$) between the oxygen atoms of the Mo (Pt) atoms in the top layer of the Mo(211) (Pt(111)) substrates and the a-SiO₂ films grown on them are shown in figure 5.1 d). A significantly larger number of Mo-O bonds than Pt-O ones is observed, with the a-SiO₂ in closer contact with the Mo(211) surface. This finding is in agreement with the experimental finding, and it affects in an important manner the work function of the a-SiO₂/Mo(211) system.

The work function of the bare Mo(211) and Pt(111) surfaces and those with the a-SiO₂ films grown on them have been calculated as the difference between the effective local calculations (including electrostatic, Hartree, and exchange correlation contributions) and the Fermi energy (E_F) of the system, see figure 5.2. For both cases $\Phi(z)$ was calculated

$$\Phi(z) = \langle \Phi(x, y, z) \rangle = \langle V_{eff}(x, y, z) \rangle - E_F \quad (5.1)$$

where $\langle .. \rangle$ denotes an average over the xy plane, and z in normal to the surface plane. In figure 5.2 the variation of the above quantity starting from the position (taken as $z = 0$) of the top layer atoms of the metal substrate is shown. $\langle \Phi(z) \rangle$ converges at some distance above the surface to a constant, which is taken as the value of the vacuum level z_v . The value at z_v is designated as the global work function $\Phi = \langle \Phi(z_v) \rangle = \langle V_{eff}(z_v) \rangle - E_F$. The work function for the bare Mo surface is smaller than that of the Pt(111), and both increase when an a-SiO₂ is adsorbed on them, with the a-SiO₂/Mo(211) being less by about 2 eV compared to the platinum system.

So far, the calculations are in accordance with previous studies on the 'SiO₂/metal (regarded as a dielectricum' system [209, 210]. The dominating charge transfer of these systems can be divided into two categories: the first being the spatial penetration of the metal wave functions into the oxide creating new, metal-induced gap-states (MIGS) at the interface, the second being

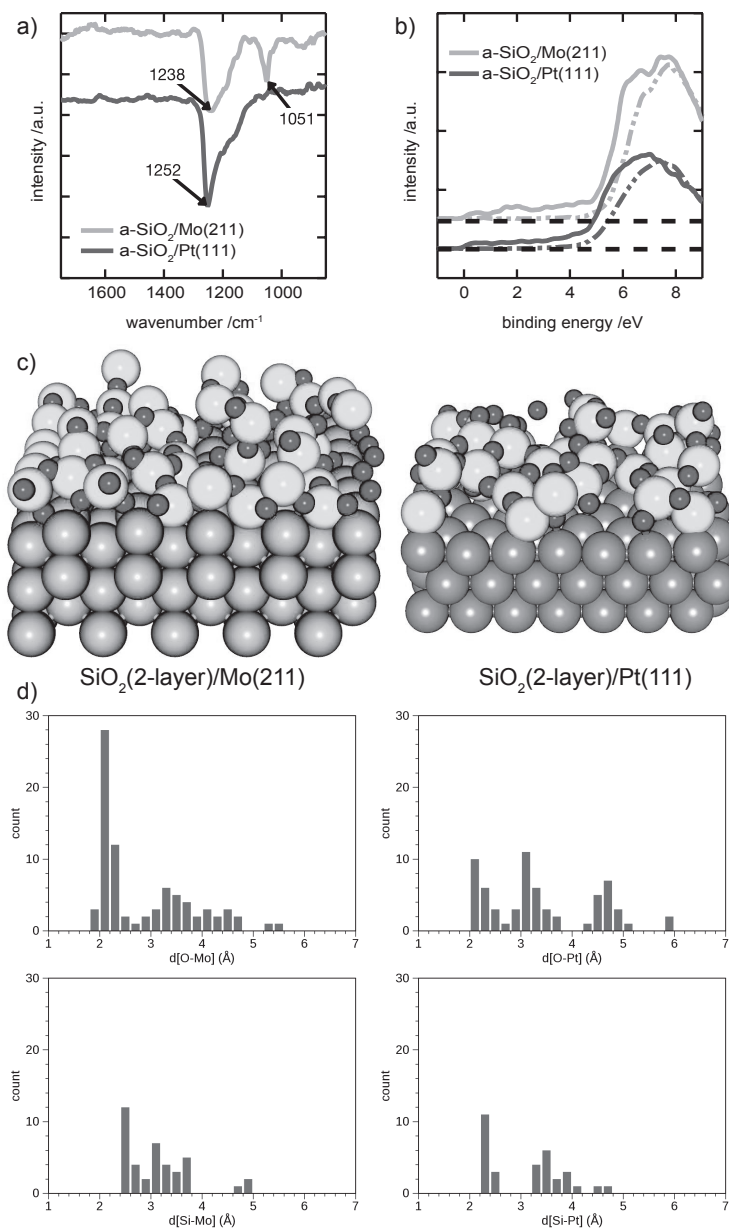


Figure 5.1: Experimental and theoretical characterization of the two support systems: $a\text{-SiO}_2$ synthesized on Pt(111) and Mo(211). a) IRRA spectra after synthesis of the support materials. The 3-D, amorphous character of both films is shown by vibrational bands at 1238 and 1252 cm^{-1} , respectively exhibiting a broad shoulder down to 1100 cm^{-1} associated with asymmetric longitudinal phonon vibrations. Additionally the $\text{SiO}_2/\text{Mo}(211)$ exhibits a band at 1051 cm^{-1} caused by Mo-O-Si vibrations. b) UP/MIE spectra (solid/dotted) of both thin films. c) Views of the calculated support systems including the underlying metal, silicon (light grey) and oxygen (dark grey). d) Histograms of the distances $d(\text{O}-\text{Mo})$ ($d(\text{O}-\text{Pt})$) between oxygen atoms in the top layer of the Mo(211) (Pt(111)) substrates and the $a\text{-SiO}_2$ films grown on them. The number of Mo-O bonds is significantly larger than the number of Pt-O bonds, with the $a\text{-SiO}_2$ in closer contact with the Mo(211) surface.

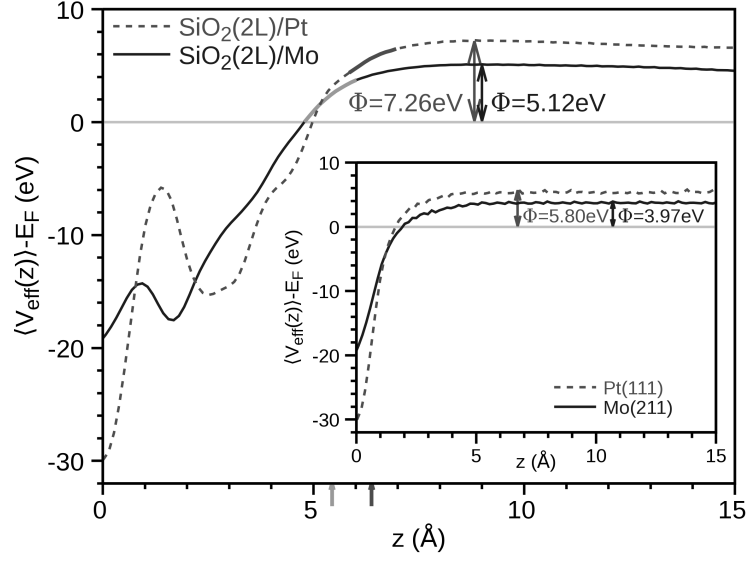


Figure 5.2: The calculated work function of the grown α - SiO_2 films on Pt(111) and Mo(211). The work function is determined by the difference between the effective local calculations and the Fermi energy (E_F) of the system. The work function converges to a constant, which is taken as the value of the vacuum level, z_v , and the correlating global work function Φ . The work function for the bare Mo surface is smaller than that of the Pt(111), and both increase when an α - SiO_2 is adsorbed on them, whereas the global work function of α - $\text{SiO}_2/\text{Mo}(211)$ is still smaller by about 2 eV compared to the platinum system.

charge transfer by covalent bonds creating covalent metal-induced gap states (CMIGS). The α - $\text{SiO}_2/\text{Pt}(111)$ system ($\Phi(\alpha\text{-SiO}_2(2\text{L})/\text{Pt}(111)) = 7.26$ eV) appears to be controlled by the first category of charge transfer, since there is no experimental evidence of interfacial Pt-O covalent bonds being formed. On the other hand, the α - $\text{SiO}_2/\text{Mo}(211)$ system ($\Phi(\alpha\text{-SiO}_2(2\text{L})/\text{Mo}(211)) = 5.12$ eV) is influenced by charge transfer through covalent Mo-O bonds (see figure 5.1). Because of the low work function of Mo, the newly created interfacial states are acceptor-like, bringing about an increased electron density in the α - SiO_2 film. The interfacial perturbation caused by covalent Mo-O bonding (see figure 5.2) is expected to have a greater effect in the case of thin silica films (e.g. 2-layer α - SiO_2) than is the case of thicker films, where the interfacial perturbation may get 'diluted' by regions of the film located further away from the metal/oxide interface.

To relate the charging propensity of a metal cluster adsorbed on the metal-adsorbed α - SiO_2 film, the local work function has to be considered, which is calculated according to:

$$\Phi_{loc}(x_i, y_i, z_i) = V_{eff}(x_i, y_i, z_i) - E_F \quad (5.2)$$

where (x_i, y_i, z_i) are the coordinates of the i -th Pt atom of the supported Pt_{13} cluster in direct contact with the underlying α - SiO_2 surface; these atoms are taken as the 7 atoms of the cluster lying closest to any of the Si or O atoms of the oxide film, with the geometry of the

a-SiO₂/metal surface taken as the one following total structural relaxation of the adsorption system Pt₁₃/a-SiO₂/metal (metal= Pt(111), Mo(112)). Pt₁₃ clusters are chosen for calculations, because they represent one of the most investigated cluster sizes [82]. The local work function of the supported Pt₁₃ cluster is determined as the average over the interfacial atoms ($\langle \dots \rangle_i$)

$$\langle \Phi_{loc} \rangle = \langle \Phi_{loc}(x_i, y_i, z_i) \rangle_i - E_F = \langle V_{eff}(x_i, y_i, z_i) \rangle_i - E_F \quad (5.3)$$

In order to sample the heterogeneous environment of the a-SiO₂ film surface, the surface is divided into a grid containing ZZZ points, and the Pt₁₃ is positioned at each of these points, followed by subsequent total relaxation of the adsorption system, and evaluation of the local work function for that cluster (as described above). The range of average distances $\langle (x_i, y_i, z_i) \rangle_i$ for the ensemble of sampled adsorbed cluster configurations and the corresponding range of $\langle \Phi_{loc} \rangle$ values are indicated in figure 5.2 by changed colored segments, with the corresponding arrows on the horizontal (z) axis, indicating the corresponding mean of the distribution of the distances of the bottom layer of the adsorbed Pt₁₃ clusters from the topmost atoms of the Mo(211) (Pt(111)) metal substrates.

In figure 5.3 the values obtained for $\langle \Phi_{loc} \rangle$ versus several characteristics of the system are displayed: a) the excess (depletion) of the number of electrons on the particular sampled cluster configuration, $\Delta n_e(\text{Pt}_{13})$ (determined through Bader analysis), b), c) the number $n(\text{Pt-Si})$ and $n(\text{Pt-O})$ of average bonds formed between the interfacial atoms of each of the sampled Pt₁₃ cluster configurations with the a-SiO₂ surface. Additionally, $\Delta n_e(\text{Pt}_{13})$ plotted versus $n(\text{Pt-Si})$ and $n(\text{Pt-O})$ for each of the sampled Pt₁₃ clusters is displayed in d), e). From figure 5.3 a), a clear correlation is observed between the values of $\langle \Phi_{loc} \rangle$ and $\Delta n_e(\text{Pt}_{13})$, with the Pt₁₃ clusters adsorbed on the Pt(111) supported a-SiO₂ film, having a higher local work function and being positively charged (that is $\Delta n_e(\text{Pt}_{13}) < 0$), whereas, the clusters adsorbed on the Mo(211)-supported film being characterized by lower values of $\langle \Phi_{loc} \rangle$ that correlate with excess electrons ($\Delta n_e(\text{Pt}_{13}) > 0$) corresponding to negative charging of the clusters. The results in figure 5.3 b), c) show that the high local work function of a-SiO₂/Pt(111) system correlates with a low number of Si-Pt bonds and a high number of O-Pt bonds between the atoms of the a-SiO₂ film and the bottom atoms of the sampled adsorbed Pt₁₃ clusters. The reverse correlation is found for the a-SiO₂/Mo(211) system, with the smaller values of $n(\text{O-Pt})$ reflecting the oxygen depletion of the top of the a-SiO₂ film because of the aforementioned formation of Mo-O bonds at the interface with the supporting metal, which draws oxygen atoms to the deeper interfacial region and away from the top region of the film.

To evaluate the charging properties in dependence of the support system, low coverages of size-selected Pt_n clusters ($4.5 \cdot 10^{12}$ particles per sample, 0.785 cm^2) were deposited on the support systems under soft-landing conditions ($E_{Kin} < 1 \text{ eV/atom}$). The Pt_n (n=10, 13 and 14) clusters are tested for their catalytic activity and deactivation during ethylene hydrogenation using a pulsed molecular beam reactive scattering experiment (p-MBRS). The temperature of the sample is kept at 300 K and a background pressure of $2 \cdot 10^{-6}$ mbar D₂ is applied in the

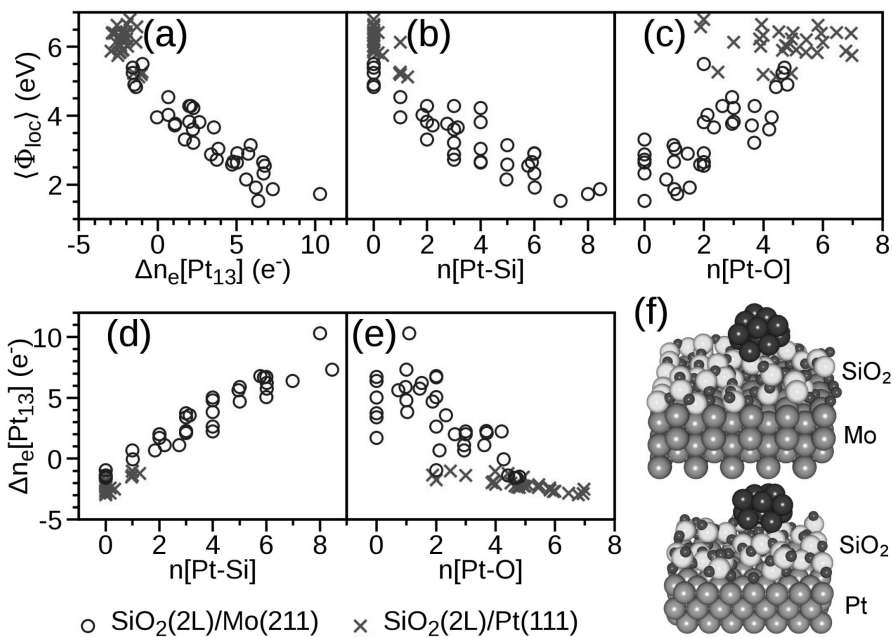


Figure 5.3: The charging propensity of a metal cluster adsorbed on the metal-adsorbed α -SiO₂ film in dependence of the local work function. The local work function of the supported Pt₁₃ cluster is determined as the average over the interfacial platinum atoms being in direct contact with the underlying α -SiO₂ surface. a) The excess/depletion of the number of electrons on the particular sampled cluster configuration, $\Delta n_e(\text{Pt}_{13})$. b, c) Average number of $n(\text{Pt-Si})$ and $n(\text{Pt-O})$ of bonds formed between interfacial platinum cluster atoms and the α -SiO₂ surface. d, e) Correlation between $\Delta n_e(\text{Pt}_{13})$ and $n(\text{Pt-Si/O})$ for each of the sampled Pt₁₃ cluster. f) Views of the calculated model systems including size-selected Pt₁₃ clusters on different α -SiO₂ thin films.

chamber. A defined pulse of ethylene is dosed and the formed ethane ($m/z = 31$) is recorded mass-spectrometrically within the quasi-steady-state region. In order to open dehydrogenation channels, the temperature is raised to 400 K for five pulses and afterwards the activity at 300 K is measured again. The turn-over frequency (TOF) at 300 K of clean Pt_n clusters before and after the induced deactivation at 400 K is shown in figure 5.4 a). An identical activity is found for Pt₁₀ clusters on each support system, whereas Pt₁₃ clusters are more reactive on α -SiO₂/Mo(211) than on α -SiO₂/Pt(111). The reverse is found for Pt₁₄ clusters supported on α -SiO₂/Pt(111) having higher activity than those supported on α -SiO₂/Mo(211). The activity for hydrogenation not only depends on electronic factors, but also on additional effects, e.g. increased required active site by co-adsorption in contrast to intramolecular dehydrogenation.

After the temperature step to 400 K, Pt₁₀ on α -SiO₂/Pt(111) shows lower activity than before, but Pt₁₃ and Pt₁₄ retain their initial catalytic activity. In strong contrast to α -SiO₂/Pt(111) as support material, all cluster sizes on α -SiO₂/Mo(211) show almost vanished reactivity after 400 K. This percent change in TOF induced by dehydrogenation is given in figure 5.4 b). All cluster sizes on α -SiO₂/Mo(211) showed deactivation between 100 and 80%, whereas the same

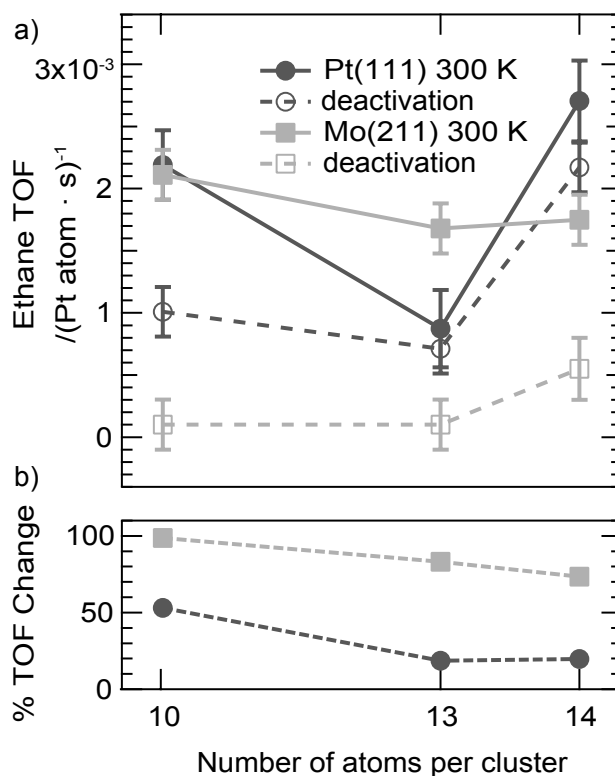


Figure 5.4: Pulsed molecular beam reactive scattering of ethylene and deuterium on size-selected Pt clusters supported on either a-SiO₂/Pt(111) or a-SiO₂/Mo(211) thin films: a) Measured ethane TOF of Pt_{10,13,14} at 300 K during quasi-steady-state region of a defined ethylene pulse and a background pressure of $p = 2 \cdot 10^{-6}$ mbar D₂ along with additional deactivation (activity at 300 K after temperature step to 400 K). b) Percent change in TOF between activity at 300 K and after temperature increase to 400 K as a function of cluster size and support system.

cluster sizes on a-SiO₂/Pt(111) showed a maximum decrease of 50% for Pt₁₀ and 0% for Pt₁₃ and Pt₁₄.

This effect can be explained by charging effects caused by the local work functions of the thin films. On the one hand, the a-SiO₂ film on Mo(211) has an increased electron density caused by the low work function of molybdenum and acceptor-like CMIGS created by covalent Mo-O bonds formed at the interface. This excess electron density is transferred to adsorbed Pt clusters, which become negatively charged. The accumulation of negative charges facilitates the formation of dehydrogenated species at elevated temperatures. On the other hand, the a-SiO₂ film on Pt(111) is characterized by the high work function of platinum and the absence of CMIGS leading to electron-deficiency. As a consequence, the thin film withdraws e^- -density of adsorbed clusters leading to increased resistance towards poisoning.

5.3 Conclusions

In conclusion, the ethylene hydrogenation catalyzed by size-selected Pt_n clusters supported on two different a-SiO₂/metal systems has been studied. The underlying single crystal not only determines the geometrical arrangement of atoms within the silicate films, but also electronically affects the films by penetration of the metal work function. Both effects lead to (de)charging of the silicate thin films resulting in different local work functions. The local work function is crucial in order to understand the local e^- -density of supported metal clusters. It was shown, that a high local work function as realized in the Pt₁₃/a-SiO₂/Pt(111) model system leads to positive charging of the cluster effectively preventing formation of carbonaceous species, whereas a low local work function leads to partially negatively charged clusters favoring dehydrogenation as evidenced by the Pt₁₃/a-SiO₂/Mo(211) system. The local work function, which can also be used in industrial practice by implementing dopants into the support material, represents an additional, yet underestimated, parameter for controlling and steering of catalyzed reactions besides more obvious parameters such as particle size. Although the experiments were performed using sub-nm sized metal clusters, the finding is general and can also be applied for perimeter activation of larger nanoparticles. The local work function might not only play a role in optimizing catalysts, but is also essential in electronic applications as the system Pt/SiO₂ is omnipresent. Consequently, the insights gained in this study might also be applicable when building electronic devices in the sub-nm size regime.

ETHYLENE HYDROGENATION ON Pd NANOPARTICLES

Palladium based systems are extensively used in a wide range of catalytic hydrogenation reactions. In this chapter, electronic modifications of two α -SiO₂ thin films are used to influence the properties of supported Pd nanoparticles (~1 nm). Negative charging of the metal particles leads to destabilization of both, surface and subsurface, hydrogen species, whereas positive charging leads to stabilization of both hydrogen species as evidenced by TPD measurements. The impact of this finding for general hydrogenation reactions is illustrated for ethylene hydrogenation at 300 K using a pulsed molecular beam technique, where an increase in TOF over one order of magnitude is observed for positively charged particles. The difference in hydrogenation TOF can be rationalized by two reasons: (i) increased hydrogen coverage on the metal surface due to stabilization and (ii) reduction in activation barrier for hydrogenation, both caused by metal-support interactions. In addition, the active phase of the metal particles during catalysis is proposed to be influenced by two mechanisms, formation of a carbide phase and a dehydrogenated carbonaceous overlayer on the surface.

6.1 Introduction

Palladium based catalysts play an important role in hydrogenation reactions of unsaturated hydrocarbons and have received ongoing scientific attention since Lindlar first described a class of catalysts named after him in 1952 [92]. However, in the case of alkenes, the mechanistic basis was paved already in 1934, when Horiuti and Polanyi proposed a reaction scheme, in which half-hydrogenation of ethylene caused by dissociated hydrogen atoms leads to an alkyl-intermediate, which is sequentially hydrogenated to give the final product ethane [14].

Ongoing research revealed, that the overall activity and selectivity of supported Pd catalysts depends on several inter-correlated subtleties effectively leading to a much more complicated picture on the molecular level than based on the Horiuti-Polanyi mechanism [48, 211–216].

These factors can be generously divided into the actual surface chemistry and subsurface chemistry. Two modes of ethylene adsorption on the surface have been identified: a di- σ or π -bonded species [217]. The former is thought to be responsible for the formation of ethylidyne, whereas the latter can be effectively hydrogenated to ethane. Ethylidyne and other dehydrogenated species on metal surfaces are mainly believed to be spectator species blocking adsorption sites [140, 179, 218], although slow hydrogenation of these (compared to the overall hydrogenation rate) has been observed experimentally on platinum [219, 220]. It has also been proposed, that these carbonaceous species act as a hydrogen reservoir during catalysis [221, 222].

Besides the formation of dehydrogenated species on the metal surface, the chemistry in the subsurface region is of paramount importance in the case of Pd nanoparticles, which are often found to exhibit a carbide phase either formed during catalysis [223–225] or intentionally introduced *a priori* [226, 227]. Carbon atoms incorporated in the subsurface region of the metal were found to control the availability of subsurface hydrogen species, which would otherwise lead to formation of a hydride phase in the absence of the hydrocarbon [228]. The availability of hydrogen on and below the metal surface is thought to determine the activity and selectivity of the catalyst during alkyne hydrogenation [229]. For Pd nanoparticles with a diameter between 1.3 and 4.8 nm supported on thin alumina films, the desorption temperature and the ratio between subsurface to surface hydrogen were shown to be dependent on particle size [217]. To the best of the authors knowledge no study has been reported so far concerning the question, whether these properties of identical Pd nanoparticles can be tuned by the appropriate choice of the support system under ultra-high vacuum conditions (UHV).

In the present work, the metal-support interaction between two modified α -SiO₂ supports and Pd nanoparticles with a narrow size distribution of 0.9–1.4 nm was investigated under UHV conditions. First, the influence of the support on the ability of Pd nanoparticles to form (sub)hydrogen species is demonstrated by D₂-temperature-programmed desorption (TPD). To further illustrate the impact of support-dictated hydrogen species for catalytic reactions, the hydrogenation of ethylene was carried out under isothermal conditions. Besides the characterization of the involved hydrogen species, also the role of the hydrocarbon during reaction was tested by isotopic scrambling. After reaction, the Pd nanoparticles were used for *post-mortem* TPR and CO IRRAS in order to evaluate the active phase during catalysis.

6.2 Results and Discussion

As the same two model α -SiO₂ systems have been applied as support material for Pd nanoparticles, the results obtained experimentally and theoretically of chapter 5 are the foundation for the interpretation and discussion of support effects on Pd nanoparticles during ethylene and acetylene hydrogenation. The interested reader is referred to this chapter for a molecular, microscopic description of the processes involved. In short, the (de)-charging of size-selected Pt clusters on α -SiO₂ on Pt(111) and Mo(211) is decisively controlled by the local work function of the supports and this leads to changes in the electronic structure of supported clusters.

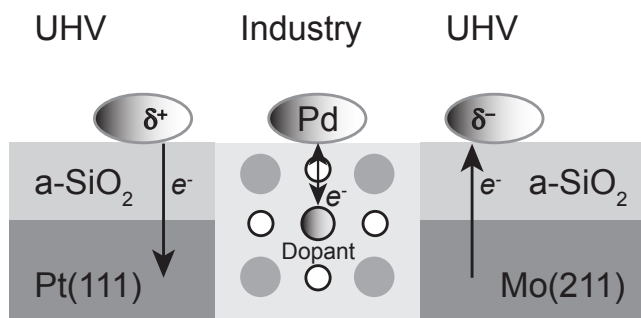


Figure 6.1: Schematic design of the two model systems: Two $a\text{-SiO}_2$ thin films as support material for Pd nanoparticles were grown on Pt(111) and Mo(211). Usage of Pt(111) as underlying metal leads to positively charged adsorbed particles, whereas Mo(211) results in accumulation of negative charges on the particles, and the amount of charge transfer is governed by the local work function of the support. The use of different underlying single crystals is comparable to purposely support doping in industrial catalysis, which is shown in the middle of the scheme [230].

For a rudimentary understanding, a macroscopic explanation based on general (de)-charging of Pd nanoparticles is given here keeping in mind the local nature of electron densities and the amorphous structure of the films. The films differ by the work function measured for the single crystals (5.9 eV for Pt(111) and 4.4 eV for Mo(211)), which penetrate into the silicate film due to the finite thickness of the latter [209]. The nature of the newly created metal induced gap states (MIGS) is controlled by the work function of the bare metals. In addition, the $a\text{-SiO}_2/\text{Mo}(211)$ support contains Si-O-Mo bonds at the interface between metal and metal oxide, which leads to an increased number of Si atoms at the surface, which were shown to negatively charge adsorbed metal particles [82]. These effects lead to a more negative charging of the adsorbed active component supported on $a\text{-SiO}_2/\text{Mo}(211)$ in comparison to $a\text{-SiO}_2/\text{Pt}(111)$. The charging, as an electronic effect, leads only to minor changes in particle morphology. A schematic drawing of the investigated model systems is given in figure 6.1.

6.2.1 Hydrogen Chemisorption

The influence of the support material on the capacity of Pd particles to form different hydrogen species was probed by D_2 -TPD summarized in figure 6.2. For the lowest investigated coverage, a single high temperature signal α at 310 K is observed for Pd supported on $a\text{-SiO}_2/\text{Pt}(111)$. Upon increasing coverage, a second low temperature signal β_1 located at ≈ 240 K appears and the high temperature signal shifts to lower temperature. The β_1 signal saturates with further increased dosage of D_2 . The same general behavior is found for identical Pd particles supported on $a\text{-SiO}_2/\text{Mo}(211)$, however the high temperature signal occurs already at 255 K and the low temperature signal at ≈ 180 K. This temperature shift indicates that the support material dictates the characteristics of adsorbed hydrogen species on the metal particles.

The appearance of at least two distinguishable signals during hydrogen desorption of Pd

nanoparticles is well documented in literature [226, 231, 232]. The high temperature signal α can be assigned to the desorption of hydrogen species initially residing on the metal surface. Upon increasing coverage, this signal shifts to lower temperature caused by the second order kinetics of the hydrogen recombination on the surface. In addition to the second order kinetics of the α signal, the appearance of the low temperature β_1 at high coverages is characteristic for the occupation of subsurface sites by hydrogen effectively weakening the adsorption strength of surface-bound H species [217]. In the case of Pd nanoparticles, this weakened adsorption strength by occupation of subsurface sites has been attributed theoretically by a shift of the Pd 4d states to lower energies with increasing hydrogen content reducing the number of states at the Fermi level and inducing a partial occupation of antibonding H-Pd states just below the Fermi level [233]. Following this line of argumentation, the temperature shift of ≈ 50 K as a function of support material reported in this work can be understood as an electronic effect. Negative charging of Pd nanoparticles as realized in the a-SiO₂/Mo(211) support system might lead to partial occupation of antibonding states just below the Fermi level, leading to destabilization of hydrogen species and accompanying lower desorption temperature. The results presented here also highlight the importance of controlled support synthesis, since electronic modifications of chemically identical supports can alter the behavior of supported metal particles.

6.2.2 Ethylene Hydrogenation

Having established the influence of metal-support interaction on different hydrogen species, the question arises, whether these characteristics can be used to steer catalytic activity. To answer this question, ethylene hydrogenation was investigated under isothermal conditions (300 K) using p-MBRS and the according results are summarized in figure 6.3.

Pd nanoparticles on a-SiO₂/Pt(111) show an initial ethane TOF of 11 (particle·s)⁻¹ and deactivate with increasing number of ethylene pulses. After 20 pulses, the ethane TOF of 5 (particle·s)⁻¹ decreased to 45 % of the initial value. Ethane, which additionally underwent HD-exchange, is shown in the subgraph of figure 6.3 and accounts to 4.3 ± 1.2 % of the stoichiometric product (averaged over twenty pulses). The starting ethane TOF of Pd supported on a-SiO₂/Mo(211) is 0.9 (particle·s)⁻¹ and consequently over one magnitude lower than the one observed for a-SiO₂/Pt(111). A similar deactivation is observed and d₃-ethane constitutes 2.4 ± 1.1 % of the formed product.

By comparison of figure 6.3 and 6.2, the change between the reactivity of both systems could be tentatively attributed to the difference in hydrogen adsorption strength, since the isothermal experiments were conducted at 300 K, indicated by the dashed vertical lines in figure 6.2. For Pd on a-SiO₂/Pt(111), the high temperature signal caused by surface hydrogen species is above 300 K, whereas on a-SiO₂/Mo(211), the signal occurs at 260 K, which is significantly below the temperature used for isothermal experiments. Keeping in mind the pulsed nature of the experiment ($f = 0.1$ Hz, 0.6 ms ethylene pulse width in $2 \cdot 10^{-6}$ mbar of D₂

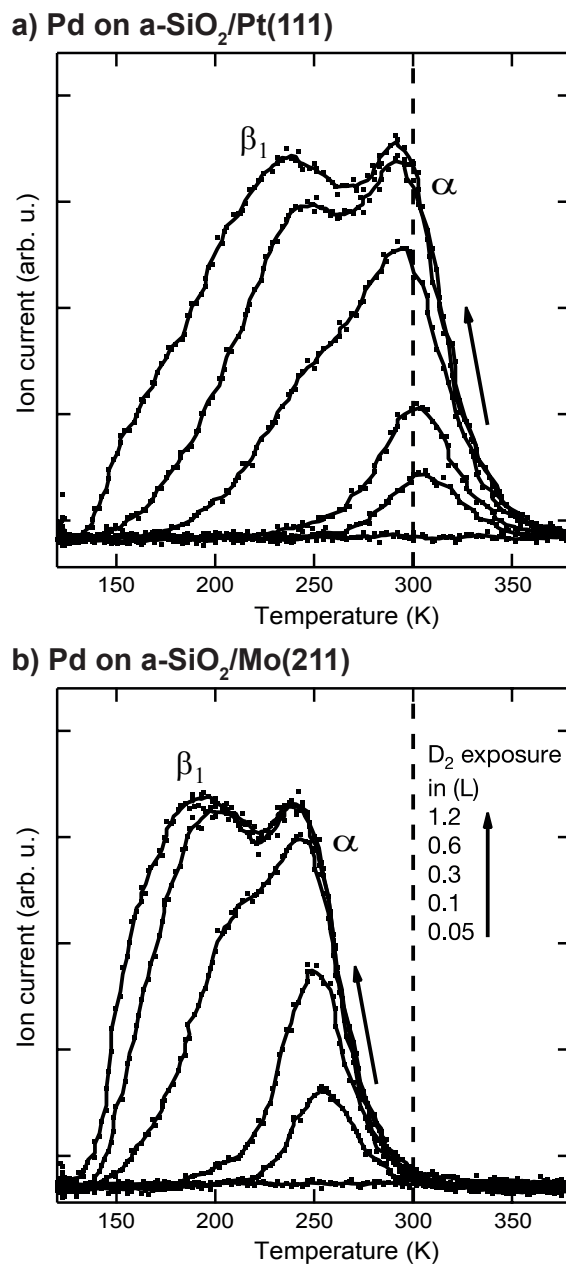


Figure 6.2: D₂-TPD spectra ($m/z = 4$) of Pd nanoparticles supported on (a) a-SiO₂/Pt(111) and (b) a-SiO₂/Mo(211) as a function of coverage. The dashed line at 300 K indicates the temperature, at which the activity under isothermal conditions is measured. In addition, the lowest curve in each case represents a blank measurement without metal particles showing that the underlying metals do not contribute to the spectra.

background pressure), this temperature difference leads to accumulation of hydrogen species in the case of $\alpha\text{-SiO}_2/\text{Pt}(111)$ resulting in a high atomic hydrogen coverage on the Pd particles in contrast to $\alpha\text{-SiO}_2/\text{Mo}(211)$, where desorption leads to a low effective hydrogen coverage on the metal particles. The difference in hydrogen coverage results in increased activity and a similar correlation between hydrogen adsorption strength (descriptive of surface coverage) and TOF for ethylene hydrogenation has been observed for a number of Pd/Re catalysts supported on alumina [234, 235]. However, the deactivation of both catalyst systems during ethylene hydrogenation studied in this work indicates, that additional factors influence the overall hydrogenation activity besides the effective hydrogen coverage.

6.2.3 Active Phase and Deactivation

To gain further insights into the catalysts active phase and deactivation, *post-mortem* TPR experiments were performed on the Pd nanoparticles, see figure 6.4. After ethylene hydrogenation using C_2H_4 and D_2 and post dosage of additional D_2 , the TPR spectra of both systems show two desorption signals of $m/z = 4$, but no desorption of $m/z = 2$. In comparison to D_2 -TPD of clean Pd particles, which also exhibits two signals, the low temperature signal is shifted to temperatures below 200 K, whereas the high temperature signal is located at ≈ 360 K. Replacing D_2 by H_2 during ethylene hydrogenation, but retaining post dosage of D_2 leads to desorption of molecular hydrogen between 300 and 400 K. Simultaneously, the low temperature signal of deuterium remains unchanged, but the high temperature signal above 300 K disappears.

Using these isotopic scrambling experiments, mechanistic details concerning the active phase during catalysis can be addressed. First, the high temperature signal is formed during catalysis, whereas the low temperature signal is caused by additional dosage of deuterium. The appearance of deuterium desorption above the reaction temperature is characteristic of dehydrogenation of a carbonaceous overlayer, e.g. ethylidyne. This is in accordance to a previous TPR study on Pd particles supported on an $\text{Al}_2\text{O}_3/\text{NiAl}(110)$ surface [217]. Here, the authors introduced a stepwise model, in which ethylene in di- σ adsorption converts to ethylidyne between 250 and 300 K, which is further dehydrogenated between 300 and 400 K to form a hydrogen-deficient carbonaceous deposit. This additional dehydrogenation is observed in the same temperature window as reported in this study.

The appearance of this dehydrogenation signal at identical temperature for both support systems indicates, that the nature of the formed carbonaceous overlayer is identical and irrespective of support system. The absence of hydrogen desorption ($m/z = 2$) during dehydrogenation for both support systems within the sensitivity of the experiments is remarkable, given the hydrogen-containing character of ethylene during hydrogenation. Typically, the conversion of ethylene to ethylidyne on Pd(111) is believed to follow a three step mechanism via consequential formation of vinyl, ethylidene followed by ethylidyne [44, 236]. However, more recently also a mechanism involving ethyl species was proposed for high atomic hydrogen concentrations [45]. Although the overall reaction results in dehydrogenation, this mechanism involves an addi-

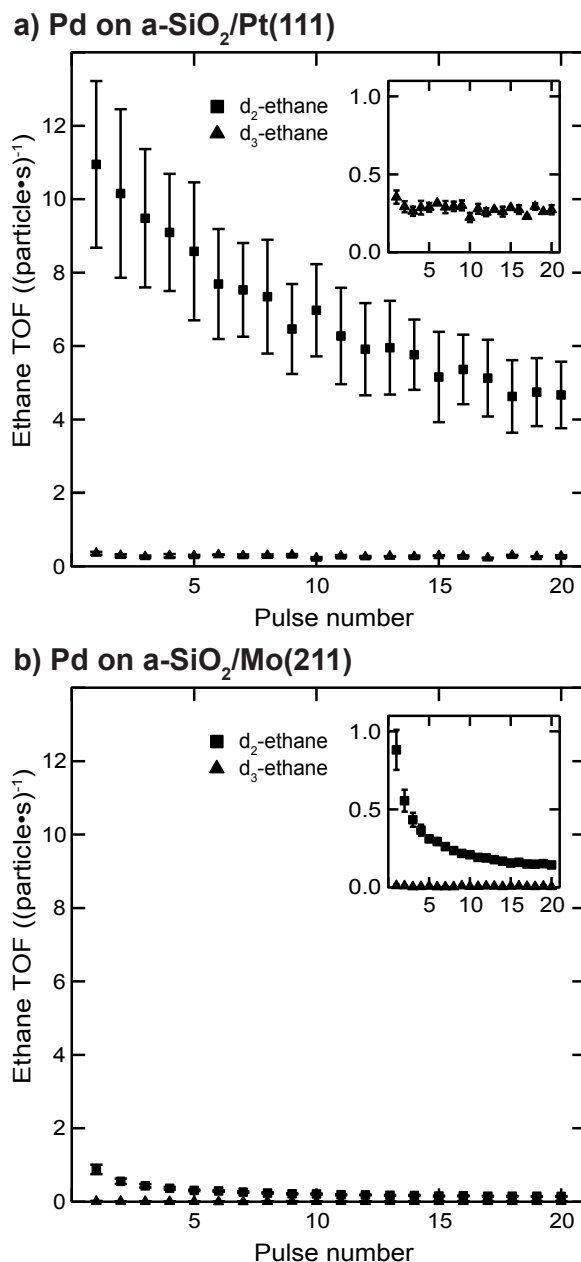


Figure 6.3: Activity results of supported Pd nanoparticles given as ethane TOF per Pd particle in progression of single ethylene pulses at 300 K. The m/z ratios = 31,33 were used to discriminate between stoichiometric d₂-ethane and HD exchanged d₃-ethane (see experimental for details). Pd nanoparticles supported on a-SiO₂/Pt(111) show an increased activity compared to a-SiO₂/Mo(211) as support material. In both cases, the particles deactivate over the course of the experiment and additional HD-exchange of ethane in small quantities is observed.

tional hydrogenation step, which could partially, but not fully, explain the HD-exchange of the adsorbed overlayer observed for supported Pd particles reported here. The role of the carbonaceous deposits during catalysis is still under debate and not fully understood [51]. Due to the full replacement of hydrogen by deuterium (also no HD at $m/z = 3$ is formed, data not shown), the experiments presented here clearly demonstrate, that these species are more than mere spectator species and have to act as a source of hydrogen atoms. The extent of this observation to the overall hydrogenation activity of the Pd particles can currently not be judged and requires further experimental insights.

Belated dosage of D_2 at 100 K after performing the reaction leads to molecular desorption below 200 K for both support systems (see figure 6.4, after reaction). This temperature is significantly lower than observed for clean metal particles, which can not solely be explained by the formation of a carbonaceous overlayer on the particles. Having performed similar experiments on supported, size-selected Pt clusters, we found, that for Pt clusters the formation of dehydrogenated species on the surface leads to completely vanished deuterium desorption after reaction and therefore not to a temperature shift [46]. As a consequence, this shift has to be caused by a phenomenon observable for Pd, but not for Pt particles under the applied reaction conditions. Palladium, either in the form of a metal or a particle, is known to form carbon deposits other than ethylidyne on the near-surface region [223, 224, 227]. These subsurface carbon deposits on Pd nanoparticles have been made responsible for lowering the activation barrier of hydrogen subsurface diffusion by destabilization of surface hydrogen species and expansion of the surface openings for penetration of hydrogen into the subsurface region [237]. These effects could explain the temperature shift observed in this work, and we therefore tentatively attribute the latter to the formation of carbon deposits below the surface besides the hydrogen containing species on the surface observable in figure 6.4.

To gain further insight into catalyst deactivation, CO IRRAS (displayed in figure 6.5) was performed before and after reaction, which is often used to characterize metal particles in combination with hydrocarbons [140, 141, 238]. Before reaction, the Pd spectra of both support systems show a single peak at 2100 cm^{-1} , with a broad feature at 1920 to 2000 cm^{-1} , corresponding to linear and bridge bonded CO, respectively. After ethylene pulsing, the bridge bonded disappears for Pd on $\alpha\text{-SiO}_2/\text{Mo}(211)$ and the on top species appears at 2089 cm^{-1} . In the case of $\alpha\text{-SiO}_2/\text{Pt}(111)$, the bridge bonded species loses intensity and the linear CO stretch is red-shifted to 2094 cm^{-1} .

The red-shift in CO frequency is typically associated with co-adsorbed carbonaceous species, which weaken the CO bond by increased metal back-donation into the $2\pi^*$ orbital. Having established the similar nature of the adsorbed dehydrogenated species (see figure 6.4), the change in frequency can be correlated to the amount of carbonaceous deposits. The shift of 6 cm^{-1} for Pd on $\alpha\text{-SiO}_2/\text{Pt}(111)$ compared to 11 cm^{-1} for $\alpha\text{-SiO}_2/\text{Mo}(211)$ indicates, that a higher amount of dehydrogenated species is formed for Pd supported on $\alpha\text{-SiO}_2/\text{Pt}(111)$ compared to $\alpha\text{-SiO}_2/\text{Mo}(211)$ as support. This observation is in line with the d-band model employed for ethylene dehydrogenation, where a close distance between E_F and center of

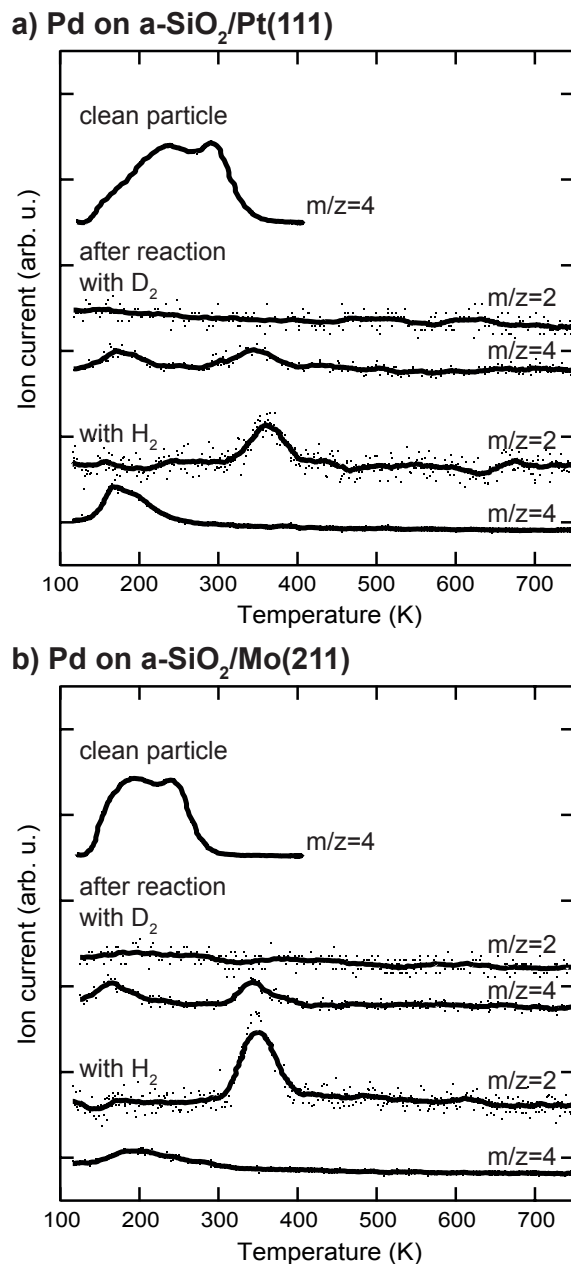


Figure 6.4: *Post-mortem* TPR spectra of Pd nanoparticles after ethylene hydrogenation. After the reaction is performed at 300 K using C₂H₄ and D₂, additional D₂ is dosed at 100 K and a TPR spectrum is recorded. For both support systems, two signals of D₂ are observed below 200 K and between 300 and 400 K (denoted as after reaction with D₂). In order to elucidate the origin of these signals, the same experimental procedure using H₂ instead of D₂ during ethylene hydrogenation at 300 K and post dosage of D₂ is performed (labelled as after reaction with H₂). The low temperature signal is caused by additional dosage of gas after reaction, whereas the high temperature signal originates from the reaction. The D₂-TPD spectra of the clean Pd particles are shown for comparison.

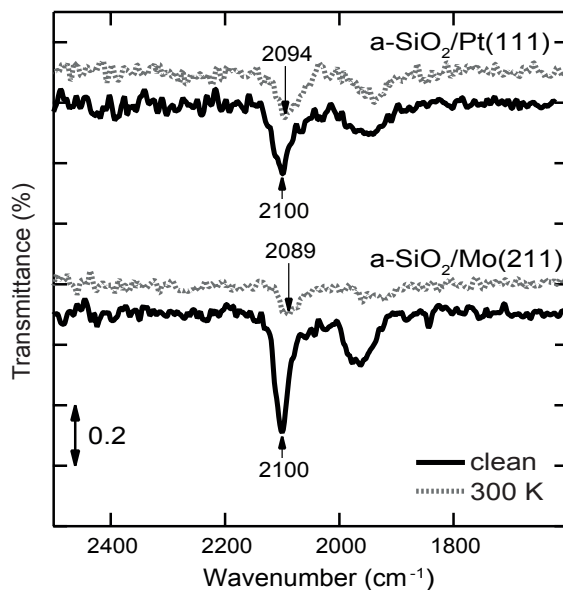


Figure 6.5: CO IRRAS data of Pd nanoparticles supported on $a\text{-SiO}_2/\text{Pt}(111)$ and $a\text{-SiO}_2/\text{Mo}(211)$: For the clean particles, linear and bridge bonded CO species can be observed (black, solid line), whereas after reaction at 300 K on-top species are red-shifted (gray, dashed line).

d-band favors dehydrogenation [239]. A similar situation is encountered here for supported particles, where an increased electron density dictated by the support material, in this case $a\text{-SiO}_2/\text{Mo}(211)$, leads to increased formation of the dehydrogenated species on the particle surface.

This charging effect is not observed for the linear CO stretch on clean particles, which occurs at 2100 cm^{-1} , in both cases. Two arguments might explain the absence of a notable change in CO frequency: Slightly bigger Pd nanoparticles supported on a basic MgO film of reference [138] show a linear CO frequency of 2098 cm^{-1} under identical experimental conditions, indicating that charge transfer between metal particles and support is more subtle than typical resolution employed in IRRA spectroscopy (4 cm^{-1}). In addition, the on top CO stretch measured here on single Pt atoms might not necessarily reflect the nature of the active site, since charge transfer is expected to be most pronounced for perimeter activation.

6.2.4 Influence of Metal-Support Interaction on Reaction Rate

It is evident from figure 6.2, that positive charging of supported Pd particles leads to stabilization of hydrogen on and below the surface, which results in an initially increased effective hydrogen coverage at 300 K during ethylene hydrogenation. However, after reaction and once the carbonaceous overlayer is formed, the involved hydrogen species do not differ significantly as evidenced by figure 6.4. At the same time, the ethane TOF measured for Pd supported on $a\text{-SiO}_2/\text{Pt}(111)$ is still one order of magnitude higher than for identical particles on $a\text{-SiO}_2/\text{Mo}(211)$ as seen in

figure 6.3, whereas Pd nanoparticles supported on a-SiO₂/Mo(211) show a higher amount of dehydrogenated species in figure 6.5.

These observations can be rationalized by charging arguments based on the d-band model [239, 240]. Nanoparticles supported on a-SiO₂/Pt(111) are charged positively relative to identical particles on a-SiO₂/Mo(211). The decreased electron density leads to an increased distance between the center of the d-band and E_F, whereas increased electron density on the particles decreases the distance. A high distance between these two was shown to be beneficial for hydrogenation and detrimental to dehydrogenation, and the reverse correlation is found for a decreased distance [239]. Based on this model, Pd particles on a-SiO₂/Pt(111) should have a higher resistance towards dehydrogenation and a lowered activation barrier for hydrogenation, resulting in higher activity in comparison to a-SiO₂/Mo(211) as support system, which fits the experimental results of this work.

Based on the Horiuti-Polanyi mechanism, the ethylene hydrogenation proceeds via two consecutive additions of atomic hydrogen, each including intrinsic activation barriers. On Pd(111), the rate determining step was proposed to be the first addition to form an ethyl species under UHV conditions [241]. A recent first-principles microkinetic model study confirmed the first hydrogenation step to be the most important one for palladium, even under increased pressure conditions, but recognized a small contribution of the second step to the overall activity by the degree of rate control analysis [242]. Due to the importance of the first hydrogenation step, the TOF could be increased to a larger extent by reduction of the first barrier than by similar reduction of the second one [242]. Taking into account the large difference in ethane TOF reported here, which can not solely be explained by a difference in active sites, it seems likely, that in particular the activation barrier for the first hydrogenation step is reduced in the case of Pd supported on a-SiO₂/Pt(111). In figure 6.3, an identical HD-exchange rate was found for both catalytic systems within the error of the measurements. This additional exchange is caused by reverse reaction from ethyl to ethylene and hydrogen and represents no contradiction to a reduced activation barrier for the first hydrogenation step, since the reverse reaction is inhibited by a large activation energy [242].

6.3 Conclusions

In the present work, the influence of metal-support interactions between Pd nanoparticles and two a-SiO₂ supports for hydrogenation reactions is provided. In particular, the doping of the support material causing charge transfer to the metal particles was mimicked under UHV conditions by changing the underlying single crystal and the following key conclusions were reached:

1. The doping of the support material can be used to control different hydrogen species on Pd nanoparticles. Decreased electron density leads to stabilization of (sub)surface hydrogen species, whereas increased electron density results in destabilization. This opens up

the avenue to improve supported metal particles for all reactions involving hydrogen by additional fine-tuning of the support besides particle size.

2. After ethylene hydrogenation, the particles were found to exhibit a dehydrogenated overlayer, which completely exchanged hydrogen by deuterium. This incorporation of deuterium contradicts the commonly believed spectative character of the adlayer, which is generally assumed during mechanistic discussions. This finding should encourage further research devoted to the contribution of the adlayer to the overall catalytic activity.
3. Electronic modifications of metal-support interactions not only affect the adsorption properties of hydrogen, but also of hydrocarbons. In the particular case of isothermal ethylene hydrogenation, an increased activity of one order of magnitude is observed, which can be rationalized by a reduced activation barrier for hydrogenation. At the same time, the higher hydrogenation activity results in lower formation of dehydrogenated carbonaceous species on the surface.

6.4 Some Additional Remarks

This chapter has shown that metal-support interactions can have a significant impact on the hydrogenation of ethylene catalyzed by supported Pd nanoparticles. However, measuring a difference of one order of magnitude in catalytic activity on identical nanoparticles should make one suspicious, whether the results obtained are trustworthy or, if that is the case, the explanation and model applied is correct.

The robustness of all experimental data is decisively controlled by the effort put into disproving the results obtained. As noted earlier in chapter 2, the effective coverage for Pd nanoparticles supported on α -SiO₂/Pt(111) had to be lowered from $4.5 \cdot 10^{12}$ to $0.3 \cdot 10^{12}$ particles per sample due to saturation effects of the used oscilloscope¹. This saturation behavior of $m/z = 31$ has not been observed for any system investigated so far, although ethylene hydrogenation using p-MBRS under the same experimental conditions has become a standard experiment [46, 138]. The coverage of $4.5 \cdot 10^{12}$ particles supported on α -SiO₂/Pt(111) has been used > 18 times for ethylene hydrogenation over the course of this work due to its application as a pretreatment of the Pd particles for acetylene hydrogenation presented in chapter 7. The atypical saturation effect has been observed each time for that particular coverage. Lowering the coverage to $1.8 \cdot 10^{12}$ particles led to initial saturation for the first pulses, whereas only at the end the whole pulse was measurable due to deactivation over the number of pulses. Only for the low coverage stated above (measured four times), all pulses were within the detection limit. After normalization to the amount of particles, the TOFs determined for each particular coverage were identical as expected for non-interacting metal particles.

To exclude any systematic error of the QMS, the ethylene hydrogenation was additionally performed under the same conditions using C₂D₄ and $m/z = 36$ instead of C₂H₄ and $m/z = 31$.

¹The measured quantity is a voltage after pre-amplification of the QMS, which can vary between 0 and 10 V.

Taken into account the different cracking patterns of the two possible ethane products, the activity was close to the one previously observed in the standard experiment and significantly higher than for nanoparticles on α -SiO₂/Mo(211). This leads to the conclusion, that the data presented here is indeed correct, but raises the question for alternative explanations.

The first possibility evolves from the role of the support for Pd nanoparticles supported on α -SiO₂/Pt(111) during ethylene hydrogenation. This active participation of the support material might lead to the creation of a capture zone by either direct or reverse spill-over, which was used to explain CO oxidation of size-selected Pd clusters supported on MgO(100). The direct spill-over would, in this case, lead to ethylene or hydrogen adsorption onto the support and subsequent diffusion to the active metal component, where the reaction takes place. However, this mechanism should be to a first approximation independent of the metal actually used for hydrogenation. As the significantly increased activity was not observed for any of the several Pt_n cluster sizes (n between 7 and 14) under identical conditions, direct spill-over can be excluded. The reverse spill-over of ethylene from the particle to the support would not enhance ethane production during the limited time frame of single pulses, but rather increase the background by constant diffusion-hydrogenation processes as the background pressure of D₂ is kept constant throughout the experiment. Diffusion of dissociatively adsorbed D₂ on the metal to the support would result in the formation of surface silanol groups, which have not been observed experimentally by IRRAS experiments. At this point a catalytic participation of the support material can be ruled out.

A second alternative mechanism centers around the stability of the support material *per se*. This idea stems from the scientific graphene community, which has shown that small molecules, e.g. hydrogen and oxygen, can diffuse between graphene and the underlying metal by grain boundaries [243, 244]. Given the finite thickness of the α -SiO₂ films reported in this work, the main issue might be an active contribution of the underlying metal, in this case Pt(111), during catalysis by diffusion of small molecules and not only an electronic effect as described earlier in this chapter. Several experimental observations are useful to exclude this possibility: First, the film thickness is practically unchanged after performed reaction as evidenced by AES. Second, diffusion of ethylene through the support to the Pt(111) single crystal would result in the formation of ethylidyne under the applied reactions conditions, which should be detectable by the $\delta_{Umbrella}$ mode at 1339 cm⁻¹ in the IRRA spectrum. This vibration has not been experimentally verified in the present work. Alternatively, CO IRRAS could be used indirectly to detect ethylidyne on Pt(111) as the CO stretch shifts to 2020 cm⁻¹ in the presence of ethylidyne on Pt(111). As can be seen in figure 6.5, this frequency was not observed in any of the CO IRRA spectra shown in this chapter. Diffusion of hydrogen (or deuterium) to the Pt(111) surface should result in the typical desorption feature at 300 K known by coverage-dependent H₂-TPD experiments on Pt(111) [170]. Given the low amount of Pd nanoparticles in comparison to the underlying Pt(111) single crystal this should result in a considerably higher amount of D₂ desorption during *post-mortem* TPR shown in figure 6.4. However, the opposite trend is found for Pd nanoparticles supported on α -SiO₂/Pt(111) in comparison α -SiO₂/Mo(211), which

can be satisfactorily explained by the amount of dehydrogenated species on the particle surface. In light of the reasons outlined above, a contribution of the underlying Pt metal other than based on electronic effects can be rejected.

One last point concerns the comparability between isothermal p-MBRS and TPR experiments. To this end, additional TPR experiments shown in figure 6.6 were performed on both support systems. Here, ethane desorption monitored by $m/z = 31$ and 32 is observed in similar quantities below 200 K for both support systems. Desorption of molecular hydrogen ($m/z = 2$) is detected at 273 K and 231 K for Pd nanoparticles supported on a-SiO₂/Pt(111) and a-SiO₂/Mo(211), respectively. The initially in excess dosed D₂ is completely consumed for HD-scrambling and hydrogenation as evidenced by the absence of any signal for the m/z ratio of 4. Based on the results presented in figure 6.6, a similar hydrogenation activity could be expected for Pd nanoparticles supported on both systems in strong contrast to the TOFs determined by p-MBRS experiments in this chapter.

This obvious discrepancy between the two experimental techniques is caused by the difference between the quasi steady-state (p-MBRS) and non steady-state (TPR) conditions applied during both experiments. The desorption temperature of ethane observed in the TPR experiments is significantly lower than the one of deuterium desorption. In other words, the activation barrier for hydrogenation is lower than the desorption barrier of molecular D₂. As a consequence, all available deuterium species are used for hydrogenation before the energy barrier of desorption can be surmounted, which is supported by the absence of molecular deuterium desorption. Since the total amount of D₂ is almost identical for Pd particles on both support systems, the overall hydrogenation signal of ethane is comparable as a consequence of these low hydrogenation barriers. On the other hand, residual ethylene adsorbed on the metal nanoparticles dehydrogenates at different temperatures as observed by molecular hydrogen desorption. This temperature difference between the two support systems reflects the lower dehydrogenation barriers for negatively charged particles also encountered during isothermal conditions. In summary, the experiments shown in figure 6.6 are not contradictory to the results obtained under quasi steady-state conditions due to the low activation barrier for hydrogenation. However, they illustrate the difficulty to extract valuable kinetic data from TPR experiments as the obtained results dramatically depend on the activation barriers for all processes on the surface. Direct comparison between quasi steady-state and non steady-state experiments should only be made with great vigilance and when all reaction pathways are known.

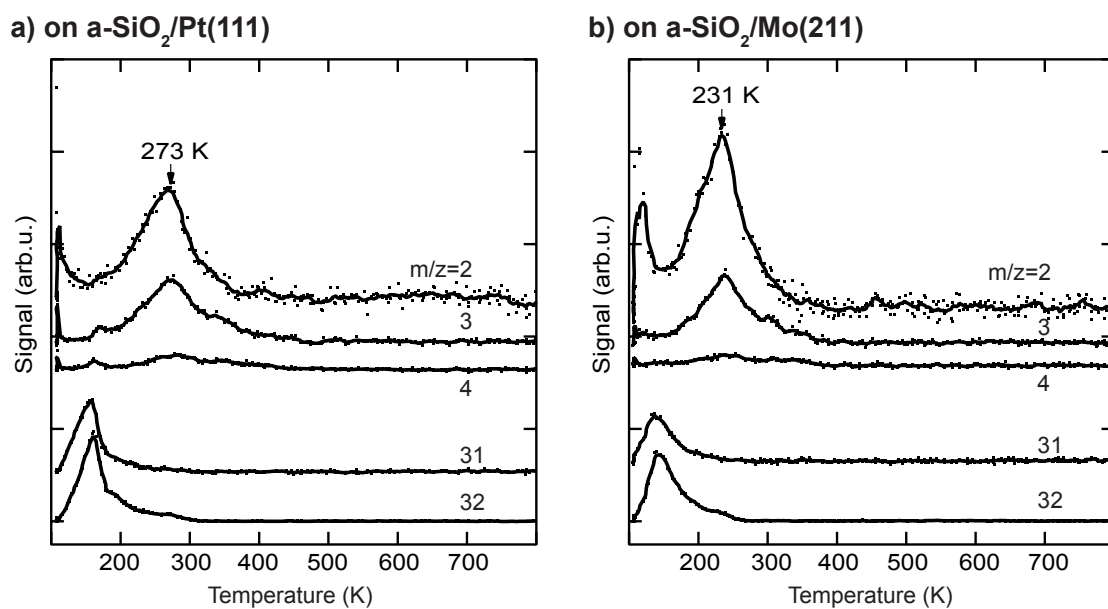


Figure 6.6: TPR spectra of D₂ and ethylene on Pd nanoparticles supported on a-SiO₂/Pt(111) (a) and a-SiO₂/Mo(211) (b): 0.4/SA D₂ followed by 0.4/SA ethylene are dosed at 100 K. The coverage of $4.5 \cdot 10^{12}$ particles per 0.785 cm^{-2} support area was used in both cases.

ACETYLENE HYDROGENATION ON Pd NANOPARTICLES

The selective hydrogenation of acetylene catalyzed by Pd nanoparticles is industrially used to increase the purity of ethylene. Despite the implementation of Pd based catalysts on an industrial scale, little is known about metal-support interactions on a fundamental level due to the complexity of these systems. In this study, the influence of metal-support interactions between Pd nanoparticles and two electronically modified α -SiO₂ thin films on acetylene hydrogenation is investigated under ultra-high vacuum (UHV) conditions. The hydrogenation is performed under isothermal reaction conditions using a pulsed molecular beam reactive scattering (p-MBRS) technique. Besides the activity and selectivity of clean Pd particles also the impact of dehydrogenated species intentionally introduced *a priori* is elucidated, whereas the active phase of the catalyst is additionally characterized by CO infrared reflection-absorption spectroscopy (IRRAS) and *post-mortem* temperature-programmed reaction (TPR). Metal-support interactions are found to influence the catalytic properties of Pd particles by charge-transfer, where positive charging leads to increased activity for acetylene hydrogenation. However, the increased activity is accompanied by formation of undesired byproducts. The active sites for acetylene and ethylene hydrogenation are shown to be different as previously proposed by the A and E model. The availability of the two different active sites on the Pd nanoparticles is determined by dehydrogenated species, whose nature and stability can be tuned by metal-support interactions. Based on these findings an electronic model is proposed for how acetylene hydrogenation selectivity can be steered solely by metal-support interactions leading to *in situ* blocking of unselective sites.

7.1 Introduction

The selective hydrogenation of acetylene to ethylene is of industrial importance during purification of ethylene feedstocks [33, 53]. Ethylene as a commodity chemical is produced by

non-selective thermal or catalytic cracking of naphtha fractions and typically contains 0.2 to 2% of acetylene. Before further processing, the amount of acetylene has to be lowered (preferentially < 5 ppm), since acetylene acts as a catalyst poison in downstream processes. In order to achieve these requirements, acetylene is removed by partial hydrogenation to ethylene avoiding fully saturating to ethane.

Due to its intrinsic high activity and selectivity, palladium in alloy form is the metal of choice for this process and much effort has been put into understanding the underlying phenomena determining catalytic performance [231, 245–252]. However, investigations on these catalytic systems are complicated by the numerous reaction products and the rich chemistry of the Pd metal itself. Although ethylene is the only desired product, complete hydrogenation to ethane can occur either by direct conversion of acetylene, or from excess ethylene. Further complicating matters, CC-coupling reactions lead to the formation of green oil effectively poisoning the catalyst [253]. The oligomerization is believed to initially proceed via buta-1,3-diene, which can either further polymerize or form benzene [241]. Even single Pd atoms supported on MgO(100) have been shown to catalyze this intermolecular cyclotrimerization [185, 186].

The product distribution is decisively controlled by the physical state of the metal catalyst [223, 254, 255]. The oligomerization products residing on the metal surface block active sites and compete with smaller dehydrogenated species formed upon adsorption of unsaturated hydrocarbons on Pd. The most prominent example of the latter is ethynidyne formed by either acetylene or ethylene [256, 257], although various other species have been proposed. Besides these surface species, the subsurface of the Pd metal is believed to be crucial for overall catalyst performance as Pd tends to form hydrides and carbides depending on reaction conditions and particle size [226, 229, 258, 259].

All of these factors combined hamper investigations on these systems since they are inter-correlated and minor changes to one experimental parameter, e. g. particle size, might also alter others in an unforeseen way. Consequently, structure-activity relationships on a molecular level are elusive for acetylene hydrogenation on Pd. Model catalysis under ultra-high vacuum (UHV) conditions allows for the investigation of single parameters while keeping others constant. For instance, in the previous chapter it was shown that nano-engineering of the support material can be used to (de)-charge Pd nanoparticles in the size range of 0.9-1.4 nm supported on amorphous silica (a-SiO₂). The underlying effect is similar to doping of the support material in industrial chemistry and can be used to increase ethylene hydrogenation activity by one order of magnitude and at the same time decrease the amount of carbonaceous deposits. On the basis of these results, the scope of this work was inspired by two main questions: can (de)-charging of Pd nanoparticles by metal-support interactions also be used to steer catalytic activity for acetylene hydrogenation, and if this is the case, what is the impact on overall selectivity?

7.2 Results

Activity results of acetylene hydrogenation catalyzed by Pd nanoparticles are shown in figure 7.1 with (a) a-SiO₂/Pt(111) and (b) a-SiO₂/Mo(211) as support material. The reactivity of the same particles is measured either as initially clean or after previous introduction of C₂H_x species and carbides, which is labelled as 'after ethylene hydrogenation'.

Clean particles deactivate over the course of the experiment irrespective of support material due to the formation of dehydrogenated species and limited desorption of acetylene. At the beginning, Pd nanoparticles supported on a-SiO₂/Pt(111) show higher ethylene production compared to the same particles supported on a-SiO₂/Mo(211). In both cases not only the stoichiometric reaction product, ethylene-D₂, is formed, but also significant amounts of ethylene-D₃, which additionally exchanged hydrogen with deuterium. However, the higher acetylene hydrogenation activity of Pd particles supported on a-SiO₂/Pt(111) is accompanied by additional overhydrogenation to ethane as evidenced by initial desorption of ethane-D₄ and ethane-D₅, which is not observed for a-SiO₂/Mo(211) as support. No desorption of C₄-molecules can be detected for clean particles, whereas higher benzene formation is shown by particles on a-SiO₂/Pt(111) with a maximum activity after several pulses of acetylene.

After performing ethylene hydrogenation, a higher initial catalytic activity is observed for Pd particles supported on a-SiO₂/Pt(111) compared to clean particles. More ethylene-D₂ as well as ethylene-D₃ is formed. No desorption of C₄-moieties can be detected, but an increase in benzene formation is observed. The ethane-D₄ background is increased and small amounts of ethane-D₅ desorb during the first pulses. In contrast to a-SiO₂/Pt(111), Pd nanoparticles on a-SiO₂/Mo(211) show slightly decreased catalytic activity for ethylene and ethane after ethylene hydrogenation. Production of C₄-moieties follows that of benzene, which is not observed for clean particles.

More information about the physical state of the metal nanoparticles is necessary in order to understand the activity results shown in figure 7.1. To this end the Pd nanoparticles are further characterized by *post-mortem* TPR and CO IRRAS to gain insight into species residing on the particle.

After isothermal acetylene hydrogenation at 250 K the catalysts are cooled to 100 K and additional D₂ is dosed. The resulting TPR spectra after reaction are summarized in figure 7.2 for particles supported on a-SiO₂/Pt(111) (a) and a-SiO₂/Mo(211) (b). No deuterium desorption ($m/z=4$) is observed for initially clean particles on a-SiO₂/Pt(111) after acetylene hydrogenation. Several desorption features of C₄-species ($m/z=54, 56$) and benzene ($m/z=78$) can be detected above 250 K. Subsequent performance of ethylene and acetylene hydrogenation leads to a broad desorption signal of deuterium. Particles supported on a-SiO₂/Mo(211) show D₂ desorption at 350 K and higher hydrocarbons desorb above 300 K. The amount of benzene desorption is significantly lower than for particles on a-SiO₂/Pt(111).

IRRA spectra of CO adsorbed on Pd nanoparticles before and after reaction are displayed in figure 7.3 for (a) a-SiO₂/Pt(111) and (b) a-SiO₂/Mo(211), respectively. For both support systems

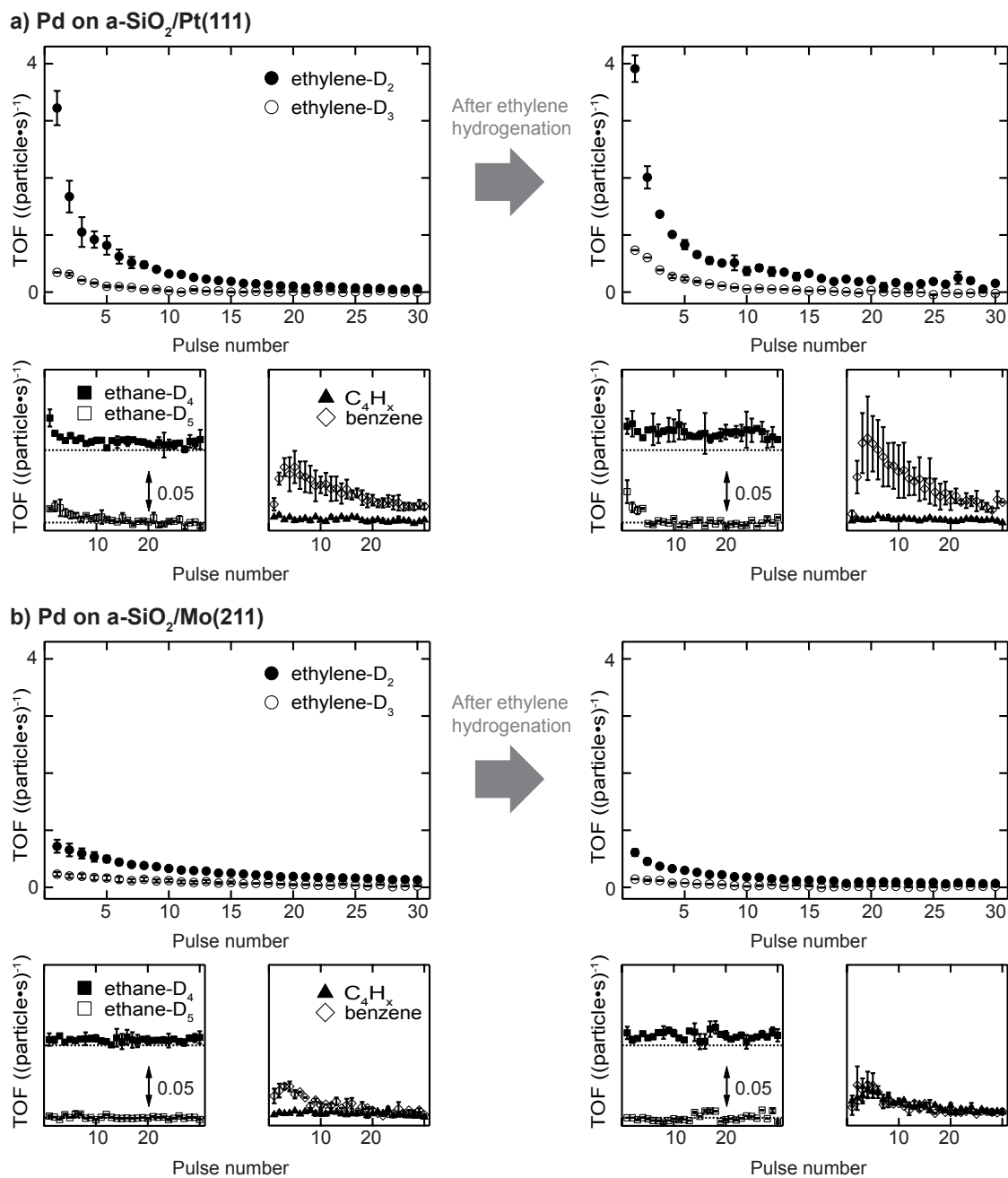


Figure 7.1: Activity results for acetylene hydrogenation catalyzed by Pd nanoparticles supported on a-SiO₂/Pt(111) (a) and a-SiO₂/Mo(211) (b). The reaction is performed at 250 K using a p-MBRs technique and the TOFs for different reaction products are given as a function of pulse number. Each support system exhibits three subfigures devoted to ethylene as the main product, ethane and oligomerization. Note that ethane-D₄ exhibits an offset in ethane subfigures indicated by the dotted line for better visibility. For each support the activity of initially clean and poisoned metal particles is given, where the poisoning is achieved by previous ethylene hydrogenation (see Experimental for details).

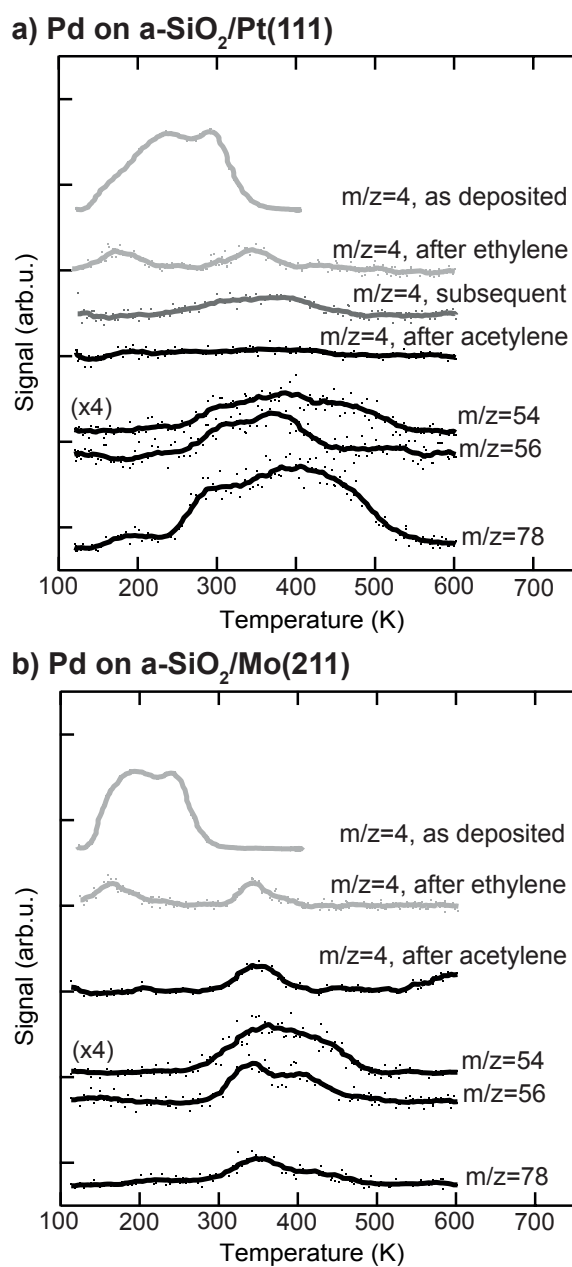


Figure 7.2: *Post-mortem* TPR spectra of Pd nanoparticles supported on a-SiO₂/Pt(111) (a) and a-SiO₂/Mo(211) (b) after acetylene hydrogenation. Additional D₂ is dosed at 100 K after reaction at 250 K using C₂H₂ and D₂, and a TPR spectrum is recorded (black). D₂-TPR spectra of particles as deposited without hydrocarbon hydrogenation and after exclusive ethylene hydrogenation are given in grey. In the case of Pd particles supported on a-SiO₂/Pt(111), an additional trace $m/z = 4$ is given for ethylene hydrogenation followed by acetylene hydrogenation denoted as subsequent.

linear and bridge bonded CO species can be observed for clean particles and after ethylene hydrogenation the linear species are red-shifted due to carbonaceous deposits on the metal particles. After acetylene hydrogenation the linear CO stretch frequency is further red-shifted for particles supported on a-SiO₂/Pt(111), depending on reaction temperature or pretreatment with ethylene (denoted as subsequent in figure 7.3). In the case of particles supported on a-SiO₂/Mo(211), no CO bands can be detected after acetylene hydrogenation regardless of reaction temperature and preconditioning.

7.3 Discussion

The discussion section is divided into two parts. The first part deals with the activity and selectivity of clean particles and the influence of support material on overall catalytic performance. In the second section the impact of preconditioning on the supported Pd nanoparticles is discussed and the effect of the dehydrogenated overlayer is elucidated.

7.3.1 Metal-Support Interactions on Clean Particles

Electron-poor particles supported on a-SiO₂/Pt(111) show higher acetylene hydrogenation activity compared to electron-rich particles supported on a-SiO₂/Mo(211) as can be seen in figure 7.1. The same effect, although more pronounced, has been observed for ethylene hydrogenation on the same particles in the previous chapter. The difference in ethylene activity has been rationalized by charging arguments based on the d-band center (ϵ_D) in comparison to the Fermi energy (E_F) when looking at the particle as an entity or varied localized electron densities for an active ensemble of metal atoms [239]. Here, a large distance between ϵ_D and E_F favours hydrogenation, whereas decreased distance leads to dehydrogenation by electron-backdonation of the metal to the σ_{CH^*} orbital of ethylene or ethyl adsorbed on the surface. This ethylene hydrogenation model was shown to be applicable to small metal nanoparticles in the nanometer size range comprised of either Pt, Pd or Ni supported on MgO(100) [138]. During ethylene hydrogenation, the adsorption of the olefin is described by the Dewar-Chatt-Duncanson model [20], which was also applied theoretically to the interactions between alkynes and metals [260, 261]. Following these descriptions of bonding, the increased activity of Pd nanoparticles on a-SiO₂/Pt(111) can be attributed to an electronic effect, where decreased electron density at the metal leads to weaker back-donation and consequently higher hydrogenation activity.

The mechanism of acetylene hydrogenation is believed to follow a Horiuti-Polanyi mechanism analogous to ethylene [14], in which sequential addition of atomic hydrogen to adsorbed acetylene leads first to a vinyl-intermediate followed by ethylene formation. Subsequently, ethylene can either desorb or be further hydrogenated to undesired ethane. This overhydrogenation to the alkane involves an alkyl-intermediate on the metal surface. During ethylene hydrogenation on the same system, it was shown in the preceding chapter that the backreaction from adsorbed alkyl to ethylene is negligible, since this reaction would involve significant

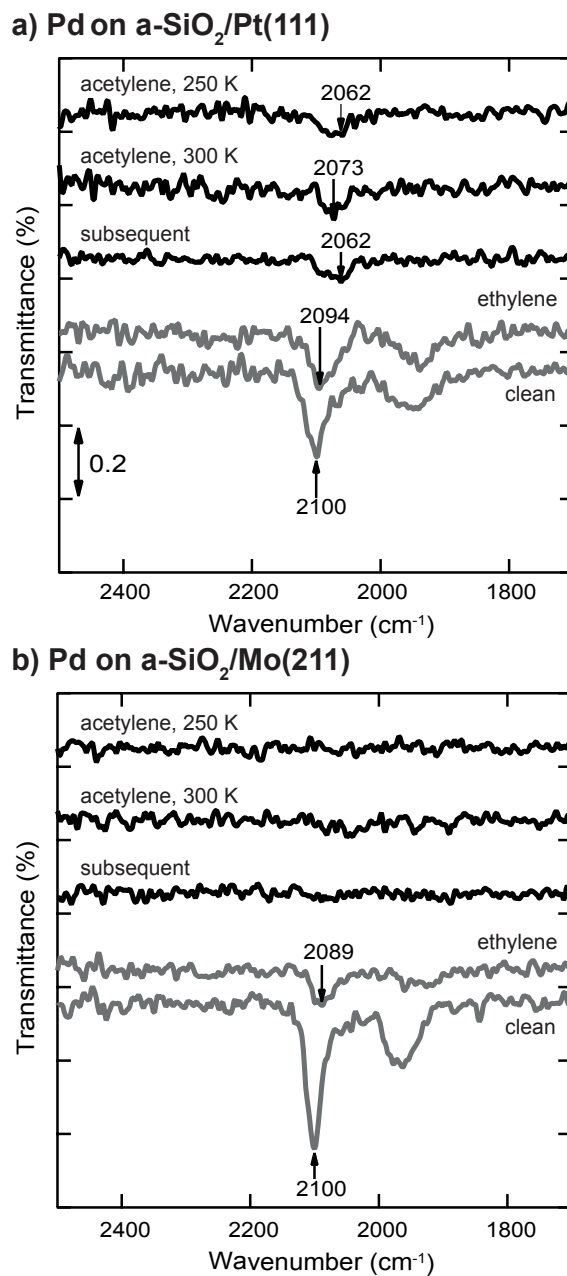


Figure 7.3: CO IRRA data of Pd nanoparticles supported on a-SiO₂/Pt(111)(a) and a-SiO₂/Mo(211)(b): CO is adsorbed at the nanoparticles at 100 K after performing the reaction at the temperature indicated. Spectra after preconditioning with ethylene at 300 K followed by acetylene hydrogenation at 250 K are denoted as subsequent. IRRA spectra of clean particles and after ethylene hydrogenation are shown for comparison (grey).

HD-exchange not observed in the desorbing products. The limited HD-exchange was attributed to a large activation barrier for the backreaction leading to accumulation of alkyl-species on the surface [242]. However, in the case of acetylene hydrogenation shown in figure 7.1, significant HD-exchange is observed for desorbing ethylene leading to ethylene-D₃ for both support systems. Consequently, the relative stability of both intermediates vinyl and ethyl on the surface has to be different. This discrepancy for acetylene was accounted for by the assumption, that the normal vinyl group is in equilibrium with a free radical state, which was used to explain the formation of E- and asym-C₂H₂D₂ isomers and might also be applicable to the exchange of hydrogen by deuterium [262].

This free radical form is also believed to play a role during oligomerization of acetylene *via* formation of adsorbed 1,3-butadiene [263], which can further polymerize or trimerize to yield benzene, although a mechanism based on coupling between acetylene and vinylidene to form a C₄ intermediate has also been experimentally verified [264]. In figure 7.1 no desorption of C₄-species are observed for clean particles on both supports. However, benzene desorption, which is the consecutive reaction product of C₄-molecules, can be detected having a maximum after several pulses in both cases. This shows, that C₄-species accumulate over the course of the experiment and remain on the surface, until the final product of cyclotrimerization benzene desorbs. Pd particles supported on a-SiO₂/Pt(111) show higher benzene yield than on a-SiO₂/Mo(211) during p-MBRS. Whether this higher yield is caused by greater catalytic production or facilitated desorption can only be clarified if the residues on the metal particles are known.

To answer this question, *post-mortem* TPR spectra shown in figure 7.2 can be used. After acetylene hydrogenation at 250 K and subsequent TPR, benzene desorption ($m/z=78$) starts at 250 K in the case of Pd particles on a-SiO₂/Pt(111), whereas the first desorption feature is located at 350 K for Pd on a-SiO₂/Mo(211). At the same time significant higher amount of benzene desorbs during TPR for Pd nanoparticles on a-SiO₂/Pt(111). The lower desorption temperature in the case of a-SiO₂/Pt(111) suggest that the production of benzene is enhanced on electron-poor particles by a lower activation barrier, whereas the higher overall yield might also be caused by residual acetylene on the surface, which undergoes cyclotrimerization upon heating. In addition to benzene ($m/z=78$), two m/z ratios of 54 and 56 are shown, which are characteristic for C₄-entities. Assuming only one desorbing C₄-molecule, e.g. 1,3-butadiene, these ratios should have identical features, which is clearly not observed in figure 7.2. A recent theoretical work evaluated C-C bond formation leading to green oil on Pd based catalysts [265]. In their vast reaction network, the authors have shown that there are several pathways for CC-coupling of low activation energies. The appearance of several desorption features and non-overlapping traces reflect the presence of several oligomerization products, which may have underwent different degrees of hydrogenation as well as HD-exchange as observed for ethylene in figure 7.1. The discussion on the absence of deuterium desorption ($m/z=4$) of Pd particles on a-SiO₂/Pt(111) after acetylene hydrogenation as well as the signal at 350 K for a-SiO₂/Mo(211) is presented in the next section, as these involve dehydrogenated C₂H_x species on the surface.

7.3.2 The Role of Dehydrogenated Species During Acetylene Hydrogenation

The hydrogenation of ethylene performed at 300 K leads to preconditioning of the Pd nanoparticles on both supports. In chapter 6 it was shown that in both cases an identical dehydrogenated overlayer C_2H_x is formed on the metal particles. This overlayer completely exchanged hydrogen by deuterium and a single desorption feature at 350 K of these species is observed during *post-mortem* TPR in figure 7.2. The amount of dehydrogenated species depends on the electron density of the particles with less electron density leading to less dehydrogenated species as observed by a smaller red-shift of the CO frequency in figure 7.3 after ethylene hydrogenation. In addition to dehydrogenation of the overlayer at 350 K, two low temperature features below 200 K are observed in figure 7.2, which might be indicative of partial carbide formation.

In the previous chapter it was shown that the formation of dehydrogenated species leads to decreased ethylene hydrogenation activity between 50 and 25 % for Pd particles on a-SiO₂/Pt(111) and a-SiO₂/Mo(211), respectively. Assuming identical active sites for acetylene and ethylene, the same decreased activity would be expected when ethylene hydrogenation is used to precondition the metal particles. However, although a small decline in activity can be observed for particles on a-SiO₂/Mo(211) in figure 7.1, this decrease is significantly smaller than expected for identical active sites. Particles on a-SiO₂/Pt(111) even show higher activity after ethylene hydrogenation than starting with clean particles. This leads to the conclusion that the active sites for acetylene hydrogenation have to be different than those for ethylene. This observation is in line with the A and E model developed by Borodziński [266, 267]. Here, at least two active sites exist on the Pd surface for acetylene (A) and ethylene (E), whereas ethylene is unable to adsorb on A sites due to geometric hindrance. On E sites, both molecules can be hydrogenated and therefore this site is made responsible for unselective overhydrogenation. This model has been developed for ambient conditions and particle sizes between 4.2 and 26.2 nm [268]. By introduction of the dehydrogenated overlayer, it is evident that this model also holds true for particles as small as twenty atoms and can be successfully mimicked under UHV conditions.

Preconditioning of electron-rich particles on a-SiO₂/Mo(211) leads to slightly decreased acetylene hydrogenation activity as can be seen in figure 7.1 b). This observation is in accordance with the C_2H_x species being stable spectator species, which effectively block active sites of the metal nanoparticles. Interestingly, the same dehydrogenation signal at 350 K is observed during *post-mortem* TPR in figure 7.2 b) for pure acetylene and ethylene hydrogenation, which indicates, that the formed dehydrogenated overlayer is partially the same for both molecules.

The analogy between acetylene and ethylene with respect to surface chemistry on clean transition metals, has also been observed for Pd single crystals [257]. However, no CO vibration can be detected in the IRRAS data of figure 7.3 b) after acetylene hydrogenation regardless of reaction temperature and pretreatment. This complete poisoning of the metal surface can be explained by reaction pathways, which are available for acetylene, but not for ethylene. The products of oligomerization, leading either to polymers or to cyclotrimerization, remain partially

on the surface and alter the availability of active sites. If these active sites are modified by stable C_2H_x spectator species on electron-rich Pd particles, the adsorption of C_4 -molecules, which would otherwise remain on the surface, is weakened leading to desorption identical to benzene as can be seen in figure 7.1 b) after ethylene hydrogenation.

The role of C_2H_x species on electron-deficient Pd particles supported on a-SiO₂/Pt(111) is more complex. After ethylene hydrogenation a single dehydrogenation feature at 350 K is observed in *post-mortem* TPR, which is identical to electron-rich particles regardless of ethylene or acetylene. However, after ethylene followed by acetylene hydrogenation this signal becomes broader in figure 7.2 a) indicating a dynamic change in the dehydrogenated overlayer. After sole acetylene hydrogenation no desorption can be detected at all, which evidences the absence of significant amounts of C_2H_x on the particles. At the same time higher desorption of ethylene as well as ethane is observed during p-MBRS in figure 7.1 a) after ethylene pretreatment leading to the conclusion that these species are replaced during acetylene hydrogenation and desorb. Especially the higher amount of ethane-D₅ after ethylene preconditioning in figure 7.1 b) supports the displacement of the spectator species, as it was shown that these species contain almost exclusively deuterium instead of hydrogen. The displacement of spectator species should lead to identical electronic structure of the supported Pd nanoparticles during acetylene hydrogenation regardless of pretreatment and is indeed observed in the CO IRRAS of figure 7.3. In both cases, after reaction starting with clean particles or after ethylene pretreatment, a single CO vibration is detected at 2062 cm⁻¹, which shifts to 2073 cm⁻¹ after increasing temperature to 300 K. This blue-shift at 300 K is caused by desorption of benzene shown in figure 7.2 a) decreasing the amount of dehydrogenated species on the metal surface. As a consequence, metal-support interactions not only determine the nature and amount of dehydrogenated species on nanoparticles, but also their relative stability. A similar effect has been observed for a platinum single crystal, where the exact nature of the dehydrogenated overlayer determined the stability in a hydrogenation atmosphere [179].

One of the key requirements for Pd based acetylene hydrogenation catalysts is to achieve high ethylene selectivity, whereas overall activity is of minor importance. So far, two key observations have been achieved in this work: first, the active sites for acetylene and ethylene are different for nanoparticles in the nm size regime. The overall activity can be steered by (de)-charging of the particles by metal-support interactions. However, by increasing reactivity also undesired byproducts are produced. Second, one major part of the dehydrogenated adlayer, C_2H_x species, can be tuned by the same interactions to be either stable in the case of electron-rich particles or to be displaced upon formation for electron-poor particles. Here, the formation of these species follows charging arguments based on the local electron density. In order to achieve higher selectivity these two factors have to be combined as shown in figure 7.4. The main aim is to minimize the amount of E sites by *in situ* blocking of unselective sites through dehydrogenation. A high electron density at the E site favours ethylene dehydrogenation leading to stable C_2H_x species as realized by a-SiO₂/Mo(211) as support system. On the other hand, the same site on electron-deficient particles leads to undesired overhydrogenation, and

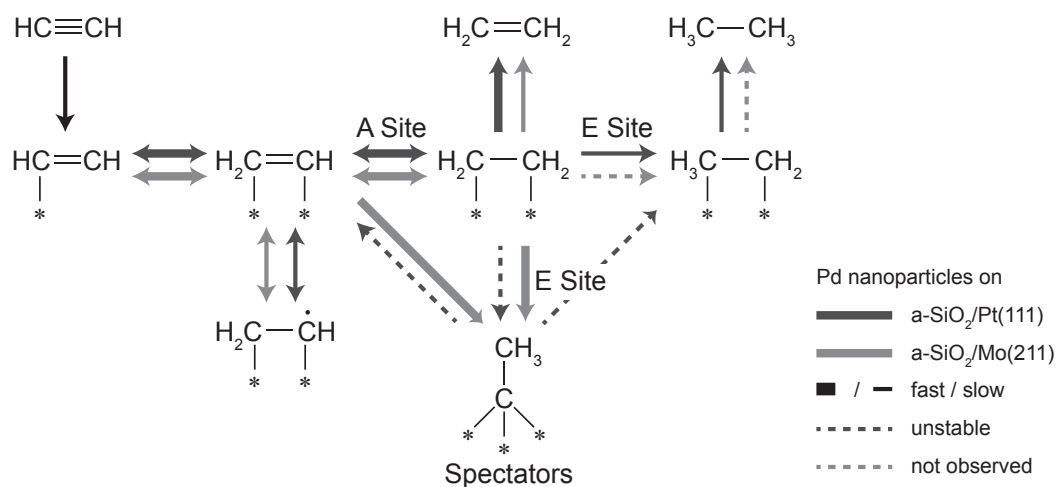


Figure 7.4: Available C₂ reaction pathways of acetylene and ethylene on supported Pd nanoparticles: a-SiO₂/Pt(111) (orange) and a-SiO₂/Mo(211) (blue). On electron-rich particles stable spectator species C₂H_x are formed either by acetylene or ethylene, whereas on electron-deficient particles the formation of these species is hindered in the case of acetylene or unstable in the case of ethylene pretreatment. Due to the formation of stable spectator on E sites, overhydrogenation to ethane can be effectively suppressed. Further reaction pathways, e.g. oligomerization, are neglected for simplicity.

even if dehydrogenated species are formed, they are unstable during acetylene hydrogenation. This self-poisoning should have a similar effect on selectivity as an external poison, e.g. lead. By increasing electron density not only unselective sites are poisoned, but also the kinetic factor should favor acetylene hydrogenation, as it was shown that the gain in acetylene activity by decreased electron density in this chapter is considerably lower than observed for ethylene hydrogenation on the same system. These considerations neglect the influence of higher hydrocarbons on E sites, which has yet to be determined.

7.4 Conclusions

The influence of metal-support interactions on catalytic properties of supported Pd nanoparticles for selective acetylene hydrogenation is provided in this work. Two different a-SiO₂ films have been prepared in order to (de-)charge identical Pd nanoparticles in the size regime of 0.9 to 1.4 nm. Here, particles supported on a-SiO₂/Pt(111) have less electron density as identical particles supported on a-SiO₂/Mo(211) caused by differences in the local work function of the support. The following main conclusions were reached:

1. Electron-poor particles have higher initial activity for acetylene hydrogenation than electron-rich particles. This metal-support induced increase in catalytic reactivity follows the trend observed for ethylene hydrogenation, although less pronounced, and can be rationalized by simple charging arguments. However, the increase in ethylene formation

- is accompanied by production of undesired byproducts, e.g. ethane, at the same time.
2. By introduction of carbonaceous deposits, it was shown that the active site for acetylene and ethylene have to be different for particles as small as twenty atoms. The occurrence of at least two distinct active sites is in line with the A and E model developed by Borodziński under applied reaction conditions and this is the first experimental evidence for their existence under UHV conditions.
 3. The metal-support interactions have direct influence on the nature of the dehydrogenated species on the metal nanoparticles. For particles with increased electron density, identical dehydrogenation features are observed between ethylene and acetylene showing their partially similar surface chemistry. In contrast to this, adsorption of acetylene leads to different surface species than ethylene for positively charged Pd nanoparticles. Pre-conditioning with species formed by ethylene and performing acetylene hydrogenation afterwards leads to replacement of initially adsorbed dehydrogenated species in contrast to spectator character typically applied in mechanistic discussions. This shows, that metal-support interactions not only determine the amount of different species on the particles, but also their relative stability. We refer to this atypical behavior as support-dictated stability of spectator species.
 4. Given the different catalytic active sites and stability of dehydrogenated species, an increase in selectivity should be accessible by increasing electron-density at the E site or reversed d-band engineering. According to the d-band model a large distance between E_F and d-band center leads to increased ethylene hydrogenation activity and the same goal can be achieved by decreased local electron density. Since this reaction is undesired in the case acetylene hydrogenation, the local electron density has to be increased at the E site leading to an *in situ* blockade of unselective sites by formation of stable spectator species. Again, this self-poisoning of unselective sites is only feasible, if the reaction takes place at different active sites as shown in the case of acetylene and ethylene in this work.

7.5 Additional Insights- Pd Nanoparticles on MgO(100)

The comparison between Pd nanoparticles supported on a-SiO₂/Pt(111) and a-SiO₂/Mo(211) in chapter 6 and 7 gave remarkable insights into the thermal chemistry of unsaturated hydrocarbons on these particles. The question arises, whether these findings can be expanded to other support materials. To this end, additional experiments were performed on the identical Pd nanoparticles supported on thick, defect-poor MgO(100), which was also used as support material for size-selected Pt clusters in chapter 4. The approach undertaken here is similar to the previous sections, where the complexity is stepwise increased from hydrogen adsorption *via* ethylene to acetylene.

The coverage dependent D₂-TPD spectra of Pd nanoparticles supported on MgO(100) are shown in figure 7.5 (a). Again, two distinct features are observed at high initial coverage, with

the high temperature signal exhibiting second order kinetics with respect to changing coverage. The high temperature signal can be attributed to surface recombination of hydrogen and the low temperature signal is caused by the presence of subsurface species in analogy to the a-SiO₂ support systems. Interestingly, the desorption temperatures between MgO(100) and a-SiO₂/Mo(211) are very similar. The similarity between the two support systems can be easily explained by the local electron density of the metal particles. As described in the previous sections, metal particles supported on a-SiO₂/Mo(211) are negatively charged due to the low local work functions. The magnesium oxide film represents a basic support and is expected to increase to the electron density of an adsorbed metal particle. Charge-transfer of electrons from the support to the Pd nanoparticles is expected in both cases, thus resulting in similar activation of hydrogen observed in the TPD spectra.

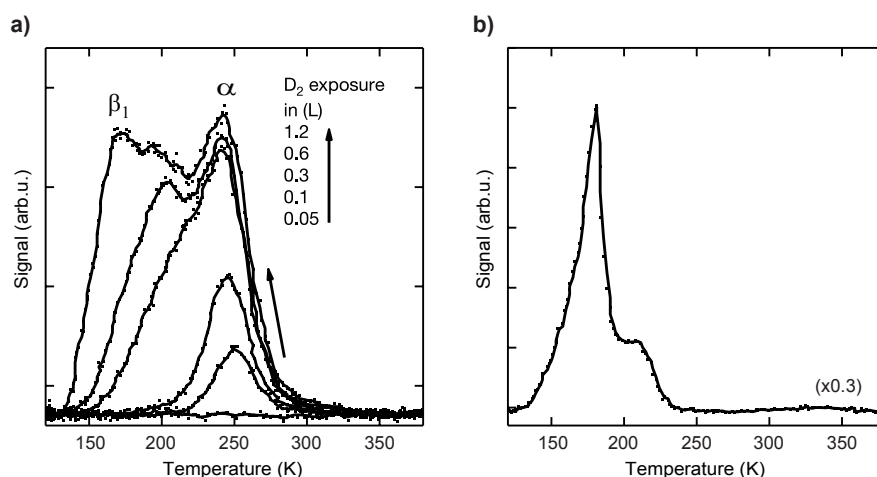


Figure 7.5: D₂-TPD spectra ($m/z = 4$) of Pd nanoparticles supported on MgO(100): (a) in dependence of coverage and (b) in the presence of excess CO. See text for experimental details and interpretation.

By comparison to literature on supported Pd nanoparticles, the existence of two distinguishable desorption features during D₂-TPD has been tentatively attributed to the presence of subsurface hydrogen species in this work. The validation of this assumption can be carried out by an elegant experiment referred to as 'hydrogen explosion' shown in figure 7.5 (b): first, 1.2 L of D₂ are dosed onto the supported Pd nanoparticles at 100 K leading to full saturation. Afterwards 2 L of CO are dosed, which displaces deuterium surface species and a TPD spectrum is recorded. During TPD, CO adsorbed on the surface of the Pd nanoparticles hinders the diffusion and surface recombination of subsurface hydrogen species. As soon as CO desorbs, a rapid decay of the Pd hydride takes place and a sharp increase in hydrogen desorption is observed, as can be seen in figure 7.5 (b). The 'hydrogen explosion' is caused by a finite size effect of the Pd nanoparticles [269] and serves as a confirmation of the subsurface character of the involved hydrogen species.

The results of the isothermal ethylene hydrogenation using the standard p-MBRS experi-

ments are shown in figure 7.6. The reaction was performed at 300 K and only the stoichiometric reaction product $C_2H_4D_2$ is presented as it was shown in the previous sections, that HD-exchange is negligible under these reaction conditions for ethylene hydrogenation. A decrease of approximately 50 % is observed over the course of the experiment due to the formation of dehydrogenated species on the metal surface. The TOF numbers obtained for Pd nanoparticles supported on MgO(100) resemble those for particles on α -SiO₂/Mo(211), highlighting the similarity between the two support systems.

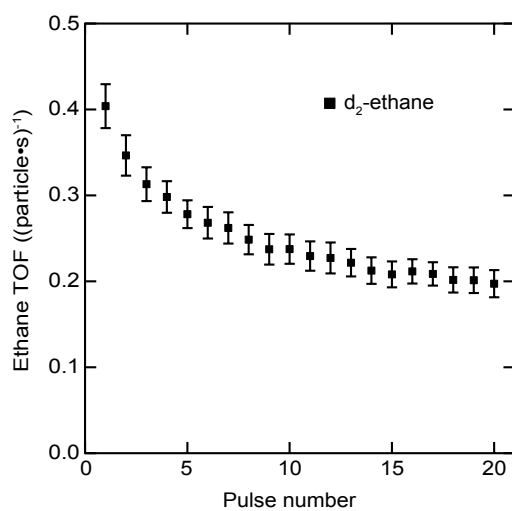


Figure 7.6: Activity results for ethylene hydrogenation of Pd nanoparticles supported on MgO(100) given as ethane TOF per Pd particle in progression of single ethylene pulses at 300 K.

The isothermal acetylene hydrogenation at 250 K was performed for initially clean Pd nanoparticles and after ethylene hydrogenation at 300 K. The results are summarized in figure 7.7 for as deposited nanoparticles (a) and after ethylene hydrogenation (b, poisoned). The clean Pd particles supported on MgO(100) show similar behavior to identical particles on α -SiO₂/Mo(211) as support material during acetylene hydrogenation. An extensive HD-exchange is observed for desorbing ethylene molecules and no overhydrogenation to ethane is detected. A maximum in benzene desorption is observed after several pulses, whereas C₄-molecules necessary for cyclotrimerization remain on the metal surface. The formation of benzene ($m/z=78$) was additionally cross-checked by the m/z ratios of 79 and 80 in order to evaluate the incorporation of deuterium during cyclotrimerization. The benzene TOFs of these masses as a function of pulse number followed the one of $m/z=78$, which excludes the possibility of preferential oligomerization *prior* to HD-exchange.

The preconditioning of the Pd nanoparticles using ethylene hydrogenation leads to the formation of C₂H_x species on the metal particles [138]. These species decrease the activity for acetylene hydrogenation on Pd nanoparticles supported on MgO(100) as can be seen in figure 7.7 (b). At the same time, the significant HD-exchange observed for initially clean particles

almost completely vanished after pretreatment. Also the formation of benzene decreases after preconditioning. Again, no formation of ethane is detected, although the background noise of $C_2H_2D_4$ increased. It was supposed in the previous section that the local electron density not only determines the nature of the dehydrogenated overlayer, but also the stability of the latter with high electron-density leading to more stable dehydrogenated species on the metal surface. Expanding this trend, it can be proposed that the basic support material MgO induces the formation of highly stable C_2H_x species on the surface. Due to their stability, they do not contribute to the overall hydrogenation activity and merely block active sites for hydrogenation. This would not only explain the diminished activity, but also the absence of HD-exchange. The dehydrogenated species can also be called pure spectator species in this regard as they resemble the behavior of the latter commonly proposed in literature. However, it was shown in this work, that the assumption of pure spectator behavior is not always justified for supported Pd nanoparticles.

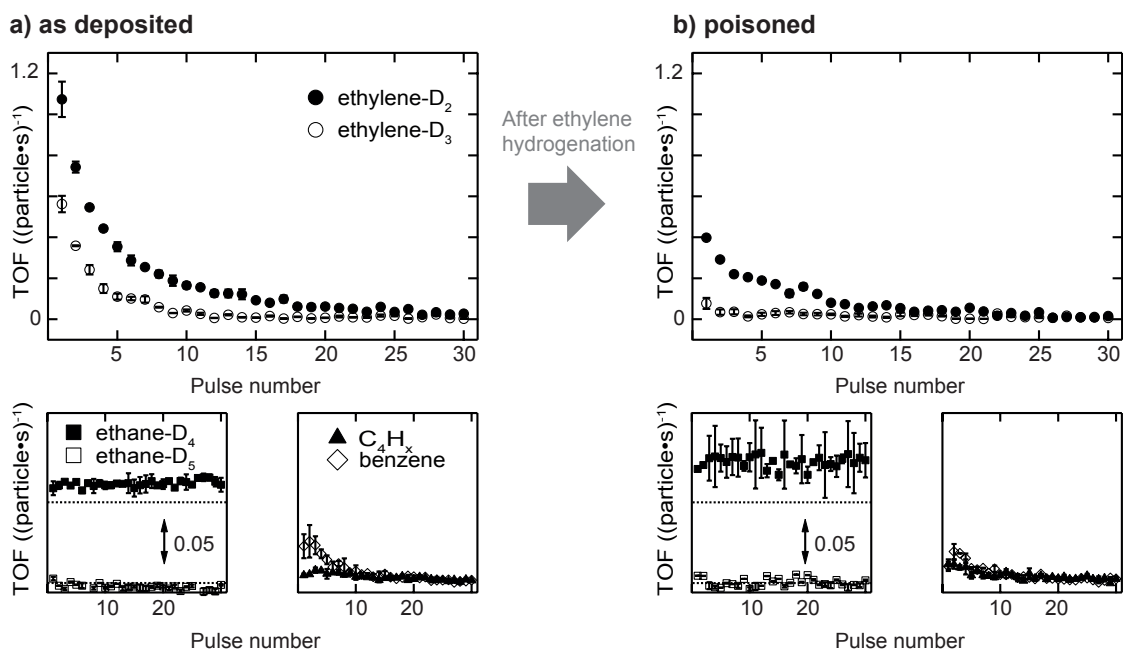


Figure 7.7: Activity results for acetylene hydrogenation catalyzed by clean (a) and poisoned (b) Pd nanoparticles supported on MgO(100). The reaction is performed at 250 K using a p-MBRS technique and the TOFs for different reaction products are given as a function of pulse number. The three subfigures are devoted to ethylene as the main product, ethane and oligomerization. Note that ethane- d_4 exhibits an offset in ethane subfigures indicated by the dotted line for better visibility.

The surface species have been further characterized by CO IRRAS (a) and *post-mortem* TPR (b) shown in figure 7.8. The frequency of linear, on top CO species is detected at 2098 cm^{-1} for clean particles. Furthermore, bridge bonded species at 1970 cm^{-1} can be detected. No CO stretch is found after acetylene hydrogenation regardless of reaction temperature and pretreatment analogous to a-SiO₂/Mo(211). This already indicates, that the complete metal surface is covered

by various carbonaceous species.

These species can be further specified using *post-mortem* TPR displayed in figure 7.8 (b). The desorption of all higher hydrocarbons as the products of oligomerization starts at the former reaction temperature of 250 K. This supports the theory, that oligomerization takes place at low temperatures and the products of this process remain on the surface. Here, the desorption signal of benzene is significantly lower than the one of Pd nanoparticles supported on α -SiO₂/Pt(111) in accordance with the results obtained for isothermal reaction conditions. Two broad signals for $m/z=4$ at 330 K and 580 K are characteristic for dehydrogenation processes, which were qualitatively observed also for particles on α -SiO₂/Mo(211). In summary, the surface chemistry of hydrogen, ethylene, and acetylene on Pd nanoparticles supported on MgO(100) is indeed similar to the one observed for α -SiO₂/Mo(211) as support material. From a chemical point of view, this observation makes sense as the support is not directly involved in the reactions, but influences the supported metal particles by transfer of electron density. Whether the increased electron density of the metal particles is caused by the magnesium oxide as an alkaline support or by the low local work functions of the α -SiO₂/Mo(211) systems seems to play only a minor role.

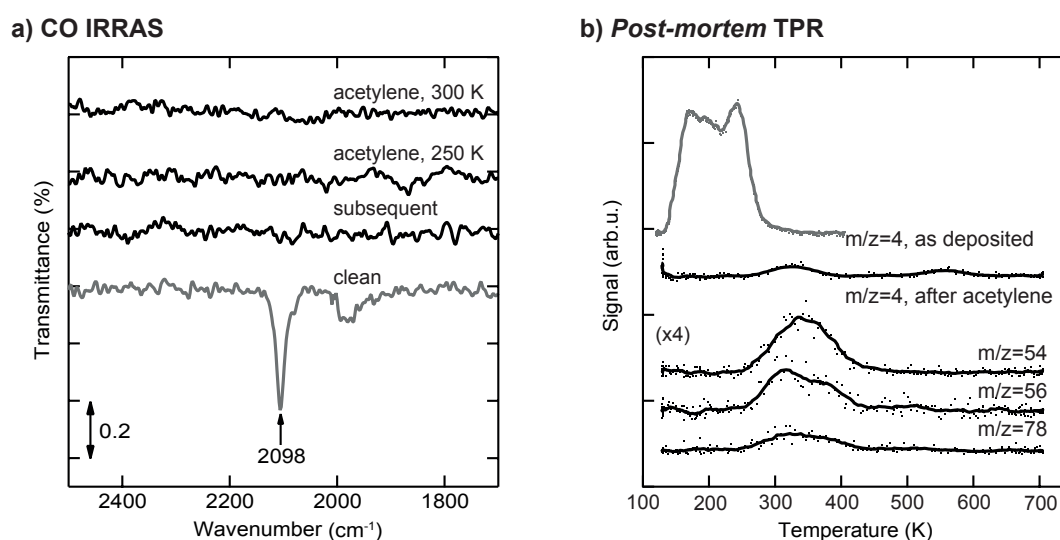


Figure 7.8: CO IRRAS data (a) and *post-mortem* TPR spectra (b) after acetylene hydrogenation on Pd nanoparticles supported on MgO(100). CO is adsorbed on the nanoparticles at 100 K after performing the reaction at the temperature indicated. The spectrum after preconditioning with ethylene at 300 K followed by acetylene hydrogenation at 250 K is denoted as subsequent and the IRRA spectrum of clean particles is shown for comparison (grey). For *post-mortem* TPR, additional 20 L of D₂ are dosed at 100 K. The D₂-TPD of clean/as deposited Pd nanoparticles is given in grey.

CONCLUSION AND OUTLOOK

In the preceding chapters, the surface chemistry of unsaturated hydrocarbons on late transition metals under UHV conditions has been presented. Diverse model systems have been used to illustrate different aspects of hydrocarbon structure, physical state of the metal, and the influence of the support material on the latter in the case of either size-selected metal clusters or nanoparticles. Besides interactions between hydrocarbon and metal, the main focus of attention was the molecular mechanisms of selective hydrogenation reactions.

As a model system for long-chained alkynes, the thermal surface chemistry of hexynes was first investigated on Pt(111) by means of combined experimental techniques. Here, a novel reaction has been observed for 1- and 3-hexyne: the dehydrocyclization to benzene, which has also been experimentally verified to occur for the according alkenes. Interestingly, this reaction involves a CC-bond formation step, which is hardly observed under UHV conditions in general and in particular for platinum. Although dehydrogenations have been extensively researched in the early stages of surface science, these studies almost exclusively dealt with the reaction sequence of cyclo-hexane, -hexene, -diene, to benzene on platinum surfaces. Consequently, the number of CC-bonds remained unchanged in these studies, and the thermal chemistry involved only dehydrogenation steps. In the present work, the additional formation of the CC-bond was proposed to proceed after dehydrogenation at higher temperatures. This finding expands our understanding of possible reaction pathways of C_6 molecules and the formation of dehydrogenated overlayers.

The surface chemistry of 3-hexyne was further elucidated on supported, size-selected Pt clusters with regard to selective hydrogenation. Several reaction pathways have been detected using isotopically labeled TPR experiments, each containing size-sensitive behavior. Here, the dehydrocyclization to benzene was shown to occur for all cluster sizes down to sizes of three atoms. Single atoms are not capable of this reaction pathway. A small atomic window is found for Pt_9 , where hydrogenation of alkynes occurs in TPR experiments in contrast to alkene

hydrogenation. The difference in activation barriers should result in enhanced selectivity. Based on previous results on these cluster sizes, it can be speculated, that the high heat of adsorption, which is close to intermetallic binding energies of the cluster, leads to significant changes in cluster morphology. This adsorbate-induced fluxionality may facilitate triple bond hydrogenation by lowering the activation barrier of D_2 dissociation, as HD-exchange on clean Pt_9 clusters is hampered by high activation barriers in contrast to larger cluster sizes. However, support of this hypothesis by theoretical calculations is impeded by the presence of dehydrogenated species, whose nature and amount have yet to be determined.

The catalytic activity of size-selected clusters is not only controlled by adsorbates, but also by charge-transfer of electrons from or to the support material. In the case of isotropic support materials, e.g. $MgO(100)$, the description of this effect is rather trivial due to the periodicity of the support, but becomes increasingly challenging for anisotropic and amorphous structures such as $\alpha-SiO_2$ described in this work. So far, descriptions of charge-transfer phenomena were performed for single model systems lacking a universal physical quantity to predict *a priori* (de)-charging of supported metal particles. The local work function of the support material might represent a suitable physical descriptor of such systems.

To this end, we have synthesized thin $\alpha-SiO_2$ films on $Pt(111)$ and $Mo(211)$, which were used as support material for size-selected Pt clusters. Supported by *first principles* calculations, these films exhibit a variety of adsorption sites. The charge-transfer between Pt_{13} clusters and single adsorption sites was shown to be directly correlated to the local work function of the support resulting in modified local electron densities in the clusters. This finding was experimentally verified indirectly by isothermal ethylene hydrogenation, where negative charging of the clusters led to significant deactivation after increased reaction temperature by formation of dehydrogenated species, whereas positively charged clusters retained most of their catalytic performance as predicted by this local work function model. The attenuation of undesired coke formation by nanoengineering of the support demonstrates, that the local work function is not only of theoretical, but also of practical relevance for the rational design of catalysts.

Besides size-selected clusters in the sub-nm size regime, the control over electron transfer can also be applied to steer catalytic activity of identical, supported Pd nanoparticles, where positive charging stabilizes hydrogen species in comparison to negatively charged particles. This finding is of general importance for all reactions involving atomic hydrogen species such as (de)-hydrogenation and hydrogenolysis. Interestingly, the performed experiments reveal a discussion in the literature in a different light: the question, whether the heat of adsorption of hydrogen species on Pd nanoparticles increases as the size is decreased or *vice versa*. The results gained give clear evidence, that the answer might not be biunique as it depends not only on exact particle size, but also on their charge state determined by metal-support interactions.

The manipulation of electron densities of supported Pd nanoparticles was applied to the hydrogenation of ethylene and acetylene. A significant enhancement of catalytic activity for ethylene hydrogenation was observed for positively charged particles in general accordance with previously reported models and attributed to lowered activation barriers. The dehydrogenated

overlayer formed upon reaction was shown to have undergone a complete substitution of hydrogen by deuterium, which contradicts the commonly believed formation mechanism. Given this HD-exchange, it seems likely, that the overlayer acts as a hydrogen reservoir to some extent, a proposal also made by other researchers in the field.

The complex role of dehydrogenated species is further underlined during selective hydrogenation of acetylene. For electron-rich particles, the same C_2H_x surface species are partially formed regardless of acetylene and ethylene, whereas these are not observed for electron-poor particles, which favor hydrogenation, oligomerization and cyclotrimerization to benzene. Even when C_2H_x species are introduced *a priori*, they are not stable on positively charged Pd particles and are replaced over the course of the reaction. Consequently, these species are by no means pure spectators, which block active surface sites.

The spectator species have also been used to shed light on the active sites required for acetylene and ethylene hydrogenation on supported Pd nanoparticles. It was unequivocally shown, that these sites differ for both molecules in accordance with the A and E model proposed for larger Pd particles under ambient conditions. Verification of such sites under idealized conditions demonstrates the capability of model catalysis to successfully mimic real world catalysts under well defined conditions despite the so-called pressure and complexity gaps. Indeed, the differentiation between two distinct active sites for hydrocarbon conversion under UHV conditions has so far been elusive to the best of the author's knowledge.

Achieving both, high activity and selectivity, is a challenging task and it seems like only a trade off is achievable for pure metal particles: Electron-poor Pd nanoparticles show higher initial hydrogenation activity. However, the increased activity is accompanied by the formation of undesired byproducts and overhydrogenation to ethane, whose detection is one of the rare examples for consecutive transformations of the same functional group under UHV conditions. As the active sites for ethylene and acetylene hydrogenation are different, it can be proposed, that the E site should be electron rich in order to achieve high selectivity. This leads to poisoning of these sites by formation of dehydrogenated species, whereas sites for acetylene remain unaffected. Again, such statements are only possible by variation of single reaction parameters enabled by model catalysis.

In summary, this work has shed light on different aspects of hydrocarbon chemistry on late transition metals under UHV conditions and the question rises of future perspectives. It was already stated in the experimental chapter, that the relocation of the laboratory required significant experimental changes. This chance was used to implement modifications and expansions in the new chamber and the novel layout of the setup is schematically shown in figure 8.1. Division of the analysis chamber into several subchambers separated by gate valves allows for rapid repairing. Connecting the transfer chamber directly to the analysis chamber renders the possibility to repeatedly transfer samples between UHV and ambient or to prepare samples for ambient experiments without the time-consuming effort to redirect the cluster beam.

The most important aspect from a scientific point of view is the possibility to perform X-ray photoelectron spectroscopy (XPS). Along with MIES/UPS, the complete electronic structure will

become accessible. The benefits gained by XPS for the investigations of hydrocarbons on metal nanoparticles are manifold: the electronic properties of the metal particles can be characterized before and after reaction. In addition, the amount and nature of dehydrogenated carbonaceous species can be monitored. Access to this information will hopefully enrich our understanding of the factors determining (sub)-surface processes.

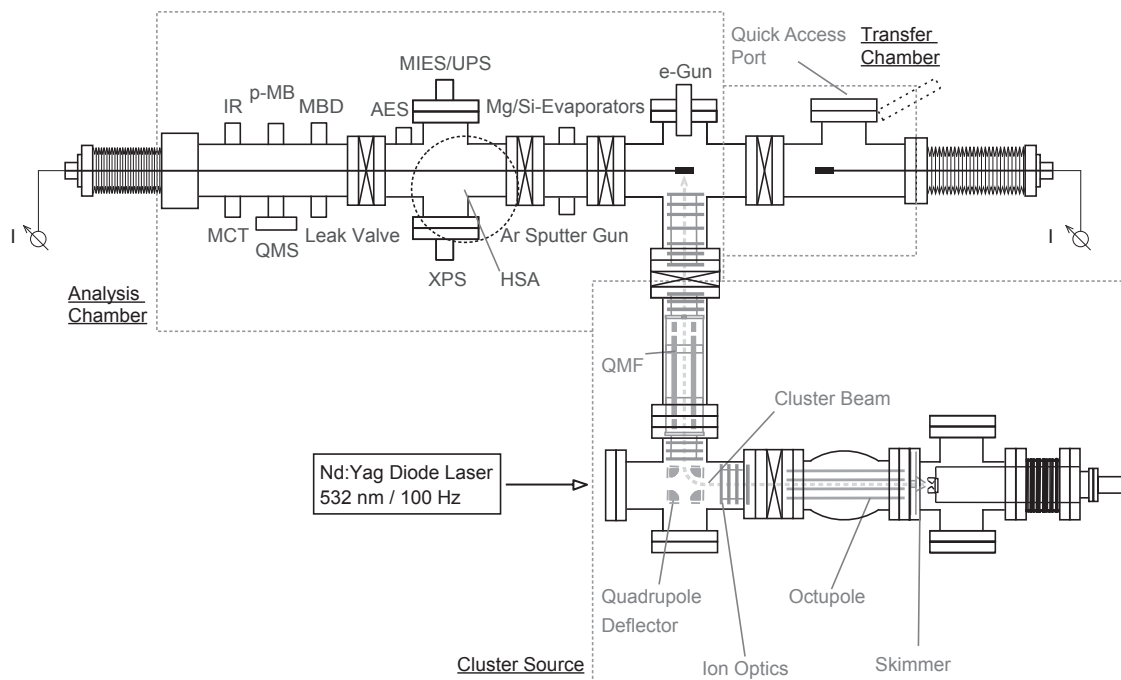


Figure 8.1: Schematic of the newly installed experimental setup: Improvements in chamber design and layout facilitate maintenance, whereas implementation of additional techniques, such as XPS, boosts scientific possibilities.

The exact reactions, materials, and topics of future investigations are limited only by the imagination of the next generation of researchers. Therefore, only brief suggestions are given here, of which the author thinks are worth pursuing. As was shown in this work, the chemistry of unsaturated hydrocarbons on late transition metals is characterized by several subtleties, whose characterization and understanding are required to get the complete picture of factors determining overall catalytic performance.

The activity and selectivity of Pd nanoparticles for hydrogenation reactions has often been discussed to be steered by the availability of subsurface hydrogen species. The experiments performed in this work demonstrate the existence of such species even for particles as small as twenty atoms. What happens, if these particles reach the lowest bottom of size, that is the non-scalable size regime? How many atoms are actually needed for 'hydride' formation and is the transition fluent or caused by addition of a single atom? Are these species similar to the ones observed for larger particles and what is their influence on catalytic performance?

For pure academic rather than industrial interest, one could also replace the metal itself by e.g. gold. It was shown by other researchers, that small Au nanoparticles exhibit excellent selectivities for alkyne hydrogenation due to negligible interactions between alkene and metal. Here, the whole reaction network is changed to such an extent, that the rate determining step of alkyne hydrogenation is replaced by dissociation of hydrogen. A single cluster size capable of effective hydrogen dissociation might turn out to be an extremely efficient hydrogenation catalyst in terms of combined activity and selectivity.

An alternative issue of selectivity is the presence of different functional groups within one target molecule. Instead of the saturation degree of an initial triple bond, the reaction of molecules such as acrolein and crotonaldehyde centers around the hydrogenation of CC *versus* CO double bonds. The control over chemoselectivity represents one of the major hurdles for future catalysis.

The long-term goal of supported, size-selected metal clusters used for catalysis purposes has to be a unifying theory. So far, two major concepts have been developed to describe their performance, fluxionality and the local electron density, which can be specified by oxidation state and charge-transfer from or to the support. However, the link between these two ideas is still missing. A concept including both would decisively broaden our conception of cluster catalysis. Considerable experimental and theoretical advancements are necessary to finally achieve this goal, but the experiences gained along the way might have an essential impact on the way we understand catalytic phenomena.



APPENDIX

The following chapter was published as a supporting information in the *Journal of Physical Chemistry C*. Reprinted with permission from *J. Phys. Chem. C* 122, 8, 2018, 4428-4436. Copyright 2018 American Chemical Society.

Theoretical calculation of molecular orbitals

To qualitatively support the experimental assignments in the UPS and MIES spectra, quantum chemical calculations are performed for the isolated molecules using the program Molpro 2006.1 [270]. To estimate the involved ionization potentials, initial and final state energies are computed. The initial state energies directly correspond to the molecular orbital energies of a Hartree-Fock (HF) calculation after Koopmans theorem. The final state energies correspond to excited electronic state energies of the cation referenced to the ground state energy of the neutral molecule. The latter is hereby representative of the relaxed electronic structure after ionization of different valence orbitals. A true ionization potential can be expected to lie between the initial and final state.

The gas phase minimum energy structures are optimized on Møller-Plesset perturbation theory (MP2) level and electronic structure calculations for ground state molecular orbitals are performed on HF level. Excited state energies are obtained via complete active space self-consistent field (CASSCF) with multireference perturbation theory (CASPT2). All levels of theory employ a cc-pVDZ basis set. The 10 lowest excited states are computed for the cation using a state averaged SA(10)-CASSCF calculation. The active space is chosen to include all orbitals with a contribution larger than 2% for the excited states. For 3-hexyne follows a (17,11) and a (18,11) active space for the cation and neutral molecule and for 1-hexyne a (19,12) and a (20,12) active space for the cation and the neutral molecule, respectively. The large number of occupied orbitals in the active space results from the cationic excited states including ionization

of low lying molecular orbitals (MOs) (c.f. table A.1 and A.2).

As seen in table A.1 and A.2, the rather crude Koopman approximation and the high-level CASPT2 calculations deviate quantitatively. Although most of the core-level ionizations are also found in the CASPT2 calculations, in the case of 3-hexyne also mixed ionization-excitation configurations are seen for the two highest excited states. Note that the declaration of the MOs changes partially due to a different energetic ranking in the HF and SA(10)-CASSCF formalism. Nevertheless, both methods show clearly that the photoelectron peaks around 10 eV correspond to $\pi_{C=C}$ orbitals while peaks at higher energies correspond to σ orbitals.

Table A.1: Theoretical photoelectron peak assignment for a gas phase spectrum of 3-hexyne, comparing molecular HF orbital energies ($-\epsilon$), corresponding to an initial state, with ionization potentials (IP) on SA(10)-CASPT2 level corresponding to a final state after a photoelectron transition. Given is the respective peak energy, the MO declaration or predominant electronic configuration as well as the MO character.

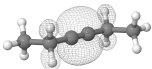
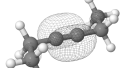
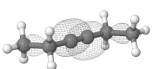
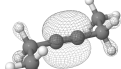
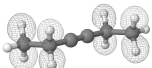
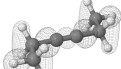

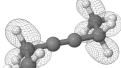

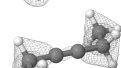

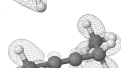
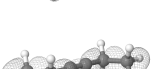
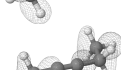
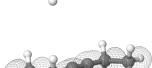
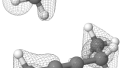
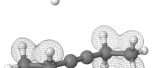
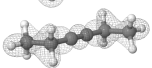
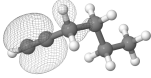
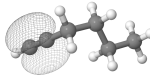
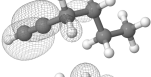
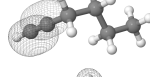
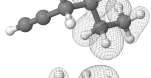
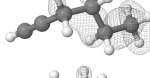
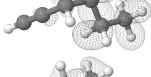
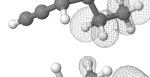
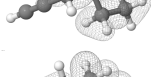
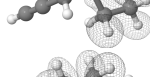
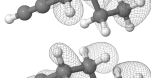
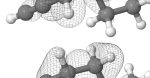
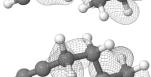
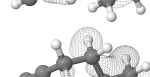
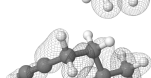
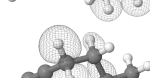
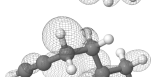
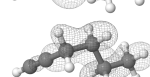

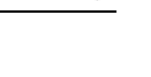
$-\epsilon / \text{eV}$	MO		IP / eV	MO	
9.55392	23a ₁ ($\pi_{C=C}$)		9.06601	23a ₁ ¹ ($\pi_{C=C}$)	
9.58658	22a ₁ ($\pi_{C=C}$)		9.11140	22a ₁ ¹ ($\pi_{C=C}$)	
13.56493	21a ₁ (σ_{C-H})		12.4764	16a ₁ ¹ ($\sigma_{C-H}, \sigma_{C-C}$)	
13.77713	20a ₁ (σ_{C-H})		12.3812	18a ₁ ¹ (σ_{C-H})	
13.85060	19a ₁ ($\sigma_{C-H}, \sigma_{C-C}$)		12.7125	19a ₁ ¹ ($\sigma_{C-H}, \sigma_{C-C}$)	
14.07918	18a ₁ ($\sigma_{C-H}, \sigma_{C-C}$)		12.6026	20a ₁ ¹ (σ_{C-H})	
14.42476	17a ₁ (σ_{C-C})		12.7326	17a ₁ ¹ ($\sigma_{C-H}, \sigma_{C-C}$)	
14.99892	16a ₁ (σ_{C-C})		13.2778	21a ₁ ¹ ($\sigma_{C-H}, \sigma_{C-C}$)	
16.63705	15a ₁ (σ_{C-H})		15.1274	22a ₁ ¹ 23a ₁ ¹ 25 a ₁ ¹	
16.83569	14a ₁ ($\sigma_{C-H}, \sigma_{C-C}$)		15.1662	22a ₁ ¹ 23a ₁ ¹ 24a ₁ ¹	

Table A.2: Theoretical photoelectron peak assignment for a gas phase spectrum of 1-hexyne, comparing molecular HF orbital energies ($-\varepsilon$), corresponding to an initial state, with ionization potentials (IP) on SA(10)-CASPT2 level corresponding to a final state after a photoelectron transition. Given is the respective peak energy, the MO declaration or predominant electronic configuration as well as the MO character.

$-\varepsilon / \text{eV}$	MO		IP / eV	MO	
-10.12264	23a ₁ ($\pi_{C=C}$)		9.75933	23a ₁ ($\pi_{C=C}$)	
-10.14985	22a ₁ ($\pi_{C=C}$)		9.85831	22a ₁ ($\pi_{C=C}$)	
-12.70228	21a ₁ (σ_{C-H})		11.4161	15a ₁ ($\sigma_{C-H}, \sigma_{C-C}$)	
-12.79208	20a ₁ ($\sigma_{C-H}, \sigma_{C-C}$)		11.6109	18a ₁ (σ_{C-H})	
-13.10773	19a ₁ ($\sigma_{C-H}, \sigma_{C-C}$)		11.7072	17a ₁ ($\sigma_{C-H}, \sigma_{C-C}$)	
-13.99482	18a ₁ (σ_{C-H})		12.6506	19a ₁ ($\sigma_{C-H}, \sigma_{C-C}$)	
-14.60708	17a ₁ ($\sigma_{C-H}, \sigma_{C-C}$)		13.0852	21a ₁ ($\sigma_{C-H}, \sigma_{C-C}$)	
-15.96221	16a ₁ ($\sigma_{C-H}, \sigma_{C-C}$)		14.3757	16a ₁ (σ_{C-H})	
-16.21255	15a ₁ ($\sigma_{C-H}, \sigma_{C-C}$)		14.4992	20a ₁ ($\sigma_{C-H}, \sigma_{C-C}$)	
-16.62344	14a ₁ ($\sigma_{C-H}, \sigma_{C-C}$)		14.8457	14a ₁ ($\sigma_{C-H}, \sigma_{C-C}$)	

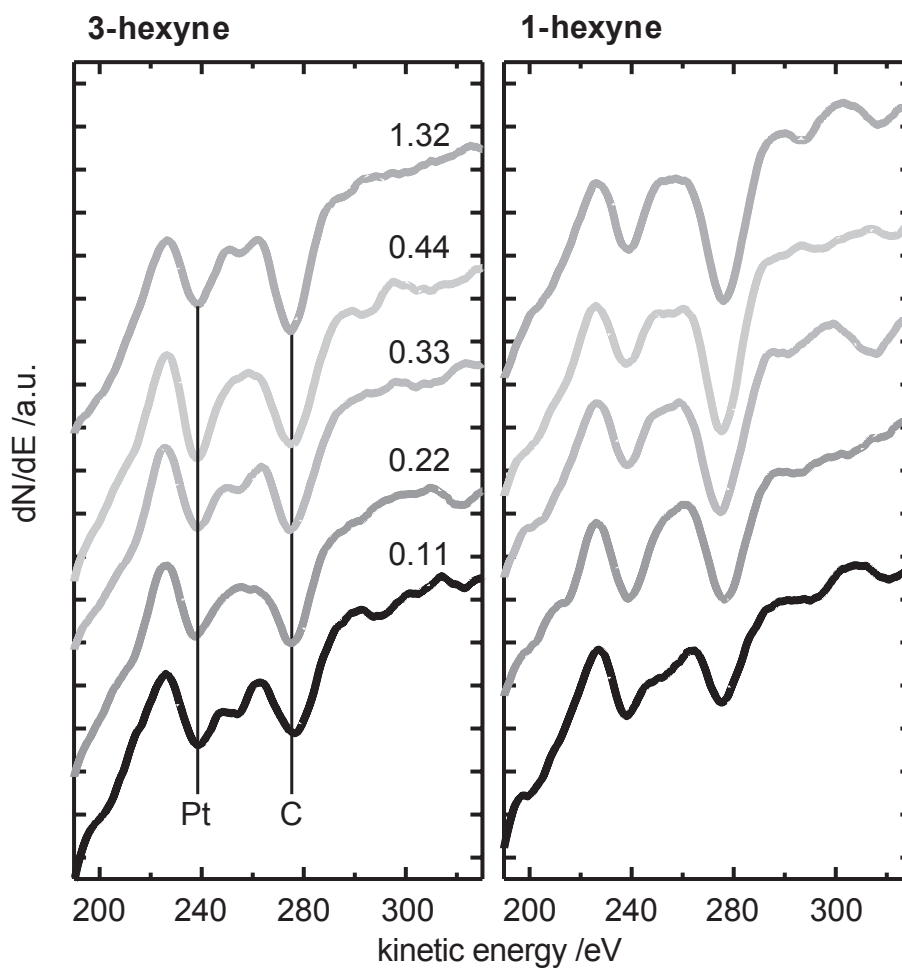


Figure A.1: Auger spectra for 3- and 1-hexyne on Pt(111) after TPD to 800 K. The ratio between C (275 eV) and Pt (241 eV) is used to calculate the amount of carbon residues on the surface. The calculation is performed according to reference [137] and takes two effects into account: (1) screening of the Pt AES signal by surface carbon atoms and (2) contribution from Pt layers in the bulk.

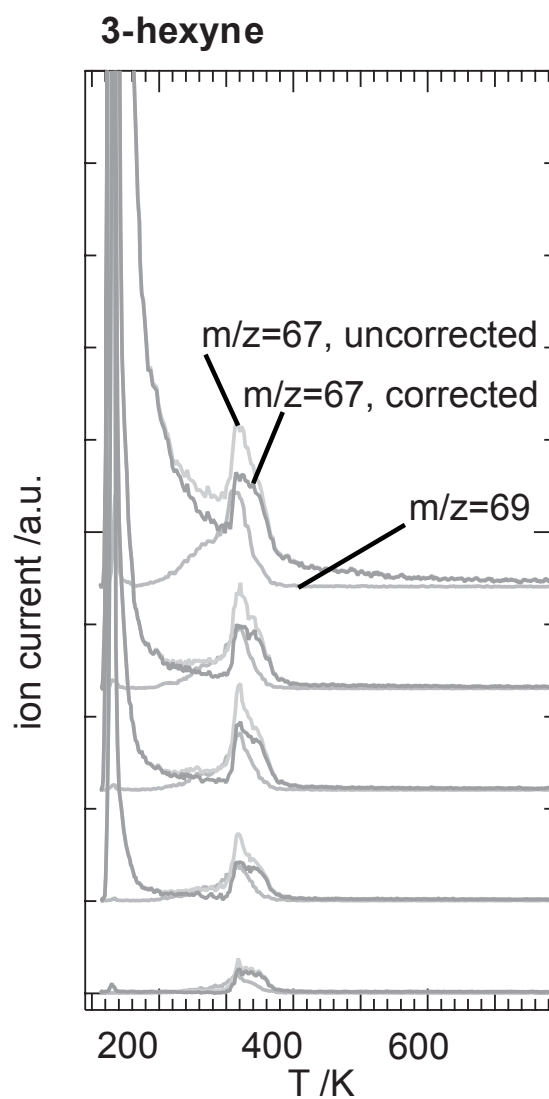


Figure A.2: Background correction for the desorption of 3-hexyne: The cracking pattern of hexene ($m/z = 69$) was determined *in situ* and the obtained sensitivity factor is used to subtract the contribution of $m/z = 69$ (hexene) from $m/z = 67$ (hexyne) resulting in the background corrected traces, which were used to determine peak areas.

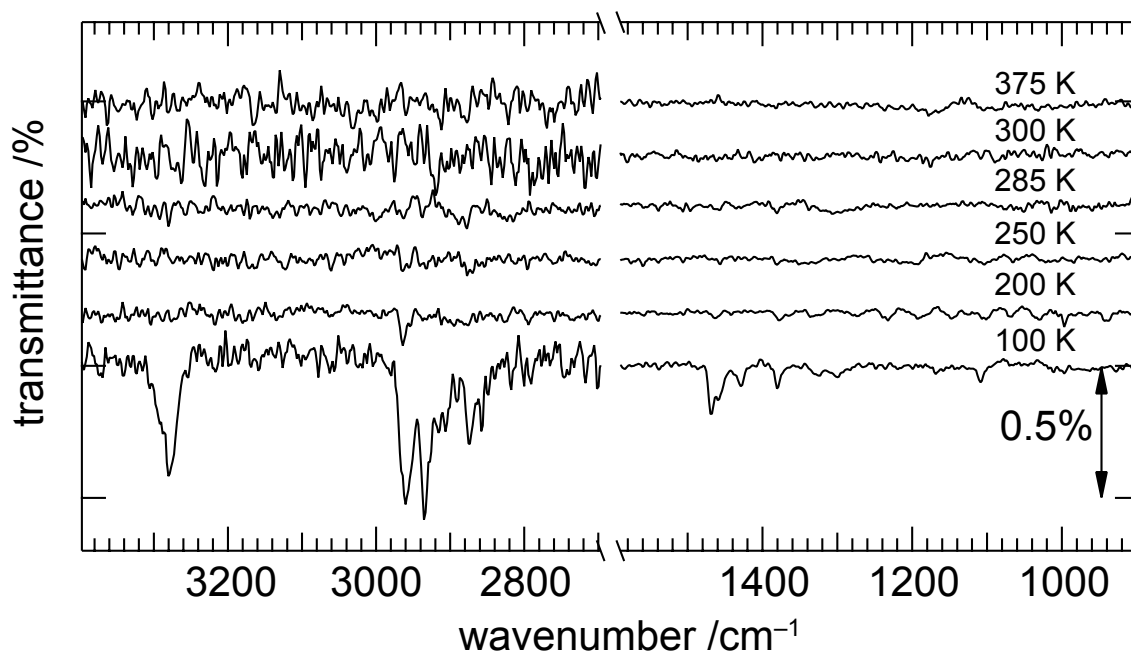


Figure A.3: Temperature dependent IRRA spectra of 1-hexyne on Pt(111): 7 L of 1-hexyne were dosed either at 200 or 250 K. After dosage at 250 K the sample temperature was stepwise increased to 285, 300 and 375 K. All spectra were recorded at the dosage temperature. Adsorption at temperatures higher than 100 K leads to disappearance of all signals indicating that dehydrogenation takes place at low temperatures in accordance with the mechanism proposed for dehydrocyclization.



RightsLink®

Home

Create Account

Help



ACS Publications
Most Trusted. Most Cited. Most Read.

Title: Surface Chemistry of 1- and 3-Hexyne on Pt(111): Desorption, Decomposition, and Dehydrocyclization
Author: M. D. Rötzer, M. Krause, A. S. Crampton, et al
Publication: The Journal of Physical Chemistry C
Publisher: American Chemical Society
Date: Mar 1, 2018
Copyright © 2018, American Chemical Society

LOGIN

If you're a [copyright.com](#) user, you can login to RightsLink using your [copyright.com](#) credentials. Already a RightsLink user or want to [learn more?](#)

PERMISSION/LICENSE IS GRANTED FOR YOUR ORDER AT NO CHARGE

This type of permission/license, instead of the standard Terms & Conditions, is sent to you because no fee is being charged for your order. Please note the following:

- Permission is granted for your request in both print and electronic formats, and translations.
- If figures and/or tables were requested, they may be adapted or used in part.
- Please print this page for your records and send a copy of it to your publisher/graduate school.
- Appropriate credit for the requested material should be given as follows: "Reprinted (adapted) with permission from (COMPLETE REFERENCE CITATION). Copyright (YEAR) American Chemical Society." Insert appropriate information in place of the capitalized words.
- One-time permission is granted only for the use specified in your request. No additional uses are granted (such as derivative works or other editions). For any other uses, please submit a new request.

BACK

CLOSE WINDOW

Copyright © 2018 [Copyright Clearance Center, Inc.](#) All Rights Reserved. [Privacy statement](#). [Terms and Conditions](#). Comments? We would like to hear from you. E-mail us at customer@copyright.com

Figure A.4: Publishing agreement for the Journal of Physical Chemistry C.

BIBLIOGRAPHY

- [1] Ostwald, W. *Physikalische Zeitschrift* **1901**, *3*, 313.
- [2] Ertl, G.; Knözinger, H.; Weitkamp, J. *Handbook of Heterogeneous Catalysis*; Wiley-VCH, 1997.
- [3] Chorkendorff, I.; Niemantsverdriet, J. *Concepts of Modern Catalysis and Kinetics*; Wiley, 2017.
- [4] Reschetilowski, W. *Einführung in die Heterogene Katalyse*; Springer Berlin Heidelberg, 2015.
- [5] Friend, C. M.; Xu, B. *Accounts of Chemical Research* **2017**, *50*, 517–521.
- [6] DECHEMA,; ICCA,; IEA, Technology Roadmap: Energy and GHG Reductions in the Chemical Industry via Catalytic Processes. 2013.
- [7] Lanzafame, P.; Perathoner, S.; Centi, G.; Gross, S.; Hensen, E. J. M. *Catalysis Science & Technology* **2017**, *7*, 5182–5194.
- [8] Crespo-Quesada, M.; Cárdenas-Lizana, F.; Dessimoz, A.-L.; Kiwi-Minsker, L. *ACS Catalysis* **2012**, *2*, 1773–1786.
- [9] Fouilloux, P. *Applied Catalysis* **1983**, *8*, 1–42.
- [10] Zaera, F. *Journal of Catalysis* **1990**, *121*, 318–326.
- [11] Zaera, F.; Hall, R. B. *Surface Science* **1987**, *180*, 1–18.
- [12] Zaera, F. *Topics in Catalysis* **2005**, *34*, 129–141.
- [13] Wasylenko, W.; Frei, H. *The Journal of Physical Chemistry B* **2005**, *109*, 16873–16878.
- [14] Horiuti, I.; Polanyi, M. *Transactions of the Faraday Society* **1934**, *30*, 1164–1172.
- [15] Ebrahimi, M.; Simonovis, J. P.; Zaera, F. *The Journal of Physical Chemistry Letters* **2014**, *5*, 2121–2125.
- [16] Dong, Y.; Ebrahimi, M.; Tillekaratne, A.; Simonovis, J. P.; Zaera, F. *Physical Chemistry Chemical Physics* **2016**, *18*, 19248–19258.

- [17] Dong, Y.; Zaera, F. *Catalysis Science & Technology* **2017**,
- [18] Bos, A. N. R.; Westerterp, K. R. *Chemical Engineering and Processing: Process Intensification* **1993**, *32*, 1–7.
- [19] Nakatsuji, H.; Hada, M. In *Quantum Chemistry: The Challenge of Transition Metals and Coordination Chemistry*; Veillard, A., Ed.; Springer Netherlands: Dordrecht, 1986; pp 477–487.
- [20] Chatt, J.; Duncanson, L. A. *Journal of the Chemical Society (Resumed)* **1953**, 2939–2947.
- [21] Bent, B. E. *Chemical Reviews* **1996**, *96*, 1361–1390.
- [22] Ma, Z.; Zaera, F. *Surface Science Reports* **2006**, *61*, 229–281.
- [23] Demuth, J. E. *Surface Science* **1979**, *84*, 315–328.
- [24] Miura, T.; Kobayashi, H.; Domen, K. *The Journal of Physical Chemistry B* **2000**, *104*, 6809–6814.
- [25] Grogan, M. J.; Nakamoto, K. *Journal of the American Chemical Society* **1966**, *88*, 5454–5460.
- [26] Taylor, H. S. *Proceedings of the Royal Society of London. Series A* **1925**, *108*, 105–111.
- [27] Christensen, C. H.; Nørskov, J. K. *The Journal of Chemical Physics* **2008**, *128*, 182503.
- [28] Nørskov, J. K.; Bligaard, T.; Hvolbaek, B.; Abild-Pedersen, F.; Chorkendorff, I.; Christensen, C. H. *Chemical Society Reviews* **2008**, *37*, 2163–2171.
- [29] Bond, G. *Metal-Catalysed Reactions of Hydrocarbons*; Springer US, 2006.
- [30] Cremer, P. S.; Somorjai, G. A. *Journal of the Chemical Society, Faraday Transactions* **1995**, *91*, 3671–3677.
- [31] Cremer, P. S.; Su, X.; Shen, Y. R.; Somorjai, G. A. *Journal of the American Chemical Society* **1996**, *118*, 2942–2949.
- [32] Medlin, J. W.; Allendorf, M. D. *The Journal of Physical Chemistry B* **2003**, *107*, 217–223.
- [33] Borodziński, A.; Bond, G. C. *Catalysis Reviews* **2008**, *50*, 379–469.
- [34] Crampton, A. S.; Rötzer, M. D.; Ridge, C. J.; Schweinberger, F. F.; Heiz, U.; Yoon, B.; Landman, U. *Nature Communications* **2016**, *7*, 10389.
- [35] Xu, C.; Tsai, Y. L.; Koel, B. E. *The Journal of Physical Chemistry* **1994**, *98*, 585–593.
- [36] Xu, C.; Peck, J. W.; Koel, B. *JOURNAL-AMERICAN CHEMICAL SOCIETY* **1993**, *115*, 751–751.

- [37] Peck, J. W.; Koel, B. E. *Journal of the American Chemical Society* **1996**, *118*, 2708–2717.
- [38] Abon, M.; Billy, J.; Bertolini, J. C. *Surface Science Letters* **1986**, *171*, L387–L394.
- [39] Demuth, J. E. *Surface Science* **1979**, *80*, 367–387.
- [40] Malik, I. J.; Agrawal, V. K.; Trenary, M. *The Journal of Chemical Physics* **1988**, *89*, 3861–3869.
- [41] Kesmodel, L. L.; Dubois, L. H.; Somorjai, G. A. *Chemical Physics Letters* **1978**, *56*, 267–271.
- [42] Zaera, F.; Bernstein, N. *Journal of the American Chemical Society* **1994**, *116*, 4881–4887.
- [43] Crampton, A. S. Systematic UHV Study of Ethylene Hydrogenation on Supported, Size-Selected Clusters. Dissertation, 2015.
- [44] Moskaleva, L. V.; Chen, Z.-X.; Aleksandrov, H. A.; Mohammed, A. B.; Sun, Q.; Rösch, N. *The Journal of Physical Chemistry C* **2009**, *113*, 2512–2520.
- [45] Aleksandrov, H. A.; Moskaleva, L. V.; Zhao, Z.-J.; Basaran, D.; Chen, Z.-X.; Mei, D.; Rösch, N. *Journal of Catalysis* **2012**, *285*, 187–195.
- [46] Crampton, A. S.; Rötzer, M. D.; Ridge, C. J.; Yoon, B.; Schweinberger, F. F.; Landman, U.; Heiz, U. *Surface Science* **2016**, *652*, 7–19.
- [47] Lu, X.; Liu, L.; Li, Y.; Guo, W.; Zhao, L.; Shan, H. *Physical Chemistry Chemical Physics* **2012**, *14*, 5642–5650.
- [48] Zaera, F. *ACS Catalysis* **2017**, 4947–4967.
- [49] Zaera, F.; Chrysostomou, D. *Surface Science* **2000**, *457*, 89–108.
- [50] Ilharco, L. M.; Garcia, A. R.; da Silva, J. L. *Surface Science* **1997**, *371*, 289–296.
- [51] Zaera, F. *Physical Chemistry Chemical Physics* **2013**, *15*, 11988–12003.
- [52] Zaera, F. *Catalysis Letters* **2003**, *91*, 1–10.
- [53] Borodziński, A.; Bond, G. C. *Catalysis Reviews* **2006**, *48*, 91–144.
- [54] Al-Ammar, A. S.; Webb, G. *Journal of the Chemical Society, Faraday Transactions 1: Physical Chemistry in Condensed Phases* **1978**, *74*, 195–205.
- [55] Menon, P. G. *Journal of Molecular Catalysis* **1990**, *59*, 207–220.
- [56] Boudart, M. In *Advances in Catalysis*; Eley, D. D., Pines, H., Weisz, P. B., Eds.; Academic Press, 1969; Vol. 20; pp 153–166.

- [57] Zaera, F. *The Journal of Physical Chemistry B* **2002**, *106*, 4043–4052.
- [58] Gluhoi, A. C.; Bakker, J. W.; Nieuwenhuys, B. E. *Catalysis Today* **2010**, *154*, 13–20.
- [59] Haruta, M.; Daté, M. *Applied Catalysis A: General* **2001**, *222*, 427–437.
- [60] Jia, J.; Haraki, K.; Kondo, J. N.; Domen, K.; Tamaru, K. *The Journal of Physical Chemistry B* **2000**, *104*, 11153–11156.
- [61] Segura, Y.; López, N.; Pérez-Ramírez, J. *Journal of Catalysis* **2007**, *247*, 383–386.
- [62] Campbell, C. T. *ACS Catalysis* **2017**, *7*, 2770–2779.
- [63] Stegelmann, C.; Andreasen, A.; Campbell, C. T. *Journal of the American Chemical Society* **2009**, *131*, 8077–8082.
- [64] Jørgensen, M.; Grönbeck, H. *Catalysis Science & Technology* **2017**, *7*, 4034–4040.
- [65] Boudart, M.; Aldag, A.; Benson, J. E.; Dougharty, N. A.; Girvin Harkins, C. *Journal of Catalysis* **1966**, *6*, 92–99.
- [66] Heiz, U.; Sanchez, A.; Abbet, S.; Schneider, W. D. *Journal of the American Chemical Society* **1999**, *121*, 3214–3217.
- [67] Masson, A.; Bellamy, B.; Romdhane, Y. H.; Che, M.; Roulet, H.; Dufour, G. *Surface Science* **1986**, *173*, 479–497.
- [68] Bond, G. C.; Thompson, D. T. *Catalysis Reviews* **1999**, *41*, 319–388.
- [69] de Heer, W. A. *Reviews of Modern Physics* **1993**, *65*, 611–676, RMP.
- [70] Heiz, U.; Sherwood, R.; Cox, D. M.; Kaldor, A.; Yates, J. T. *The Journal of Physical Chemistry* **1995**, *99*, 8730–8735.
- [71] Heiz, U.; Vanolli, F.; Trento, L.; Schneider, W.-D. *Review of Scientific Instruments* **1997**, *68*, 1986–1994.
- [72] Schweinberger, F. F.; Berr, M. J.; Döblinger, M.; Wolff, C.; Sanwald, K. E.; Crampton, A. S.; Ridge, C. J.; Jäckel, F.; Feldmann, J.; Tschurl, M.; Heiz, U. *Journal of the American Chemical Society* **2013**, *135*, 13262–13265.
- [73] Berr, M. J.; Schweinberger, F. F.; Döblinger, M.; Sanwald, K. E.; Wolff, C.; Breimeier, J.; Crampton, A. S.; Ridge, C. J.; Tschurl, M.; Heiz, U.; Jäckel, F.; Feldmann, J. *Nano Letters* **2012**, *12*, 5903–5906.
- [74] von Weber, A.; Anderson, S. L. *Accounts of Chemical Research* **2016**, *49*, 2632–2639.
- [75] von Weber, A.; Baxter, E. T.; White, H. S.; Anderson, S. L. *The Journal of Physical Chemistry C* **2015**, *119*, 11160–11170.

- [76] Riedel, J. N.; Rötzer, M. D.; Jorgensen, M.; Vej-Hansen, U. G.; Pedersen, T.; Sebok, B.; Schweinberger, F. F.; Vesborg, P. C. K.; Hansen, O.; Schiötz, J.; Heiz, U.; Chorkendorff, I. *Catalysis Science & Technology* **2016**, *6*, 6893–6900.
- [77] Harding, C.; Habibpour, V.; Kunz, S.; Farnbacher, A. N.-S.; Heiz, U.; Yoon, B.; Landman, U. *Journal of the American Chemical Society* **2009**, *131*, 538–548.
- [78] Pacchioni, G.; Giordano, L.; Baistrocchi, M. *Physical Review Letters* **2005**, *94*, 226104, PRL.
- [79] Sterrer, M.; Risse, T.; Heyde, M.; Rust, H.-P.; Freund, H.-J. *Physical Review Letters* **2007**, *98*, 206103, PRL.
- [80] Yoon, B.; Häkkinen, H.; Landman, U.; Würz, A. S.; Antonietti, J.-M.; Abbet, S.; Judai, K.; Heiz, U. *Science* **2005**, *307*, 403–407.
- [81] Abbet, S.; Riedo, E.; Brune, H.; Heiz, U.; Ferrari, A. M.; Giordano, L.; Pacchioni, G. *Journal of the American Chemical Society* **2001**, *123*, 6172–6178.
- [82] Crampton, A. S.; Rötzer, M. D.; Schweinberger, F. F.; Yoon, B.; Landman, U.; Heiz, U. *Angewandte Chemie International Edition* **2016**, *55*, 8953–8957.
- [83] Crampton, A. S.; Rötzer, M. D.; Landman, U.; Heiz, U. *ACS Catalysis* **2017**, 6738–6744.
- [84] Röttgen, M. A.; Abbet, S.; Judai, K.; Antonietti, J.-M.; Würz, A. S.; Arenz, M.; Henry, C. R.; Heiz, U. *Journal of the American Chemical Society* **2007**, *129*, 9635–9639.
- [85] Häkkinen, H.; Abbet, S.; Sanchez, A.; Heiz, U.; Landman, U. *Angewandte Chemie International Edition* **2003**, *42*, 1297–1300.
- [86] Wang, B.; Yoon, B.; König, M.; Fukamori, Y.; Esch, F.; Heiz, U.; Landman, U. *Nano Letters* **2012**, *12*, 5907–5912.
- [87] Yoon, B.; Landman, U.; Habibpour, V.; Harding, C.; Kunz, S.; Heiz, U.; Moseler, M.; Walter, M. *The Journal of Physical Chemistry C* **2012**, *116*, 9594–9607.
- [88] Fung, V.; Jiang, D.-e. *The Journal of Physical Chemistry C* **2017**, *121*, 10796–10802.
- [89] Baxter, E. T.; Ha, M.-A.; Cass, A. C.; Alexandrova, A. N.; Anderson, S. L. *ACS Catalysis* **2017**, 3322–3335.
- [90] Heiz, U.; Bullock, E. L. *Journal of Materials Chemistry* **2004**, *14*, 564–577.
- [91] Xu, L.; Spaether, W.; Mingyong, S.; Boyer, J.; Urbancic, M. *Processing Shale Feedstocks* **2013**, 1–4.
- [92] Lindlar, H. *Helvetica Chimica Acta* **1952**, *35*, 446–450.

- [93] García-Mota, M.; Gómez-Díaz, J.; Novell-Leruth, G.; Vargas-Fuentes, C.; Bellarosa, L.; Bridier, B.; Pérez-Ramírez, J.; López, N. *Theoretical Chemistry Accounts* **2011**, *128*, 663–673.
- [94] Kruppe, C. M.; Krooswyk, J. D.; Trenary, M. *ACS Catalysis* **2017**, 8042–8049.
- [95] Armbrüster, M. et al. *ChemCatChem* **2012**, *4*, 1048–1063.
- [96] Zimmermann, R. R.; Hahn, T.; Reschetilowski, W.; Armbrüster, M. *ChemPhysChem* **2017**, *18*, 2517–2525.
- [97] Armbrüster, M.; Kovnir, K.; Behrens, M.; Teschner, D.; Grin, Y.; Schlögl, R. *Journal of the American Chemical Society* **2010**, *132*, 14745–14747.
- [98] Prinz, J.; Pignedoli, C. A.; Stöckl, Q. S.; Armbrüster, M.; Brune, H.; Gröning, O.; Widmer, R.; Passerone, D. *Journal of the American Chemical Society* **2014**, *136*, 11792–11798.
- [99] Osswald, J.; Kovnir, K.; Armbrüster, M.; Giedigkeit, R.; Jentoft, R. E.; Wild, U.; Grin, Y.; Schlögl, R. *Journal of Catalysis* **2008**, *258*, 219–227.
- [100] Yang, B.; Burch, R.; Hardacre, C.; Headdock, G.; Hu, P. *Journal of Catalysis* **2013**, *305*, 264–276.
- [101] Kim, S. K.; Kim, C.; Lee, J. H.; Kim, J.; Lee, H.; Moon, S. H. *Journal of Catalysis* **2013**, *306*, 146–154.
- [102] Yang, B.; Burch, R.; Hardacre, C.; Hu, P.; Hughes, P. *Surface Science* **2016**, *646*, 45–49.
- [103] Hoffmann, F. M. *Surface Science Reports* **1983**, *3*, 107–192.
- [104] Wilson, E. L.; Brown, W. A. *The Journal of Physical Chemistry C* **2010**, *114*, 6879–6893.
- [105] Greenler, R. G. *The Journal of Chemical Physics* **1966**, *44*, 310–315.
- [106] Chesters, M. A.; Gardner, P.; McCash, E. M. *Surface Science* **1989**, *209*, 89–99.
- [107] Garcia, A. R.; Barros, R. B.; Ilharco, L. M. *Journal of Physical Organic Chemistry* **2008**, *21*, 703–712.
- [108] Ilharco, L. M.; Garcia, A. R.; Brito de Barros, R. *Surface Science* **2002**, *516*, 85–94.
- [109] Ilharco, L. M.; Garcia, A. R.; da Silva, J. L. *Surface Science* **1997**, *392*, L27–L32.
- [110] Schweinberger, F. *Catalysis with Supported Size-selected Pt Clusters: Fundamental UHV and Applied Ambient Experiments*; Springer International Publishing, 2016.
- [111] Kunz, S. *Cluster Catalysis Under UHV and Ambient Conditions*; 2010.

- [112] Brundle, C.; Baker, A.; Baker, A. *Electron Spectroscopy: Theory, Techniques and Applications*; Academic Press, 1977.
- [113] Berglund, C. N.; Spicer, W. E. *Physical Review* **1964**, *136*, A1030–A1044, PR.
- [114] Harada, Y.; Masuda, S.; Ozaki, H. *Chemical Reviews* **1997**, *97*, 1897–1952.
- [115] Spirkel, F. M.; Kunz, S.; Schweinberger, F. F.; Farnbacher, A. N.; Schröter, R.; Heiz, U. *Review of Scientific Instruments* **2012**, *83*, 013114.
- [116] Schweinberger, F. F.; Crampton, A. S.; Zimmermann, T.; Kwon, G.; Ridge, C. J.; Günther, S.; Heiz, U. *Surface Science* **2013**, *609*, 18–29.
- [117] Maus-Friedrichs, W.; Wehrhahn, M.; Dieckhoff, S.; Kemper, V. *Surface Science* **1990**, *237*, 257–265.
- [118] Broughton, J. Q.; Perry, D. L. *Surface Science* **1978**, *74*, 307–317.
- [119] King, D. A. *Surface Science* **1975**, *47*, 384–402.
- [120] Redhead, P. A. *Vacuum* **1962**, *12*, 203–211.
- [121] Habenschaden, E.; Küppers, J. *Surface Science* **1984**, *138*, L147–L150.
- [122] Zaera, F. *Surface Science Reports* **2017**, *72*, 59–104.
- [123] Harding, C. J.; Kunz, S.; Habibpour, V.; Teslenko, V.; Arenz, M.; Heiz, U. *Journal of Catalysis* **2008**, *255*, 234–240.
- [124] Kunz, S.; Schweinberger, F. F.; Habibpour, V.; Röttgen, M.; Harding, C.; Arenz, M.; Heiz, U. *The Journal of Physical Chemistry C* **2010**, *114*, 1651–1654.
- [125] Röttgen, M. *Untersuchung von katalytischen Eigenschaften gröÙenselektierter Cluster mittels gepulster Molekularstrahlen*; Universitätsbibliothek der TU München, 2008.
- [126] Crampton, A. S.; Ridge, C. J.; Rötzer, M. D.; Zwaschka, G.; Braun, T.; D’Elia, V.; Basset, J. M.; Schweinberger, F. F.; Günther, S.; Heiz, U. *The Journal of Physical Chemistry C* **2015**, *119*, 13665–13669.
- [127] Wendt, S.; Ozensoy, E.; Wei, T.; Frerichs, M.; Cai, Y.; Chen, M. S.; Goodman, D. W. *Physical Review B* **2005**, *72*, 115409, PRB.
- [128] Schroeder, T.; Giorgi, J. B.; Bäumer, M.; Freund, H. J. *Physical Review B* **2002**, *66*, 165422, PRB.
- [129] Kunz, S.; Schweinberger, F. F.; Kwon, G.; Kiermaier, J.; Le Moal, S.; Henry, C.; Heiz, U. *Surface Science* **2010**, *604*, 2184–2189.

- [130] Pacchioni, G.; Freund, H. *Chemical Reviews* **2013**, *113*, 4035–4072.
- [131] Jung, R.; Lee, J. C.; Orosz, G. T.; Sulyok, A.; Zsolt, G.; Menyhard, M. *Surface Science* **2003**, *543*, 153–161.
- [132] Kunz, S.; Hartl, K.; Nesselberger, M.; Schweinberger, F. F.; Kwon, G.; Hanzlik, M.; Mayrhofer, K. J. J.; Heiz, U.; Arenz, M. *Physical Chemistry Chemical Physics* **2010**, *12*, 10288–10291.
- [133] Wettergren, K.; Schweinberger, F. F.; Deiana, D.; Ridge, C. J.; Crampton, A. S.; Rötzer, M. D.; Hansen, T. W.; Zhdanov, V. P.; Heiz, U.; Langhammer, C. *Nano Letters* **2014**, *14*, 5803–5809.
- [134] Bozack, M. J.; Muehlhoff, L.; Jr., J. N. R.; Choyke, W. J.; Jr., J. T. Y. *Journal of Vacuum Science and Technology A: Vacuum, Surfaces, and Films* **1987**, *5*, 1–8.
- [135] Winkler, A.; Jr., J. T. Y. *Journal of Vacuum Science and Technology A: Vacuum, Surfaces, and Films* **1988**, *6*, 2929–2932.
- [136] Ertl, G.; Neumann, M.; Streit, K. M. *Surface Science* **1977**, *64*, 393–410.
- [137] Murillo, L. E.; Khan, N. A.; Chen, J. G. *Surface Science* **2005**, *594*, 27–42.
- [138] Crampton, A. S.; Rötzer, M. D.; Schweinberger, F. F.; Yoon, B.; Landman, U.; Heiz, U. *Journal of Catalysis* **2016**, *333*, 51–58.
- [139] Amenomiya, Y.; Pottie, R. F. *Canadian Journal of Chemistry* **1968**, *46*, 1735–1739.
- [140] Beebe, T. P.; Yates, J. T. *Surface Science* **1986**, *173*, L606–L612.
- [141] Rioux, R. M.; Hoefelmeyer, J. D.; Grass, M.; Song, H.; Niesz, K.; Yang, P.; Somorjai, G. A. *Langmuir* **2008**, *24*, 198–207.
- [142] Lenz, D. H.; Conner, W. C. *Analytica Chimica Acta* **1985**, *173*, 227–238.
- [143] Dibeler, F. L.; V. H. abd Mohler; deHemptinne, M. *J. Res. Natl. Bur. Stand.* **1954**, *53*, 107–111.
- [144] Zhao, H.; Koel, B. E. *The Journal of Physical Chemistry C* **2009**, *113*, 18152–18162.
- [145] Teplyakov, A. V.; Gurevich, A. B.; Garland, E. R.; Bent, B. E.; Chen, J. G. *Langmuir* **1998**, *14*, 1337–1344.
- [146] Teplyakov, A. V.; Bent, B. E. *The Journal of Physical Chemistry B* **1997**, *101*, 9052–9059.
- [147] Goda, A. M.; Neurock, M.; Barteau, M. A.; Chen, J. G. *Surface Science* **2008**, *602*, 2513–2523.

- [148] Pansoy-Hjelvik, M. E.; Schnabel, P.; Hemminger, J. C. *The Journal of Physical Chemistry B* **2000**, *104*, 6554–6561.
- [149] Manner, W. L.; Girolami, G. S.; Nuzzo, R. G. *The Journal of Physical Chemistry B* **1998**, *102*, 10295–10306.
- [150] Yang, M.; Somorjai, G. A. *Journal of the American Chemical Society* **2004**, *126*, 7698–7708.
- [151] Yang, M.; Chou, K. C.; Somorjai, G. A. *The Journal of Physical Chemistry B* **2004**, *108*, 14766–14779.
- [152] Hugenschmidt, M. B.; Diaz, A. L.; Campbell, C. T. *The Journal of Physical Chemistry* **1992**, *96*, 5974–5978.
- [153] Henn, F. C.; Diaz, A. L.; Bussell, M. E.; Hugenschmidt, M. B.; Domagala, M. E.; Campbell, C. T. *The Journal of Physical Chemistry* **1992**, *96*, 5965–5974.
- [154] Bussell, M. E.; Henn, F. C.; Campbell, C. T. *The Journal of Physical Chemistry* **1992**, *96*, 5978–5982.
- [155] Manner, W. L.; Bishop, A. R.; Girolami, G. S.; Nuzzo, R. G. *The Journal of Physical Chemistry B* **1998**, *102*, 8816–8824.
- [156] Bishop, A. R.; Girolami, G. S.; Nuzzo, R. G. *The Journal of Physical Chemistry B* **2000**, *104*, 754–763.
- [157] Ilharco, L. M.; Garcia, A. R.; Hargreaves, E. C.; Chesters, M. A. *Surface Science* **2000**, *459*, 115–123.
- [158] Garcia, A. R.; Barros, R. B. d.; Ilharco, L. M. *Surface Science* **2001**, *482-485, Part 1*, 107–113.
- [159] Garcia, A. R.; Brito de Barros, R.; Ilharco, L. M. *Surface Science* **2003**, *532-535*, 179–184.
- [160] Garcia, A. R.; Lopes da Silva, J.; Ilharco, L. M. *The Journal of Physical Chemistry B* **1999**, *103*, 6746–6751.
- [161] Carlier, P.; Dubois, J. E.; Masclet, P.; Mouvier, G. *Journal of Electron Spectroscopy and Related Phenomena* **1975**, *7*, 55–67.
- [162] Bieri, G.; Burger, F.; Heilbronner, E.; Maier, J. P. *Helvetica Chimica Acta* **1977**, *60*, 2213–2233.
- [163] Ertl, G. *Surface Science* **1979**, *89*, 525–539.
- [164] Crowell, J. E.; Garfunkel, E. L.; Somorjai, G. A. *Surface Science* **1982**, *121*, 303–320.
- [165] Garcia, A. R.; Brito de Barros, R.; Ilharco, L. M. *Surface Science* **2002**, *502-503*, 169–175.

- [166] Megiris, C. E.; Berlowitz, P.; Butt, J. B.; Kung, H. H. *Surface Science* **1985**, *159*, 184–198.
- [167] Avery, N. R. *Langmuir* **1988**, *4*, 445–448.
- [168] Peck, J. W.; Mahon, D. I.; Koel, B. E. *Surface Science* **1998**, *410*, 200–213.
- [169] Salmeron, M.; Somorjai, G. A. *The Journal of Physical Chemistry* **1982**, *86*, 341–350.
- [170] Bădescu, c. C.; Jacobi, K.; Wang, Y.; Bedürftig, K.; Ertl, G.; Salo, P.; Ala-Nissila, T.; Ying, S. C. *Physical Review B* **2003**, *68*, 205401, PRB.
- [171] Mittendorfer, F.; Thomazeau, C.; Raybaud, P.; Toulhoat, H. *The Journal of Physical Chemistry B* **2003**, *107*, 12287–12295.
- [172] Tait, S. L.; Dohnálek, Z.; Campbell, C. T.; Kay, B. D. *The Journal of Chemical Physics* **2005**, *122*, 164707.
- [173] Tait, S. L.; Dohnálek, Z.; Campbell, C. T.; Kay, B. D. *The Journal of Chemical Physics* **2006**, *125*, 234308.
- [174] Campbell, J. M.; Seimanides, S.; Campbell, C. T. *The Journal of Physical Chemistry* **1989**, *93*, 815–826.
- [175] Vasquez, N.; Madix, R. J. *Journal of Catalysis* **1998**, *178*, 234–252.
- [176] Morales, R.; Zaera, F. *The Journal of Physical Chemistry B* **2006**, *110*, 9650–9659.
- [177] Saeys, M.; Reyniers, M.-F.; Marin, G. B.; Neurock, M. *The Journal of Physical Chemistry B* **2002**, *106*, 7489–7498.
- [178] Scoggins, T. B.; White, J. M. *The Journal of Physical Chemistry B* **1999**, *103*, 9663–9672.
- [179] Simonovis, J.; Tillekaratne, A.; Zaera, F. *The Journal of Physical Chemistry C* **2017**, *121*, 2285–2293.
- [180] Lee, I.; Zaera, F. *Journal of the American Chemical Society* **2005**, *127*, 12174–12175.
- [181] Delbecq, F.; Zaera, F. *Journal of the American Chemical Society* **2008**, *130*, 14924–14925.
- [182] Garcia, A. R.; Brito de Barros, R.; Ilharco, L. M. *Surface Science* **2004**, *566-568, Part 2*, 733–739.
- [183] Tyo, E. C.; Vajda, S. *Nat Nano* **2015**, *10*, 577–588.
- [184] Yoshihide, W. *Science and Technology of Advanced Materials* **2014**, *15*, 063501.
- [185] Abbet, S.; Sanchez, A.; Heiz, U.; Schneider, W.-D. *Journal of Catalysis* **2001**, *198*, 122–127.
- [186] Abbet, S.; Sanchez, A.; Heiz, U.; Schneider, W. D.; Ferrari, A. M.; Pacchioni, G.; Rösch, N. *Surface Science* **2000**, *454*, 984–989.

- [187] Dai, Y.; Gorey, T. J.; Anderson, S. L.; Lee, S.; Lee, S.; Seifert, S.; Winans, R. E. *The Journal of Physical Chemistry C* **2017**, *121*, 361–374.
- [188] Yasumatsu, H.; Fukui, N. *Catalysis Science & Technology* **2016**, *6*, 6910–6915.
- [189] Yin, C. et al. *Journal of Materials Chemistry A* **2017**, *5*, 4923–4931.
- [190] Kane, M. D.; Roberts, F. S.; Anderson, S. L. *The Journal of Physical Chemistry C* **2015**, *119*, 1359–1375.
- [191] Reber, A. C.; Khanna, S. N.; Roberts, F. S.; Anderson, S. L. *The Journal of Physical Chemistry C* **2016**, *120*, 2126–2138.
- [192] Watanabe, Y.; Wu, X.; Hirata, H.; Isomura, N. *Catalysis Science & Technology* **2011**, *1*, 1490–1495.
- [193] Isomura, N.; Wu, X.; Hirata, H.; Watanabe, Y. *Journal of Vacuum Science & Technology A: Vacuum, Surfaces, and Films* **2010**, *28*, 1141–1144.
- [194] Isomura, N.; Wu, X.; Watanabe, Y. *The Journal of Chemical Physics* **2009**, *131*, 164707.
- [195] Kaden, W. E.; Wu, T.; Kunkel, W. A.; Anderson, S. L. *Science* **2009**, *326*, 826–829.
- [196] Bonanni, S.; Ait-Mansour, K.; Harbich, W.; Brune, H. *Journal of the American Chemical Society* **2012**, *134*, 3445–3450.
- [197] Bonanni, S.; Ait-Mansour, K.; Brune, H.; Harbich, W. *ACS Catalysis* **2011**, *1*, 385–389.
- [198] Imaoka, T.; Akanuma, Y.; Haruta, N.; Tsuchiya, S.; Ishihara, K.; Okayasu, T.; Chun, W.-J.; Takahashi, M.; Yamamoto, K. *Nature Communications* **2017**, *8*, 688.
- [199] Ha, M.-A.; Baxter, E. T.; Cass, A.; Anderson, S. L.; Alexandrova, A. N. *Journal of the American Chemical Society* **2017**,
- [200] Rioux, R. M.; Song, H.; Hoefelmeyer, J. D.; Yang, P.; Somorjai, G. A. *The Journal of Physical Chemistry B* **2005**, *109*, 2192–2202.
- [201] Koestner, R. J.; Frost, J. C.; Stair, P. C.; Van Hove, M. A.; Somorjai, G. A. *Surface Science* **1982**, *116*, 85–103.
- [202] Rötzer, M. D.; Krause, M.; Crampton, A. S.; Mitterreiter, E.; Heenen, H. H.; Schweinberger, F. F.; Reuter, K.; Heiz, U. *The Journal of Physical Chemistry C* **2018**, *122*, 4428–4436.
- [203] Zhao, H.; Welch, L. A.; Koel, B. E. *Surface Science* **2009**, *603*, 3355–3360.
- [204] Landman, U.; Yoon, B.; Zhang, C.; Heiz, U.; Arenz, M. *Topics in Catalysis* **2007**, *44*, 145–158.

- [205] Chaves, A. S.; Rondina, G. G.; Piotrowski, M. J.; Tereshchuk, P.; Da Silva, J. L. F. *The Journal of Physical Chemistry A* **2014**, *118*, 10813–10821.
- [206] Vajda, S.; Pellin, M. J.; Greeley, J. P.; Marshall, C. L.; Curtiss, L. A.; Ballentine, G. A.; Elam, J. W.; Catillon-Mucherie, S.; Redfern, P. C.; Mehmood, F.; Zapol, P. *Nat Mater* **2009**, *8*, 213–216, 10.1038/nmat2384.
- [207] Okrut, A.; Runnebaum, R. C.; Ouyang, X.; Lu, J.; Aydin, C.; Hwang, S.-J.; Zhang, S.; Olatunji-Ojo, O. A.; Durkin, K. A.; Dixon, D. A.; Gates, B. C.; Katz, A. *Nat Nano* **2014**, *9*, 459–465.
- [208] Liu, L.; Diaz, U.; Arenal, R.; Agostini, G.; Concepcion, P.; Corma, A. *Nat Mater* **2017**, *16*, 132–138.
- [209] Giordano, L.; Cinquini, F.; Pacchioni, G. *Physical Review B* **2006**, *73*, 045414, PRB.
- [210] Prada, S.; Martinez, U.; Pacchioni, G. *Physical Review B* **2008**, *78*, 235423, PRB.
- [211] Zhao, S.; Li, Y.; Liu, D.; Liu, J.; Liu, Y.-M.; Zakharov, D. N.; Wu, Q.; Orlov, A.; Gewirth, A. A.; Stach, E. A.; Nuzzo, R. G.; Frenkel, A. I. *The Journal of Physical Chemistry C* **2017**, *121*, 18962–18972.
- [212] Ohno, S.; Wilde, M.; Mukai, K.; Yoshinobu, J.; Fukutani, K. *The Journal of Physical Chemistry C* **2016**, *120*, 11481–11489.
- [213] Jung, U.; Elsen, A.; Li, Y.; Smith, J. G.; Small, M. W.; Stach, E. A.; Frenkel, A. I.; Nuzzo, R. G. *ACS Catalysis* **2015**, *5*, 1539–1551.
- [214] Binder, A.; Seipenbusch, M.; Muhler, M.; Kasper, G. *Journal of Catalysis* **2009**, *268*, 150–155.
- [215] Silvestre-Albero, J.; Rupprechter, G.; Freund, H.-J. *Journal of Catalysis* **2005**, *235*, 52–59.
- [216] Silvestre-Albero, J.; Rupprechter, G.; Freund, H.-J. *Journal of Catalysis* **2006**, *240*, 58–65.
- [217] Shaikhutdinov, S.; Heemeier, M.; Bäumer, M.; Lear, T.; Lennon, D.; Oldman, R. J.; Jackson, S. D.; Freund, H. J. *Journal of Catalysis* **2001**, *200*, 330–339.
- [218] Burkholder, L.; Stacchiola, D.; Tysoe, W. T. *Surface Review and Letters* **2003**, *10*, 909–916.
- [219] Tilekaratne, A.; Simonovis, J. P.; López Fagúndez, M. F.; Ebrahimi, M.; Zaera, F. *ACS Catalysis* **2012**, *2*, 2259–2268.
- [220] Zaera, F. *Catalysis Letters* **2003**, *91*, 1–10.
- [221] Zaera, F.; Somorjai, G. A. *Journal of the American Chemical Society* **1984**, *106*, 2288–2293.
- [222] Zeigarnik, A. V.; Valdés-Pérez, R. E.; Egorova, N. I. *Surface Science* **2001**, *487*, 146–158.

- [223] Teschner, D.; Borsodi, J.; Kis, Z.; Szentmiklósi, L.; Révay, Z.; Knop-Gericke, A.; Schlögl, R.; Torres, D.; Sautet, P. *The Journal of Physical Chemistry C* **2010**, *114*, 2293–2299.
- [224] Teschner, D.; Pestryakov, A.; Kleimenov, E.; Hävecker, M.; Bluhm, H.; Sauer, H.; Knop-Gericke, A.; Schlögl, R. *Journal of Catalysis* **2005**, *230*, 195–203.
- [225] Teschner, D.; Wild, U.; Schlögl, R.; Paál, Z. *The Journal of Physical Chemistry B* **2005**, *109*, 20516–20521.
- [226] Ludwig, W.; Savara, A.; Madix, R. J.; Schauermann, S.; Freund, H.-J. *The Journal of Physical Chemistry C* **2012**, *116*, 3539–3544.
- [227] Wilde, M.; Fukutani, K.; Ludwig, W.; Brandt, B.; Fischer, J.-H.; Schauermann, S.; Freund, H.-J. *Angewandte Chemie International Edition* **2008**, *47*, 9289–9293.
- [228] Tew, M. W.; Miller, J. T.; van Bokhoven, J. A. *The Journal of Physical Chemistry C* **2009**, *113*, 15140–15147.
- [229] Tew, M. W.; Janousch, M.; Huthwelker, T.; van Bokhoven, J. A. *Journal of Catalysis* **2011**, *283*, 45–54.
- [230] Sauer, J.; Freund, H.-J. *Catalysis Letters* **2015**, *145*, 109–125.
- [231] Khan, N. A.; Shaikhutdinov, S.; Freund, H. J. *Catalysis Letters* **2006**, *108*, 159–164.
- [232] Doyle, A. M.; Shaikhutdinov, S. K.; Freund, H. J. *Journal of Catalysis* **2004**, *223*, 444–453.
- [233] Aleksandrov, H. A.; Kozlov, S. M.; Schauermann, S.; Vayssilov, G. N.; Neyman, K. M. *Angewandte Chemie International Edition* **2014**, *53*, 13371–13375.
- [234] Latusek, M. P.; Spigarelli, B. P.; Heimerl, R. M.; Holles, J. H. *Journal of Catalysis* **2009**, *263*, 306–314.
- [235] Skoglund, M. D.; Holles, J. H. *Catalysis Letters* **2013**, *143*, 966–974.
- [236] Pallassana, V.; Neurock, M.; Lusvardi, V. S.; Lerou, J. J.; Kragten, D. D.; van Santen, R. A. *The Journal of Physical Chemistry B* **2002**, *106*, 1656–1669.
- [237] Neyman, K.; Schauermann, S. *Angewandte Chemie International Edition* **2010**, *49*, 4743–4746.
- [238] Lundwall, M. J.; McClure, S. M.; Goodman, D. W. *The Journal of Physical Chemistry C* **2010**, *114*, 7904–7912.
- [239] Pallassana, V.; Neurock, M. *Journal of Catalysis* **2000**, *191*, 301–317.
- [240] Hammer, B.; Nørskov, J. K. *Surface Science* **1995**, *343*, 211–220.

- [241] Stacchiola, D.; Azad, S.; Burkholder, L.; Tysoe, W. T. *The Journal of Physical Chemistry B* **2001**, *105*, 11233–11239.
- [242] Heard, C. J.; Hu, C.; Skoglundh, M.; Creaser, D.; Grönbeck, H. *ACS Catalysis* **2016**, *6*, 3277–3286.
- [243] Sutter, P.; Sadowski, J. T.; Sutter, E. A. *Journal of the American Chemical Society* **2010**, *132*, 8175–8179.
- [244] Ferrighi, L.; Perilli, D.; Selli, D.; Di Valentin, C. *ACS Applied Materials & Interfaces* **2017**, *9*, 29932–29941.
- [245] McCue, A. J.; Guerrero-Ruiz, A.; Ramirez-Barria, C.; Rodríguez-Ramos, I.; Anderson, J. A. *Journal of Catalysis* **2017**, *355*, 40–52.
- [246] Huang, X.; Xia, Y.; Cao, Y.; Zheng, X.; Pan, H.; Zhu, J.; Ma, C.; Wang, H.; Li, J.; You, R.; Wei, S.; Huang, W.; Lu, J. *Nano Research* **2017**, *10*, 1302–1312.
- [247] Cao, Y.; Sui, Z.; Zhu, Y.; Zhou, X.; Chen, D. *ACS Catalysis* **2017**, *7*, 7835–7846.
- [248] McCue, A. J.; Anderson, J. A. *Frontiers of Chemical Science and Engineering* **2015**, *9*, 142–153.
- [249] Witte, P. T.; Boland, S.; Kirby, F.; van Maanen, R.; Bleeker, B. F.; de Winter, D. A. M.; Post, J. A.; Geus, J. W.; Berben, P. H. *ChemCatChem* **2013**, *5*, 582–587.
- [250] Mei, D.; Neurock, M.; Smith, C. M. *Journal of Catalysis* **2009**, *268*, 181–195.
- [251] López, N.; Bridier, B.; Pérez-Ramírez, J. *The Journal of Physical Chemistry C* **2008**, *112*, 9346–9350.
- [252] Silvestre-Albero, J.; Rupprechter, G.; Freund, H.-J. *Chemical Communications* **2006**, 80–82.
- [253] Ahn, I. Y.; Lee, J. H.; Kum, S. S.; Moon, S. H. *Catalysis Today* **2007**, *123*, 151–157.
- [254] Teschner, D.; Borsodi, J.; Wootsch, A.; Révay, Z.; Hävecker, M.; Knop-Gericke, A.; Jackson, S. D.; Schlögl, R. *Science* **2008**, *320*, 86–89.
- [255] Teschner, D.; Vass, E.; Hävecker, M.; Zafeiratos, S.; Schnörch, P.; Sauer, H.; Knop-Gericke, A.; Schlögl, R.; Chamam, M.; Wootsch, A.; Canning, A. S.; Gamman, J. J.; Jackson, S. D.; McGregor, J.; Gladden, L. F. *Journal of Catalysis* **2006**, *242*, 26–37.
- [256] Jungwirthová, I.; Kesmodel, L. L. *The Journal of Physical Chemistry B* **2001**, *105*, 674–680.
- [257] Gates, J. A.; Kesmodel, L. L. *Surface Science* **1983**, *124*, 68–86.

- [258] García-Mota, M.; Bridier, B.; Pérez-Ramírez, J.; López, N. *Journal of Catalysis* **2010**, *273*, 92–102.
- [259] Teschner, D.; Pestryakov, A.; Kleimenov, E.; Hävecker, M.; Bluhm, H.; Sauer, H.; Knop-Gericke, A.; Schlögl, R. *Journal of Catalysis* **2005**, *230*, 186–194.
- [260] Clotet, A.; Pacchioni, G. *Surface Science* **1996**, *346*, 91–107.
- [261] Fahmi, A.; van Santen, R. A. *Surface Science* **1997**, *371*, 53–62.
- [262] Bond, G. C.; Wells, P. B. *Journal of Catalysis* **1966**, *6*, 397–410.
- [263] Bond, G. C.; Wells, P. B. *Journal of Catalysis* **1966**, *5*, 65–73.
- [264] Kaltchev, M.; Stacchiola, D.; Molero, H.; Wu, G.; Blumenfeld, A.; Tysøe, W. *Catalysis Letters* **1999**, *60*, 11–14.
- [265] Vignola, E.; Steinmann, S. N.; Al Farra, A.; Vandegheuchte, B. D.; Curulla, D.; Sautet, P. *ACS Catalysis* **2018**, 1662–1671.
- [266] Borodziński, A.; Gołębiowski, A. *Langmuir* **1997**, *13*, 883–887.
- [267] Borodziński, A. *Catalysis Letters* **1999**, *63*, 35–42.
- [268] Borodziński, A. *Catalysis Letters* **2001**, *71*, 169–175.
- [269] Morkel, M.; Rupprechter, G.; Freund, H.-J. *Surface Science* **2005**, *588*, L209–L219.
- [270] Werner, H. J.; Knowles, P. J.; Lindh, R.; Manby, F. R.; Schütz, M.; Celani, P.; Korona, T.; Rauhut, G.; Amos, R. D.; Bernhardsson, A. MolPro. 2006.

ACKNOWLEDGMENTS

After all these years spent at TUM and in particular at the Lehrstuhl für Physikalische Chemie there are numerous people I would like to thank: first, and most important, Prof. Ulrich K. Heiz for allowing me to perform my PhD thesis at his chair. Working as a Studentische Hilfskraft during Bachelor and Master studies, performing the master thesis abroad, and finally this work would not have been possible without his constant support. Thank you, Ueli, for the scientific freedom to pursue own ideas, but also for giving me the feedback and advice in times of need. Looking back I wouldn't change a single decision, and I think, that's the most honest compliment one can give.

I would also like to thank Prof. Richard Fischer for coordinating this project on the part of Clariant. Changing the point of view from fundamental studies under UHV to industrial relevant challenges, his suggestions and remarks were quite instructive for me and shaped the present work.

The productive combination of experiment and theory was decisively influenced by Prof. Uzi Landman and Dr. Bokwon Yoon. I am very grateful for their help.

Next on the list are the elders of the group: Aras Kartouzian, Friedrich Esch, and Martin Tschurl. Aras and Martin were not only available for scientific discussions, but also for some chess games. Our Chess Clusters are ranked number 2104 out of 23299 groups (91.3%) at the time of writing, which is quite remarkable for Patzers like us. Only a single day I would like to have the enthusiasm of Friedrich about science. Thank you, Friedrich, for a wonderful stay at Berkeley. At this point, I also acknowledge the help of Barbara Lechner, who made this trip possible in the first place. I wish you the best.

During the last couple of years I had the pleasure to work with several great people in the nanocat lab: Florian Schweinberger was the one, who got me to work there, when I was still in my bachelor studies at a time, when the wonderful Claron Ridge was still around. Thank you, Flo, for not only having a huge impact on my scientific career and teaching me how to write and present results, but also for hanging around for fun.

The first few years, Andrew Crampton was a steady companion in the lab. To clarify things it should be noted that he was already in the lab at times I didn't even know what a cluster is. Although one might call him mister ethylene, it is more about the moments besides work, which I will never forget. All the best for you and your family, and I sincerely hope, that you will find the way home to munich one day.

At some point, Drew was replaced by my new partner Maximilian Krause, who is even more interested in technical absurdities than myself. An old man once told me, that he believes, that the nanocat lab will keep on producing important results in the future despite all difficulties. Finally I understand his words and think, that this saying can be successfully prolonged.

Former students like Kathi, Elmar, Mikhail and Maxi contributed at different stages of the project and their valuable input is honored.

Besides the nanocat team, also other group members deserve to be mentioned: in particular Basti, Conz, Fabi and Jan, who represent the long-time escort, and numerous older/younger PhD students like Alex. All of them made the time spent at university or at the tabletop soccer simply awesome and I am proud to say that I have been a member of this group.

The research of our group is ensured and facilitated by the mechanical and electronic workshops. Without their support, direct and with hands-on mentality, none of the experiments presented in this work would have been possible. Also the help of Michael Eckinger for planning the new setup and Dani Reicheneder for organizational issues is appreciated.

Long lasting friends helped to relax from the sometimes exhausting research. It was always a pleasure to meet the former colleagues like Andi, Hannes, Hendrik, Peter, Streck, Rina, and Anna. My football team kept me in shape during all those years. Friends like Mihi, Maxi, Dutsch, Nikl, Marta, Caro, Wal and all the others enriched my personal life in the past (sometimes almost 25 years) and will continue to do so in the future.

I could not think of a better family than the one I already have: my sister Kristin, her husband Tobias, my nephew Kajetan and niece Thekla always impressively demonstrate me that there are more important things in life than work. The support and love of my parents, Silvia and Georg, over the last almost 30 years enabled all of what has been achieved, which is also meant literally in this context. Spending a Friday afternoon at the turning table with my father in order to repair the xy-screw of our manipulator is only one anecdote in this regard. Thank you for everything.

Last but not least I thank the person, who had to suffer most from my grumpy mood during writing of this thesis: my girlfriend Jule. Your love, confidence and support are the most important driving forces, who keep me going. There is not a single day in the future, where I want to miss your smile and happiness. The last couple of years with you just spun away and I look forward to what we will build up together.

Peer Reviewed Journal Articles

1. Kristina, Wettergren; Schweinberger, Florian F; Deiana, Davide; Ridge, Claron J; Crampton, Andrew S; **Rötzer, Marian**; Hansen, Thomas Willum; Zhdanov, Vladimir P; Heiz, Ueli; Langhammer, Christoph: High Sintering Resistance of Size-Selected Platinum Cluster Catalysts by Suppressed Ostwald Ripening. *Nano Letters* 14 (10), 2014, 5803
2. Crampton, A. S.; Ridge, C. J.; **Rötzer, M. D.**; Zwaschka, G.; Braun, T.; D'Elia, V.; Basset, J.-M.; Schweinberger, F. F.; Günther, S.; Heiz, U.: Atomic Structure Control of Silica Thin Films on Pt(111). *J. Phys. Chem. C* 119 (24), 2015, 13665-13669
3. Riedel, Jakob Nordheim; **Rötzer, Marian David**; Jørgensen, Mikkel; Vej-Hansen, Ulrik Grønbjerg; Pedersen, Thomas; Sebok, Bela; Schweinberger, Florian Frank; Vesborg, Peter Christian Kjærgaard; Hansen, Ole; Schiøtz, Jakob; Heiz, Ulrich; Chorkendorff, Ib: H₂/D₂ Exchange Reaction on Mono-Disperse Pt Clusters: Enhanced Activity from Minute O₂ Concentrations. *Catal. Sci. Technol.* 6 (18), 2016, 6893-6900
4. Crampton, Andrew S.; **Rötzer, Marian D.**; Schweinberger, Florian F.; Yoon, Bokwon; Landman, Uzi; Heiz, Ueli: Ethylene Hydrogenation on Supported Ni, Pd and Pt Nanoparticles: Catalyst Activity, Deactivation and the d-Band Model. *Journal of Catalysis* 333, 2016, 51-58
5. Crampton, Andrew S.; **Rötzer, Marian D.**; Schweinberger, Florian F.; Yoon, Bokwon; Landman, Uzi; Heiz, Ueli: Controlling Ethylene Hydrogenation Reactivity on Pt₁₃ Clusters by Varying the Stoichiometry of the Amorphous Silica Support. *Angewandte Chemie International Edition* 55 (31), 2016, 8953-8957
6. Crampton, Andrew S.; **Rötzer, Marian D.**; Ridge, Claron J.; Yoon, Bokwon; Schweinberger, Florian F.; Landman, Uzi; Heiz, Ueli: Assessing the Concept of Structure Sensitivity or Insensitivity for Sub-Nanometer Catalyst Materials. *Surface Science* 652, 2016, 7-19
7. Crampton, Andrew S.; **Rötzer, Marian D.**; Ridge, Claron J.; Schweinberger, Florian F.; Heiz, Ueli; Yoon, Bokwon; Landman, Uzi: Structure Sensitivity in the Non-scalable Regime

- Explored via Catalysed Ethylene Hydrogenation on Supported Platinum Nanoclusters. Nature Communications, 2016, 10389
8. Crampton, Andrew S.; **Rötzer, Marian D.**; Schweinberger, Florian F.; Heiz, Ueli: Vom Großen aufs Kleine schließen. Nachrichten aus der Chemie, 64, 2016, 955-959
 9. Rondelli, M.; Zwaschka, G.; Krause, M.; **Rötzer, M. D.**; Hedhili, M. N.; Högerl, M. P.; D'Elia, V.; Schweinberger, F. F.; Basset, J.-M.; Heiz, U.: Exploring the Potential of Different-Sized Supported Subnanometer Pt Clusters as Catalysts for Wet Chemical Applications. ACS Catalysis, 2017, 7, 4152-4162.
 10. Crampton, Andrew S.; **Rötzer, Marian D.**; Landman, Uzi; Heiz, Ueli: Can Support Acidity Predict Sub-Nanometer Catalyst Activity Trends?. ACS Catalysis, 2017, 6738-6744.
 11. Zwaschka, G.; Rondelli, M.; Krause, M.; **Rötzer, M. D.**; Hedhili, M. N.; Heiz, U.; Basset, J.-M.; Schweinberger, F. F.; D'Elia, V.: Supported Sub-Nanometer Ta Oxide Clusters as Model Catalysts for the Selective Epoxidation of Cyclooctene. New Journal of Chemistry, 42 (4), 2018, 3035-3041

Peer Reviewed Journal Articles Of This Thesis

12. **Rötzer, M. D.**; Krause, M.; Crampton, A. S.; Mitterreiter, E.; Heenen, H. H.; Schweinberger, F. F.; Reuter, K.; Heiz, U.: Surface Chemistry of 1- and 3-Hexyne on Pt(111): Desorption, Decomposition and Dehydrocyclization. J. Phys. Chem. C, 122, 2018, 4428-4436
13. **Rötzer, M. D.**; Crampton, A. S.; Krause, M.; Thanner, K.; Schweinberger, F. F.; Heiz, U.: Hydrogenation of 3-Hexyne on Size-selected, Supported Pt Clusters: Prediction of Enhanced Selectivity, 2018, *in preparation*
14. **Rötzer, M. D.**; Crampton, A. S.; Krause, M.; Heiz, U.; Bokwon, Y.; Landman, U.: Nanotuning via Local Workfunction of Support: Ethylene Hydrogenation on Supported Pt Nanoclusters, 2018, *in preparation*
15. **Rötzer, M. D.**; Krause, M.; Schweinberger, F. F.; Crampton, A. S.; Heiz, U.: Ethylene Hydrogenation on Supported Pd Nanoparticles: Influence of Support on Catalyst Activity and Deactivation, 2018, *in preparation*
16. **Rötzer, M. D.**; Krause, M.; Huber, M.; Schweinberger, F. F.; Crampton, A. S.; Heiz, U.: Selective Hydrogenation of Acetylene on Supported Pd Nanoparticles: Influence of Support and Pretreatment on Catalytic Performance and Active Sites, 2018, *in preparation*

Colophon

This work was created using Texmaker (5.0.2), EndNote (7.7.1), Adobe Illustrator CS5, and IgorPro (6.37). The thesis is based on the template "University of Bristol Thesis" by Víctor F. Breña-Medina (License: Creative Commons CC BY 4.0).

Der Panther

Sein Blick ist vom Vorübergehn der Stäbe
so müd geworden, dass er nichts mehr hält.
Ihm ist, als ob es tausend Stäbe gäbe
und hinter tausend Stäben keine Welt.

Der weiche Gang geschmeidig starker Schritte,
der sich im allerkleinsten Kreise dreht,
ist wie ein Tanz von Kraft um eine Mitte,
in der betäubt ein großer Wille steht.

Nur manchmal schiebt der Vorhang der Pupille
sich lautlos auf -. Dann geht ein Bild hinein,
geht durch der Glieder angespannte Stille -
und hört im Herzen auf zu sein.

Rainer Maria Rilke

